Lukas Legenstein, BSc

Crystal Structure Solution of a Cu-INA Metal-Organic Framework

MASTER'S THESIS

to achieve the university degree of

Diplom-Ingenieur

Master's degree programme:

Technical Physics

submitted to

Graz University of Technology

Supervisor

Ao.Univ.-Prof. Dipl.-Ing. Dr.techn. Roland Resel

Institute of Solid State Physics

Graz, October 2020

AFFIDAVIT

I declare that I have authored this thesis independently, that I have not used other than the declared sources/resources, and that I have explicitly indicated all material which has been quoted either literally or by content from the sources used. The text document uploaded to TUGRAZonline is identical to the present master's thesis.

Date, Signature

Acknowledgment

First and foremost I want to thank my supervisor and mentor Roland Resel, not only for giving me the opportunity to join his work group for this project, but also for always having an open ear for questions big and small. Roland's inclusive manner of managing the work group translated to close collaboration between the colleagues, helping me immensely to progress my work.

I also want to thank all my colleagues from the Resel group for being open to the discussion of ideas and for the pleasant work environment. Especially Benedikt Schrode and Sebastian Hofer deserve praise, since they not only introduced me to the group's methods and shared their deep knowledge, but also diverted much of their time to help me.

Additionally I also want to acknowledge Sabina Rodriguez and Timothée Stassin who synthesized the fINA sample series and provided important preliminary information and data for my work.

Luisa Barba, the scientist responsible for the XRD1 beamline at the *Elettra* synchrotron facility, also needs to be highlighted for offering her great assistance during our measurements and fixing problems even at late hours and weekend days.

Most of all, I want to express eternal gratitude to my parents and family. You supported me throughout the years and made me able to focus on my studies. Be assured that this privilege has not been taken for granted.

Kurzfassung

Das Interesse an metallorganischen Gerüstverbindungen (Engl.: MOFs) hat in den letzten Jahren stark zugenommen und für diese porösen Materialien wurden mehrere Anwendungen wie heterogene Katalyse, Gastransport und Ionentrennung vorgeschlagen. Während mit neuen Kombinationen von Metallionen und organischen Verbindungsmolekülen und den Methoden diese als dünne Schichten zu präparieren experimentiert wird, sind die Methoden zu deren Strukturuntersuchung noch unausgereift und ausbaufähig. Röntgenbeugungstechniken liefern wichtige Information über die kristallographische Einheitszelle und Struktur von neuartigen Materialien, die oft für weitere Untersuchungen der Materialeigenschaften benötigt werden. Die Röntgendiffraktometrie unter streifendem Einfallswinkel (Engl.: GIXD) hat sich als oberflächenempfindliche Technik für die Charakterisierung von MOF-Dünnfilmen als unschätzbar wertvoll erwiesen.

Neuartige Dünnschichtproben, die aus Kupfer(II)-Oxid (CuO) oder Kupferhydroxid (Cu(OH)$_2$)-"Nanobelts" und isonikotinischer Säure (INA) synthetisiert wurden, wurden durch komplementäre Röntgendiffraktometriemethoden (Engl.: XRD) untersucht und es wurden zwei unterschiedliche, unbekannte Phasen entdeckt. Durch die Kombination von spekularen XRD und GIXD Methoden konnten die Beugungsmuster indiziert und kristallographische Einheitszellparameter bestimmt werden. Die epitaktische Ausrichtung des Cu-INA Gerüsts, das auf einachsig-ausgerichteten Cu(OH)$_2$-"Nanobelts" gewachsen ist, wurde durch rotierende GIXD-Experimente und daraus berechneten Polfiguren nachgewiesen. Darüber hinaus wurde ein neuartiger Ansatz zur Anwendung der Schweratom-Methode, basierend auf der Patterson-Funktion, zur Lösung der Struktur aus GIXD-Daten getestet. Mittels dieser neuen Anwendung der, heutzutage nicht mehr verwendeten, Schweratom-Methode konnten für das vorliegende Cu-INA Gerüst Positionen der Cu-Atome und einen Teil der organischen Verbindungsmoleküle bestimmt werden.

Abstract

Interest in metal-organic frameworks (MOFs) has surged over the last few years and several applications, such as heterogeneous catalysis, gas transport and ion separation, have been proposed for these porous materials. While new combinations of metallic ions and organic linker molecules and the methods to process those as thin films are experimented with, precise structural investigations for MOF thin films lag behind. Characterization of novel materials with X-ray diffraction techniques produces integral information of the crystallographic unit cell and structure, often needed for further investigations of material properties. Grazing-Incidence X-ray Diffraction (GIXD) has been invaluable, as a surface sensitive technique, for the characterization of MOF thin films. Novel thin film samples synthesized from copper(II) oxide (CuO) or copper hydroxide ($Cu(OH)_2$) nanobelts and isonicotinic acid (INA) were investigated by complementing X-ray diffraction (XRD) techniques and two distinguished, unknown phases were discovered. By combining specular XRD and GIXD, the diffraction patterns could be indexed and crystallographic unit cell parameters determined. Epitaxial alignment of the Cu-INA framework grown on uniaxially aligned $Cu(OH)_2$ nanobelts has been revealed by rotating GIXD experiments and calculated pole figures based thereof. Furthermore, an unprecedented approach of deploying the Heavy-Atom Method, based on the Patterson function, for solving the structure from GIXD data has been tested. For the Cu-INA framework at hand, positions for the Cu atoms and part of the organic linker INA could be determined, using this novel application of the nowadays less used Heavy-Atom Method.

3

Contents

Chapter 1

Metal-organic frameworks

1.1 Overview

Metal-organic frameworks (MOFs) are compound materials consisting of metal ions and organic linker molecules. The organic linkers, also called ligand, are connecting metallic centers to build a framework. Linkers are rigid and their bonds to metallic centers are very directional, therefore void space is part of the framework. Embedded pores play a large part in the surge of research and interest in MOFs since the first publications about these materials and their synthesis in 1998 by O'Keeffe and Yaghi [1], Kondo [2] and others. Metal-organic frameworks are crystalline materials and as a consequence pores are regularly arranged and of homogeneous size.

Open pores and the resulting large internal surface area give rise to several technical applications for MOFs. The applications range from gas sensing [3], transporting [4] and storing [5], to extracting lithium as molecular sieves [6] in the desalination process or as a host material for lithium-based batteries [7], as well as heterogeneous catalysts [8].

Metal centers can be single metal ions or whole coordination clusters. The later mentioned copper isonicotinic acid frameworks provide several examples for single metal ion frameworks and MOF-5 [1] an example for a framework with a cluster of ions.

1.2 MOF-5

An example for a coordination cluster in MOFs would be Zn_4O, representing the metal center for the most prominent and well researched frameworks. In MOF-5

[1], also called IRMOF-1, four Zn^{2+} ions form a tetra nuclear cluster around an O^{2-} ion. Dicarboxylic acid groups of 1,4-benzenedicarboxylate (BDC) bonding to Zn form super tetrahedral nodes connected by rigid benzene rings in three dimensions as seen in Fig. 1.1.
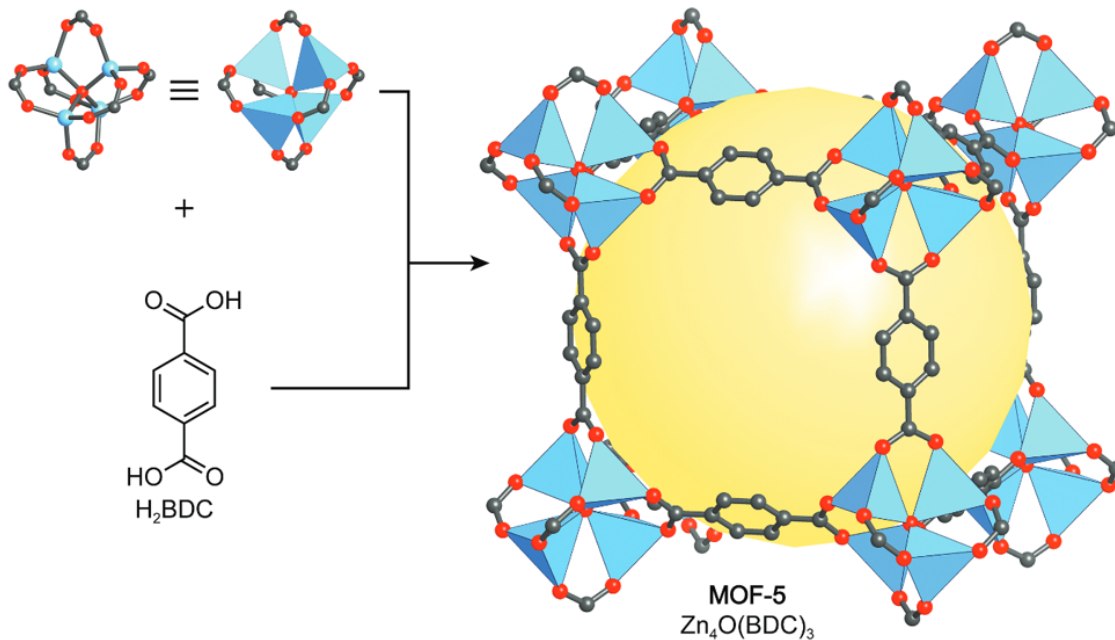
Figure 1.1: O^{2-} (red) in tetra nuclear cluster with Zn^{2+} (blue) bond to six dicarboxylic acid groups (carbon being black) and linked by BDC to form the structure of MOF-5. The pore (yellow sphere) results from the topology. Printed from [9].

Polyhedral depictions like in Fig. 1.1 for the Zn tetrahedral cluster are used to explain the metallic node as a building unit with the polygon corners symbolizing bonding sites of a metal-organic coordination complex. Furthermore, transition metal coordination complexes usually are not following the octet rule since they can utilize d, s and p valence orbitals with up to 18 electrons for bonding. The polyhedral depiction therefore also distinguishes between conventional covalent bonding and coordinate covalent bonding in the presentation of crystalline structures, e.g. in software like *Mercury*.

The name IRMOF-1 derives from isoreticular synthesis, with isoreticular meaning "forming the same net", referring to structures having the same topology [10], even when they consist of chemically different ligands or metallic centers. This description fits the IRMOF series, shown in Fig. 1.2, which features the same topology as IRMOF-1, albeit varying in size and attached functional groups.

7
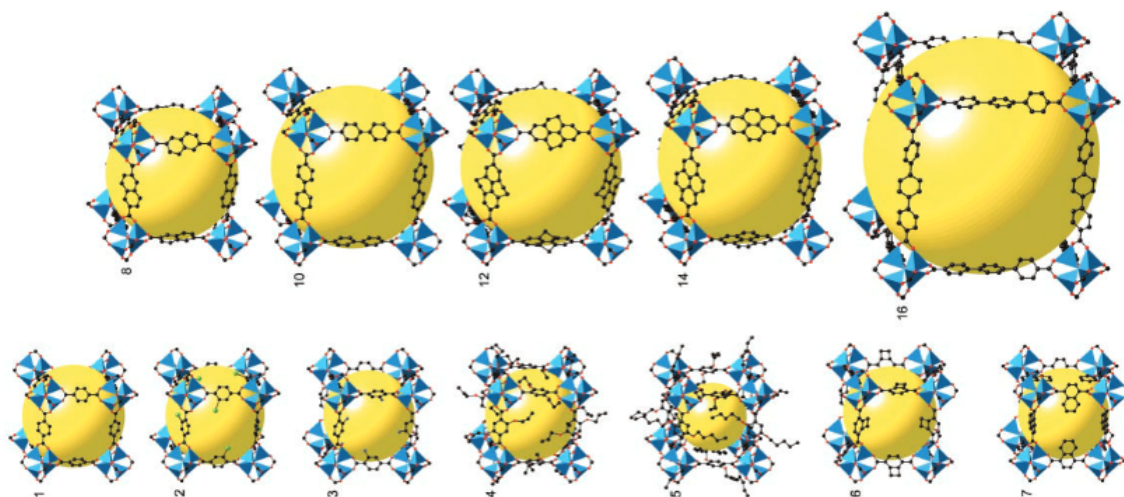
Figure 1.2: Structures of IRMOF-1 to IRMOF-16. The structures of IRMOF-2 to 7 had different functional groups introduced to their linkers, while with IRMOF-8 to 16 increasingly longer molecules connect the metallic clusters. Printed from [10]

Employing linkers similar to BCD, like biphenyl-4,4'-dicarboxylic acid with two benzene rings or terphenyl-4,4'-dicarboxylic acid with three rings, creates frameworks with the same topology, but varying pore sizes. Pore diameters vary between 3.8 Å to 28.8 Å [10], as seen in schematic 8 to 16 in Fig. 1.2. Using the largest sphere that can fit between the frameworks atoms, without touching their *van der Waals* surface, is a simple way to quantify and display the pore diameter. At the same time different functional groups, e.g. an amino group NH_2, can be introduced to a linker without changing the topology of the net, but decreasing the pore size.

Varying the pore diameter via the length of linker molecules and tuning the chemical functionality did not change the periodicity and stability of these crystalline frameworks, which sparked a large interest in metal-organic frameworks as tune-able, porous materials with large internal surface areas.

1.3 Copper isonicotinic acid frameworks

In this section different frameworks with copper ion centers and isonicotinic acid (INA) [11] as a linker are introduced, since the research of this thesis was dedicated to a series of Cu-INA framework thin film samples.

A more precise name for isonicotinic acid would be 4-pyridinecarboxylic acid and its chemical formula can be seen in Figure 3. Similar to the commonly occurring linker BDC, INA is also composed of an aromatic ring with a carboxylic acid group. It differs from BDC as it has a nitrogen atom replacing a carbon atom in the ring opposite to the carboxylic acid group, making it not only shorter than BDC but also changing the ability to bond on that end of the molecule. Cu-INA frameworks are formed by the carboxylic as well as the pyridyl groups both bonding to Cu ions and therefore linking them. Several structures of Cu-INA frameworks are already registered in the *Cambridge Crystallographic Data Center* (CCDC), showing a variety of different metallic nodes and topologies.

One of the simplest examples is a Cu-INA framework with CCDC codename *UFUMUD* [12]. Interestingly, there are reported structures of the same single crystal for several research steps, starting from synthesis, to cleansing of water from the pores and also transport experiments with several smaller gas molecules. Metal centers of the structure are Cu(II) ions, manifesting in a square pyramidal coordination complex when stabilized and linked by INA to form a 3D framework. The electronic configuration of Cu(II) (Cu^{2+}) would be [Ar] $3d^9$ $4s^0$, suggesting preferred bonding with three ligands to fill both 3d- and 4s-orbitals. The square pyramidal Cu node provides five ligand bonding sites [13], made possible by the electron sharing of nitrogen. Since the lone atom pairs of N are facing away from the pyridine ring, they provide two electrons for coordinate covalent bonding with Cu, a common type of bond between transition metals and ligands.

In Fig. 1.3 the atomic makeup of the coordination complex and polyhedral geometry are displayed. The square base of the Cu complex, with almost in-plane, orthogonal ligand sites, leads to the spiral topology of diagonal repetition (also in Fig. 1.3), resulting in an $8.9\,\text{Å}$ x $8.9\,\text{Å}$ area between the Cu nodes in the framework. The largest spheres able to fit into the structure's voids considering the *van der Waals* radii [14], is around $1.95\,\text{Å}$ in diameter and was displayed inside the crystallographic unit cell of *UFUMUD* in Fig. 1.3. Since the framework is spirally extending in the crystallographic a direction, as described in [12], the pores extend in the same direction, forming separated open channels through the material. For
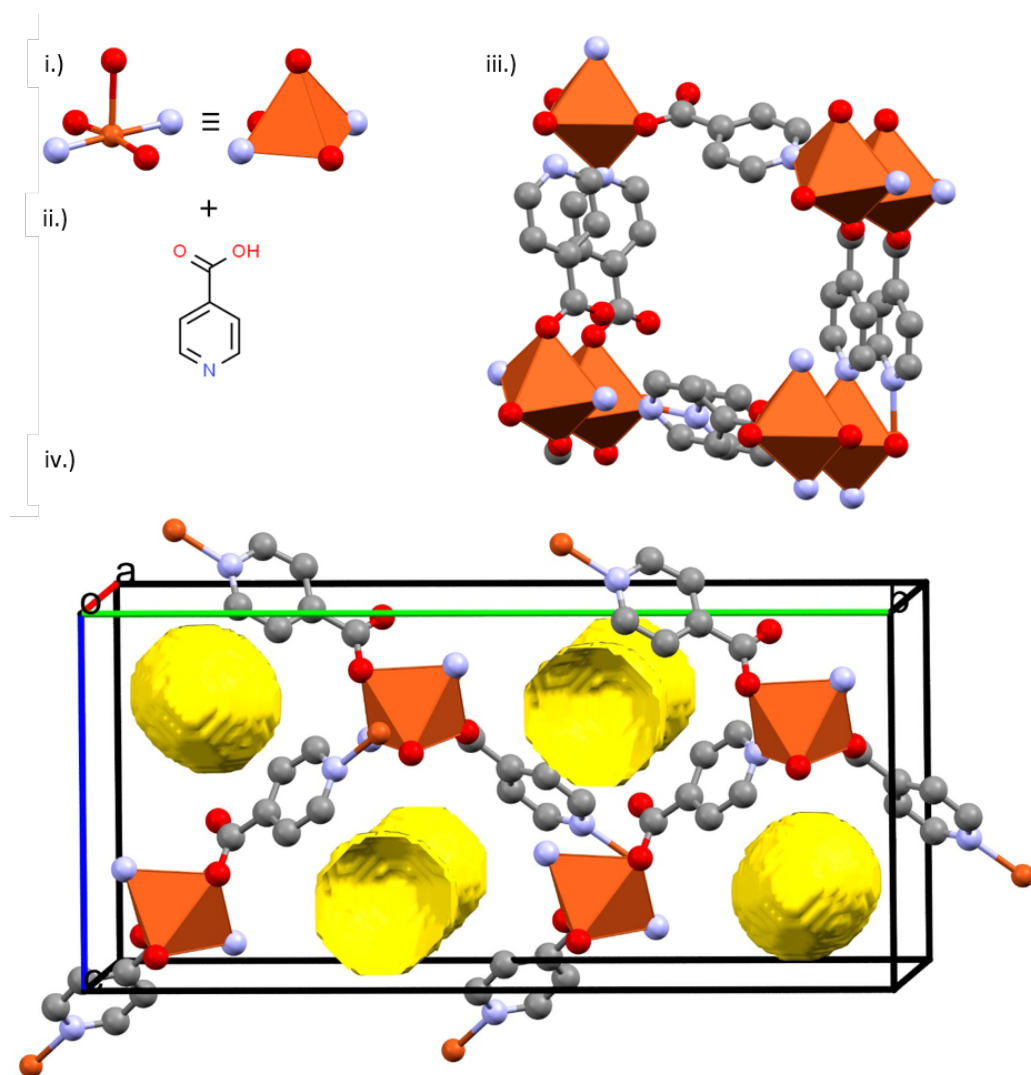
Figure 1.3: : i.) Cu (brown) coordinated with O (red) and N (blue) from carboxyl and pyridyl of INA (ii.) chemical structure) in a square pyramidal complex.

iii.) Spiral 3D framework formed by square pyramidal Cu node linked by INA.

iv.)Crystallographic unit cell of *UFUMUD* with 1.95 Å diameter pore (yellow) indicating the open channel traversing through the framework along the crystallographic *a* direction.

H_2 molecules with *van der Waals* radii of approximately 1.2 Å, around 23% of the unit cell volume is accessible.

Another commonly occurring metal ion cluster in Cu-INA frameworks is the copper bi-paddle-wheel, where two Cu ions at around 2.65 Å distance are stabilized by four carboxylic groups bonding to the four sites at the base of the square pyramidal Cu ion complexes. An example for a Cu-INA structure with this metallic node would be *CIBFUR* [15], where the Cu paddle-wheel can be found at the center and on half-lenghts of the edges of the unit cell. There is a second kind of ion cluster in

the framework, where Cu is surrounded by three pyridine groups and linked to the paddle-wheel. This distorted square pyramidal coordination complex is similar to the one in Fig. 1.3, with the exception of a N atom instead of an O atom on the apical site and a slightly different bonding geometry. In Fig. 1.4 both complexes, their connection and the crystallographic unit cell are displayed. The topology of *CIBFUR* in combination with the length of INA does not create voids of relevant size, meaning the pores are generally smaller than $1.2\,\text{Å}$ and can't host H_2.
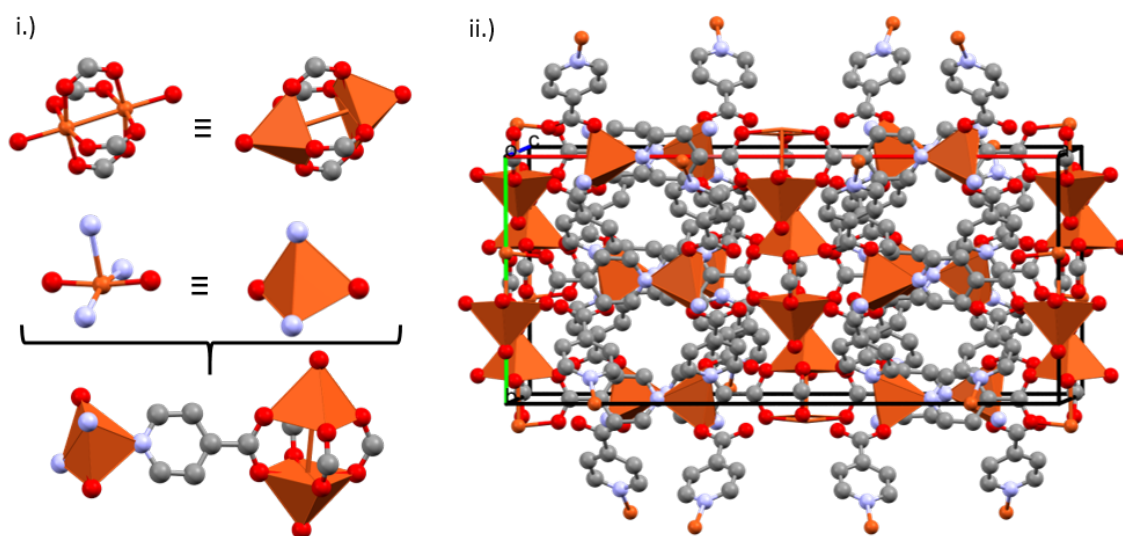
Figure 1.4: i.) Cu paddlewheel connected to opposing square pyramidal complexes. Three pyridine and two carboxyl groups form a distorted square pyramidal cluster.
ii.) Crystallographic unit cell of 3D framework structure of *CIBFUR* [15] with a Cu-paddlewheel at the center.

Octohedral nodes are also a possibility for copper INA frameworks. In the structure *AHEMEG* [16], three Cu ions create a conglomeration of different adjacent coordination complexes. The octohedral complex consists of two opposing N and O atoms in one plane and O atoms at the top and bottom site. Adjacent complexes are tetrahedrons and asymmetrical polygons with five sites and are depicted in Fig. 1.5. INA linkers interconnecting those metallic complexes reduce the size of pores within *AHEMEG* to around 1.05 Å, according to *Mercury*.
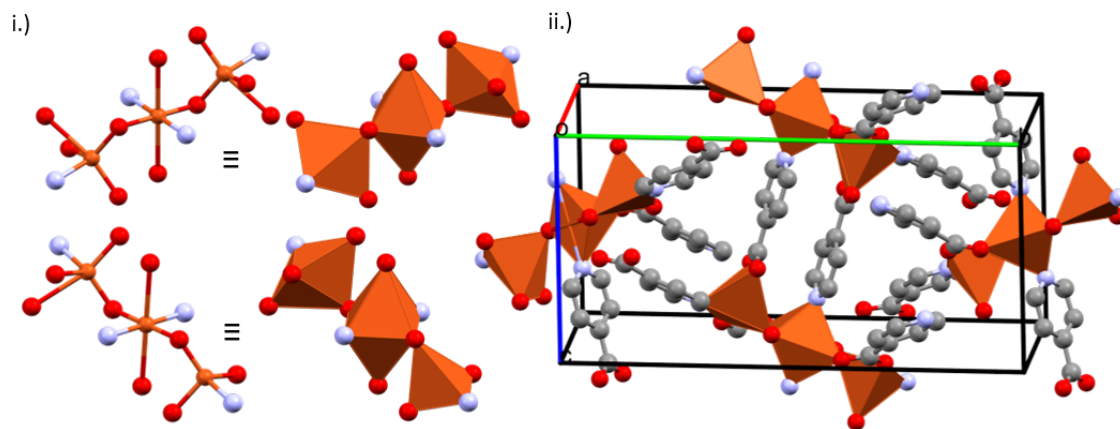
Figure 1.5: i.) Conglomeration of Cu coordination complexes in *AHEMEG*. The octahedral complex is adjacent by a tetrahedral complex and a polygon of irregular shape. ii.) Crystallographic unit cell of 3D framework *AHEMEG* [16].

Several distinct topologies and coordination complexes arise, just from Cu ion nodes with INA linkers. Differences in topology can be attributed to the synthesis processes and their process parameters, but result in structurally different materials. The distinction of these complexes and their ramification on the structure, will be important during the later described investigation of the crystal structure of the fINA samples.

Chapter 2

Experimental Techniques

In this chapter, the basis and the theoretical aspects of the applied experimental techniques are explained.

2.1 Crystal textures of thin film samples

The investigated crystalline thin film samples can be divided in different classifications regarding the orientation of crystallites on their substrate. Different methods have to be applied for their characterization. Classifications of orientation modes according to Heffelfinger and Burton [17] are:

Random: Crystallites are oriented randomly on the substrate surface, with neither preferred alignment to the substrate nor among themselves.

Uniplanar: Crystallites have a preferred orientation where a crystal plane is parallel to the substrate surface. The planes surface normal vector extends out of the substrate, therefore another expression for this crystallite orientation would be out-of-plane orientation. Otherwise the crystallites have no preferred orientation and are aligned randomly.

Axial: One crystal axis is preferred oriented along an axis of the substrate surface. Beyond that, crystal axes perpendicular to the aligned axis are randomly oriented.

Uniplanar-axial: Crytallites have an out-of-plane alignment, as well as a crystal axis with preferred orientation to the substrate. For this combination of preferred orientation, planes not parallel to the substrate surface are aligned among crystallites as well. The alignment of planes of crystallites is called in-plane alignment.

The fINA sample series was experimentally investigated with two different methods, X-ray diffraction (XRD) in the form of a $\theta/2\theta$ scan and Grazing Incidence X-ray

Diffraction (GIXD). The following sections will provide a sufficient description of the methods, in regard of the type of crystalline samples investigated.

2.2 X-Ray Diffraction: A brief overview

The wavelength of X-rays has the same order of magnitude as atomic distances in molecules or lattice constants of crystals. X-rays are scattered elastically by atoms or rather by their electron clouds. Atoms in crystals are regularly arranged and the crystals internal structure can be described by a periodic arrangement of crystallographic unit cells. X-rays are usually not scattered in the same direction, after they are diffracted by the sample. The regular atomic arrangement leads to constructive interference patterns of scattered X-rays, occurring at specific incident angles with respect to the orientation, texture and crystal lattice of the sample. Scattered X-rays can be detected as maxima with measurable intensity, at their characteristic diffraction angles, if conditions for constructive interference are fulfilled. The conditions to be fulfilled are Bragg's law [18] and Laue's equation [19]. Positions in the diffractogram are specified by the scattering vector q, the difference between the primary, incident wave vector k and the secondary, scattered wave vector k',

$$\vec{q} = \Delta\vec{k} = \vec{k'} - \vec{k}, \tag{2.1}$$

and the Laue condition for a reciprocal lattice vector g_{hkl} is formulated as

$$\vec{q} = \vec{g}_{hkl}. \tag{2.2}$$

$$\vec{g}_{hkl} = h\,\vec{a^*} + k\,\vec{b^*} + l\,\vec{c^*}, \tag{2.3}$$

showing, that diffraction peak positions are related to the reciprocal lattice vectors a^*, b^*, c^* of the crystallographic unit cell and Laue indices hkl, integer numbers that specify directions in a reciprocal crystal lattice. Those reciprocal lattice vectors in turn form a geometric relation to the direct lattice vectors a, b, c as,

$$\vec{a^*} = 2\pi \frac{\vec{b} \times \vec{c}}{\vec{a}(\vec{b} \times \vec{c})}, \ \vec{b^*} = 2\pi \frac{\vec{c} \times \vec{a}}{\vec{b}(\vec{c} \times \vec{a})}, \ \vec{c^*} = 2\pi \frac{\vec{a} \times \vec{b}}{\vec{c}(\vec{a} \times \vec{b})}. \tag{2.4}$$

The specific pattern of maxima in a diffractogram can be used to identify the sample from a database or to determine its unit cell parameters. Intensities of maxima reveal information of the underlying symmetries and involved scattering

14

atoms in the unit cell. The intensity $I(hkl)$ can be expressed as the absolute square of the structure factor $F(hkl)$, which depends on atomic number and arrangement of the atoms in the unit cell. More details follow in the chapter about the Patterson function.

There are different requirements for XRD experimental setups, depending on the type of sample and the areas of reciprocal space that need to be investigated for meaningful characterization. A general distinction would be made between e.g. a crystalline powder and a single-crystal samples, both requiring different set-ups. For diffraction on single-crystals or thin films with bi-axial texture, large areas of reciprocal space need to be scanned, since intensity maxima are found at specific reciprocal coordinates (q_x, q_y, q_z), corresponding to a very specific combination of crystal orientation and detector angle. Diffraction reflexes are at discrete spots.

For a polycrystalline sample, every crystalline orientation is present simultaneously. Diffraction reflexes are distributed randomly on spherical shells in 3D reciprocal space with constant radius $q = |\vec{q}|$, related to the detector angle 2θ via Eq. 2.5. The distribution of diffraction reflexes for the previously mentioned crystal textures can be seen in Fig. 2.1. For the uniplanar texture, with out-of-plane aligned and in-plane randomly oriented crystallites, diffraction reflexes are found on rings on a q_{xy}-plane, at specific q_z values. On the other hand, samples with additional in-plane alignment and also single-crystals produce discrete diffraction spots as in Fig. 2.1 b.).

(a) Uniplanar
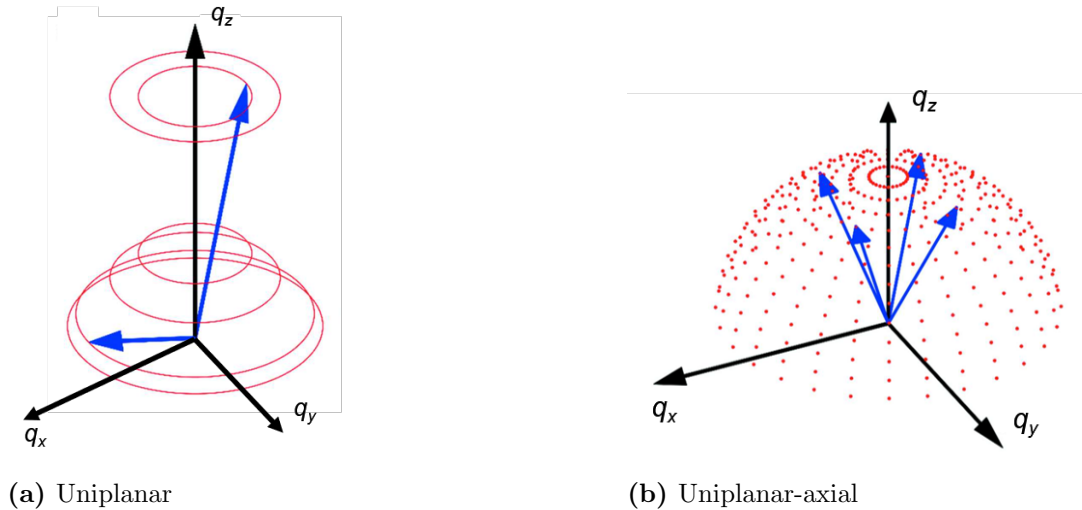
(b) Uniplanar-axial

Figure 2.1: Diffraction reflexes at coordinates in reciprocal space for a.) uniplanar and b.) single-crystal or uniplanar-axial crystal texture. Printed from [20].

2.3 Specular X-ray Diffraction:

The X-ray Diffraction experiments performed to investigate the fINA sample series were so called *specular* scans. For the scan, the angle of the X-ray source θ, is increased within a certain range. The detector's angle mirrors the primary angle, measuring only X-rays scattered at the same angle θ, relative to the surface. Keeping *specular conditions* for source and detector, results in a diffraction pattern, where intensities are detected at reciprocal vectors $\boldsymbol{q}$, normal to the sample surface, as sketched in Fig. 2.2. As in Eq. 2.1, the reciprocal vector is the difference of the
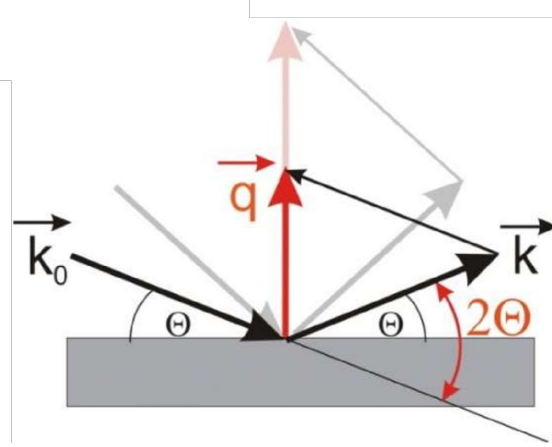
Figure 2.2: Schematic presentation of a specular scan. Printed from [21]

incident and of the scattered wave vector. Besides the z-component, the vector components of the scattering vector $\boldsymbol{q}$ are zero for the specular condition. Diffraction reflexes are solely detected along the q_z-axis. The specular scan or $\theta/2\theta$ scan, is well suited to investigate crystal planes parallel to the substrate. The relation between the detector angle 2θ and length of $\boldsymbol{q}$ is:

$$|\vec{q}| = q = \frac{4\pi}{\lambda} sin(\frac{2\theta}{2}),$$

(2.5)

where λ is the wavelength of X-rays specified by its source.

2.4 Grazing Incidence X-ray Diffraction

GIXD is named after the very small angle ω of the incident beam, chosen around the critical angle of total reflection α_i for X-rays in the material, which is most often roughly in the 0.1° to 0.5° range. An evanescent wave traverses through the material with an exponential decaying penetration depth, providing the basis for

a surface sensitive diffraction experiment [22]. The low penetration depth allows the investigation of thin films, while minimizing diffraction from substrates. During the recording of the diffractogram, the incident angle ω is kept constant. The region of reciprocal space covered, depends on the deployed detector. As discussed in the next chapter, the experiments were performed at a synchrotron facility. Synchrotron radiation is coherent and at a constant, high intensity and the detectors used are mostly 2D-detectors. In scientific literature, this method is commonly referred to as *grazing incidence wide angle X-ray scattering* (GIWAXS), but will be called GIXD for the sake of continuity. This set-up allows the recording of diffractograms, covering larger areas of reciprocal space, in a comparatively short amount of time. Diffractograms recorded by 2D-detectors are 2D projections of 3D reciprocal space vectors and the recorded intensities are mapped to reciprocal positions with coordinates $(q_{xy} = \sqrt{q_x^2 + q_y^2}, q_z)$. Such a set-up can be seen schematically in Fig. 2.3, where scattering onto a 2D-detector is demonstrated.
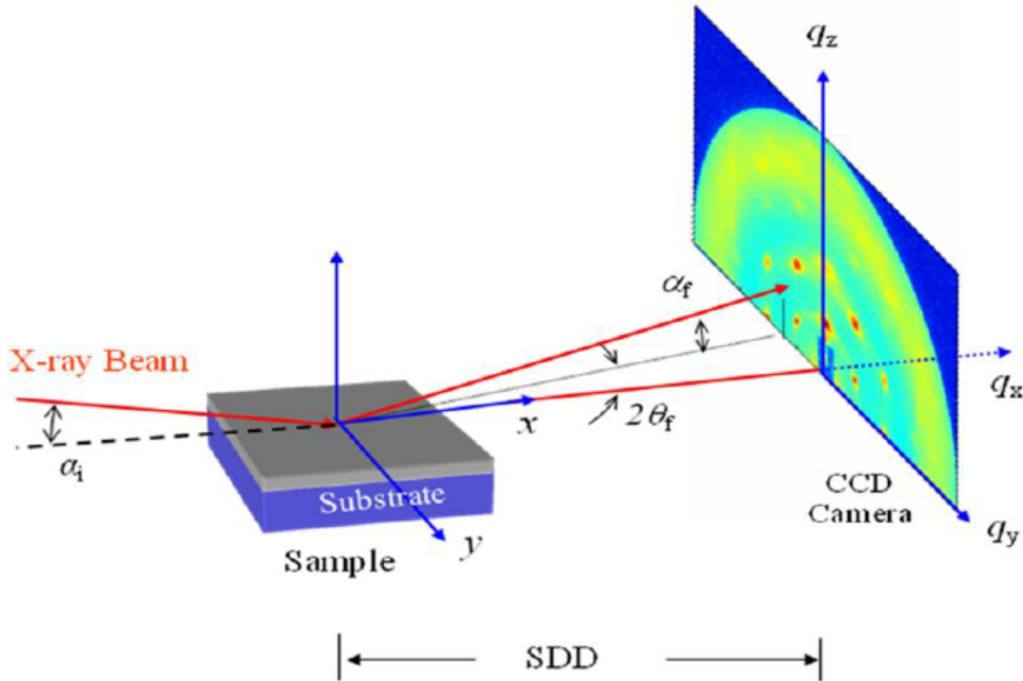
Figure 2.3: Schematic of GIXD set-up with scattering onto a 2D-detector. Printed from [23].

The **s**ample **d**etector **d**istance (SDD) is crucial for converting the pixel coordinates of the detector into reciprocal space coordinates. The setting of the SDD

dictates the area in reciprocal space investigated. Moving the detector closer to the sample, subjects it to scattering with reciprocal vectors of greater length, hence a larger area of reciprocal space is recorded. Optimally, the SDD is chosen in way to capture all relevant diffraction features, but still have a high enough resolution to distinguish those features. The larger the structures under investigation are, the further away the detector can be moved, due to the inverse relation between scattering vectors and molecular structure sizes.

2.5   Rotating GIXD

In addition to setting an angle of incidence ω and the sample detector distance, the sample can also be rotated with ϕ, in the plane perpendicular to the detector and parallel to the substrate surface. Considering samples with uniplanar-axial crystal texture, rotating the crystal leads to scattering with constructive interference from different crystal orientations, at varying rotation angles. Certain reflections of crystallographic net planes only appear at a specific sample orientation. The concept is exemplified in Fig. 2.4, showing diffraction reflexes at specific reciprocal coordinates (q_x, q_y, q_z), that only appear by rotating the crystal, similar to Fig. 2.1 b.). Considering that the consecutively measured GIXD pattern were recorded at different rotation angles, they can be treated as 2D slices through 3D reciprocal space.
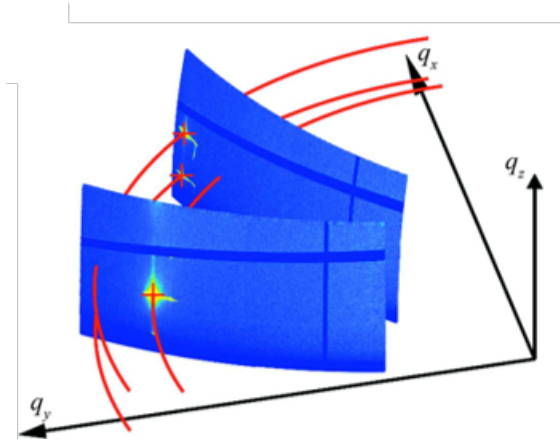
Figure 2.4: Diffraction reflexes appearing and disappearing during sample rotation in GIXD patterns of consecutive measurements. Printed from [20].

Rotating samples without in-plane alignment provides no new information in the form of new diffraction reflexes appearing, underlined by the ring distribution in Fig.

2.1 a.). It does not matter how the crystal is oriented regarding ϕ, all diffraction maxima are present in every 2D slice. Rotating, however, provides better statistics for the intensity values in the GIXD pattern and also their positions. Small shifts of reflex positions, due to inevitable, macroscopic sample misalignment, are smoothed out in a way, if measurements are performed while rotating for a full 360°. Several measurements, from different angles ϕ, can also be summed to improve the signal-to-noise ratio, making diffraction reflexes stand out more above the background. One way to perform such a summation would be the program *GIDVis* [20]. The software provides a plethora of useful tools for GIXD data analysis and displays GIXD pattern in the form of colormaps.

2.5.1 Software tool *GIDVis*

The modular *MATLAB* based application *GIDVis* is used to display recorded GIXD pattern. Using a calibration measurement for the specific set-ups and parameters, allows mapping the recorded intensities from the pixel positions of the detector, to reciprocal space with a physical relevance.

Used features of *GIDVis*, are going to be mentioned in the experimental sections.

Chapter 3

Patterson Method

3.1 Patterson Function

In 1934, Arthur L. Patterson developed and published his method to solve crystal structures by solving the phase problem [24]. His approach was to deploy a Fourier series of indexed intensities, to calculate the relative coordinates of atoms, inside the crystallographic unit cell. The following paragraph is based on Dennis W. Bennett's chapter [25] about experimental methods for solving crystal structures.

The ability of a crystal structure to scatter X-rays is described by an indexed diffraction pattern. For diffraction maxima at specific scattering vectors $\boldsymbol{q}$, Laue indices hkl can be assigned and structure factors F_{hkl} of the intensities can be defined as

$$F_{hkl} = \sum_{j=1}^{n} f_j(q) e^{-2\pi i(h\,x_j + k\,y_j + l\,z_j)}, \tag{3.1}$$

with the atomic scattering factor f_j of atom j, the scattering power of atoms depending on their number of electrons. The positions of atoms inside the unit cell and in regards to each other are therefore decisive in the relative intensity distributions of said structure factors. The electron density $\rho(x,y,z)$ can be calculated by these structure factors and their relative phases, normalized by the volume of the unit cell V_c using

$$\rho(x, y, z) = \frac{1}{V_c} \sum_{hkl} F_{hkl} e^{-2\pi i(h\,x + k\,y + l\,z)} \equiv \frac{1}{V_c} \sum_{\boldsymbol{h}} F_{\boldsymbol{h}} e^{-2\pi i(\boldsymbol{h}\boldsymbol{r})} \tag{3.2}$$

where function values of $\rho(x,y,z)$ show local maxima, where atoms are positioned in the unit cell. Calculating the electron density would require knowledge of the phase, which cannot be measured by X-ray diffraction experiments. The Patterson function

$P(u)$ utilizes the information given by a diffraction experiment to determine parts of a structure or in some cases the whole structure.

Consider an electron density map, where all the atoms in the unit cell are displaced by a vector $\boldsymbol{u}$. Atomic coordinates are chosen as fractional coordinates of the unit cell with $\boldsymbol{r} = (x, y, z) \in [0,1]$. A convolution of the electron densities $\rho(\boldsymbol{r})$ and the displaced $\rho(\boldsymbol{r}+\boldsymbol{u})$ can be defined as

$$P(\boldsymbol{u}) = \int_0^1 \int_0^1 \int_0^1 \rho(\boldsymbol{r})\rho(\boldsymbol{r} + \boldsymbol{u})dxdydz \tag{3.3}$$

and would not be dependent on the atomic coordinates (x, y, z), thus providing a theoretical form of the Patterson function. In this form, the function can be regarded as the superposition of the electron densities of every atom, with every other atom in the unit cell. The nature of the convolution is the reason the function only depends on the distance coordinates between pairs of atoms and is independent of the absolute atomic positions. Inserting Eq. 3.2, with Laue indices $\boldsymbol{h} = (h, k, l)$ for $\rho(\boldsymbol{r})$ and $\boldsymbol{h}'$ for $\rho(\boldsymbol{r}+\boldsymbol{u})$, results in the expression

$$P(\boldsymbol{u}) = \frac{1}{V_c^2} \left(\sum_{\boldsymbol{h}} F_{\boldsymbol{h}} \int_0^{V_c} e^{-2\pi i(\boldsymbol{h}\,\boldsymbol{r})}dV \right) \left(\sum_{\boldsymbol{h}'} F_{\boldsymbol{h}'} e^{-2\pi i(\boldsymbol{h}'\boldsymbol{u})} \int_0^{V_c} e^{-2\pi i(\boldsymbol{h}'\boldsymbol{r})}dV \right) \tag{3.4}$$

Since Laue indices hkl (in vector form $\boldsymbol{h}$) are integer, an integral over $e^{-2\pi i(\boldsymbol{h}+\boldsymbol{h}')\boldsymbol{r}}$ would vanish for all terms but $\boldsymbol{h}' = -\boldsymbol{h}$, getting closer to a practical expression for the Patterson function,

$$P(\boldsymbol{u}) = \sum_{\boldsymbol{h}} F_{\boldsymbol{h}} F_{-\boldsymbol{h}} \, e^{-2\pi i(-\boldsymbol{h}\boldsymbol{u})} \frac{1}{V_c^2} \underbrace{\int_0^{V_c} e^{2\pi i(\boldsymbol{h}-\boldsymbol{h})\boldsymbol{r}}dV}_{= V_c} = \frac{1}{V_c} \sum_{\boldsymbol{h}} F_{\boldsymbol{h}} F_{-\boldsymbol{h}} \, e^{-2\pi i(-\boldsymbol{h}\boldsymbol{u})} \tag{3.5}$$

Using Friedel's law $F_{\boldsymbol{h}} F_{-\boldsymbol{h}} = F_{\boldsymbol{h}}^2$, the structure factors can be replaced by observed intensities $I_O(\boldsymbol{h})$, while trigonometric identities finally lead to the practical form of the Patterson function as

$$P(\boldsymbol{u}) = \frac{1}{V_c} \sum_{\boldsymbol{h}} I_O(\boldsymbol{h}) \cos(2\pi(\boldsymbol{h}\,\boldsymbol{u})), \tag{3.6}$$

which can be evaluated at various points $\boldsymbol{u} = (u,v,w)$, with $u,v,w \in [0,1]$ with observed and indexed intensities of X-ray reflexes. If maxima in $P(\boldsymbol{u})$ occur, $\boldsymbol{u}$ corresponds to a vector between two atoms.

Figure 3.1 shows the electron density of three atoms in a hypothetical 1D unit cell and its resulting Patterson function.
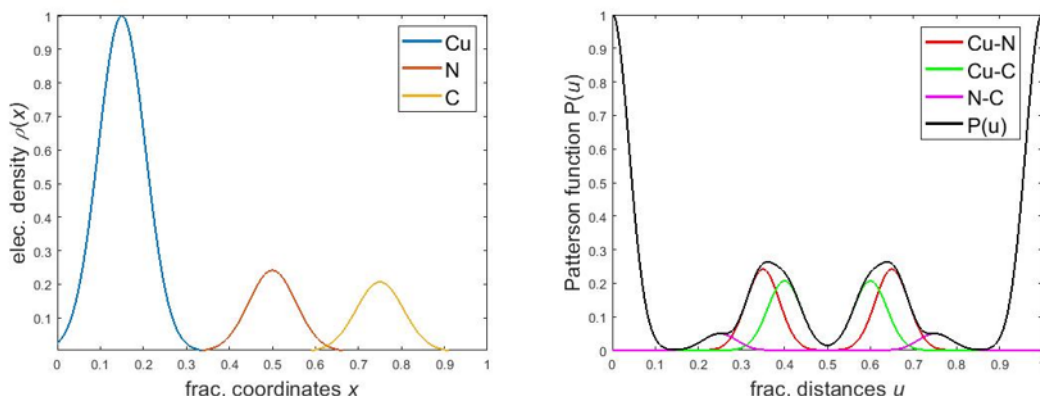
Figure 3.1: Electron density of three atoms in a unit cell (left) and resulting Patterson map and its contributions (right)

For two atoms at positions x_1 and x_2, maxima in the Patterson function $P(\boldsymbol{u})$ can be found at the coordinate $u = |x_1 - x_2|$, so at the distance between two atoms. The equivalent for a 3D unit cell would be the vector $\boldsymbol{u}$ between atoms at $\boldsymbol{r}_1$ and $\boldsymbol{r}_2$. Function values of maxima are proportional to the product of the atom pair's electron densities. While N atoms lead to N peaks in the electron density, a Patterson function will have $N(N\text{-}1)$ unique peaks, one for every atom pair. Additionally, there are N peaks superimposed at $\boldsymbol{u} = (0, 0, 0)$ corresponding to the distances of one atom to itself. These occur for each atom and add up to a very large, so called "origin" peak.

A pair of atoms creates two maxima in Figure 3.1, since there is a vector from atom A to B as well as a vector from B in an adjacent unit cell to A, resulting in a centrosymmetric function $P(\boldsymbol{u}) = P(-\boldsymbol{u})$. In a 3D Patterson function this concept can be extended for seven adjacent unit cells.

The function is also not dependent on a molecules position in a unit cell. Since the function depends only on the interatomic vectors, all starting from the origin, the resulting function is invariant to unit cell translations. Just like the crystallographic unit cell itself, the function space has periodic boundary conditions. All interatomic vectors are always translated to the origin in the Patterson function. If a peak can be found for a vector with e.g. a v component of $v_1 = 0.65$, there will be a peak for its counterpart with $v_2 = 1 - v_1 = 0.35$. This is not an artifact or mathematical effect, but has a physical reason behind it. If the distance between atom A and atom B is larger, than half the length of the unit cell in any dimension, the distance of atom A to atom B' in an adjacent unit cell must be shorter in that direction. Peaks, of more or less the same intensity, occur for both atom pairs and their corresponding

22
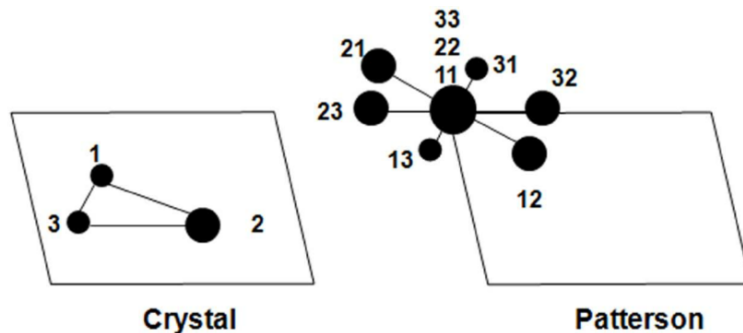
Figure 3.2: Schematic representation of Patterson vectors corresponding to an atomic structure. Printed from [26].

vectors have physical meaning. For analysis sake, these vectors can of course be grouped together, but most of the time the sign of the over-determined component can then be assumed as negative for one of the vectors, since it would be pointing in the opposing direction.

A 2D representation of Patterson vectors and their corresponding structure can be seen in Fig. 3.2. Three atoms in the unit cell result in nine vectors of which three are from one atom to itself and superimposing at the origin. The atomic number of the atom, proportional to the electron density in the unit cell, is indicated by the radii of the spheres. Intensities of corresponding Patterson peaks depend on the product of electron densities of their atom pair.

In the first half of the last century, the Patterson Method was an important analysis tool for crystal structure solutions from single-crystal X-ray diffraction data. Solutions for structures containing heavy atoms were especially achievable, for example the structure solution of Vitamin B_{12} by Dorothy Hodgkin et. al. [27] in 1957.

3.2 Heavy-Atom method and search procedures

Analyzing a Patterson function of a structure containing solely light atoms can be tedious to unpractical, since superimposing peaks of electron densities of very similar magnitude are very hard to distinguish.

The organic molecule pentacenequinone (P2O) crystallizes in a $P2_1/c$ space group and contains only oxygen, besides carbon and hydrogen. Using the solved structure to calculate theoretical values for indexed intensities, the theoretical 3D Patterson function can be determined. The crystal structure of P2O can be seen in Fig. 3.3 and is compared to the structure's Patterson function, looking along the a-direction of both the crystallographic unit cell and the 3D function space. The function was normalized to the intensity of the origin peak, which was set to an arbitrary intensity to visualize function values of high electron density superpositions.
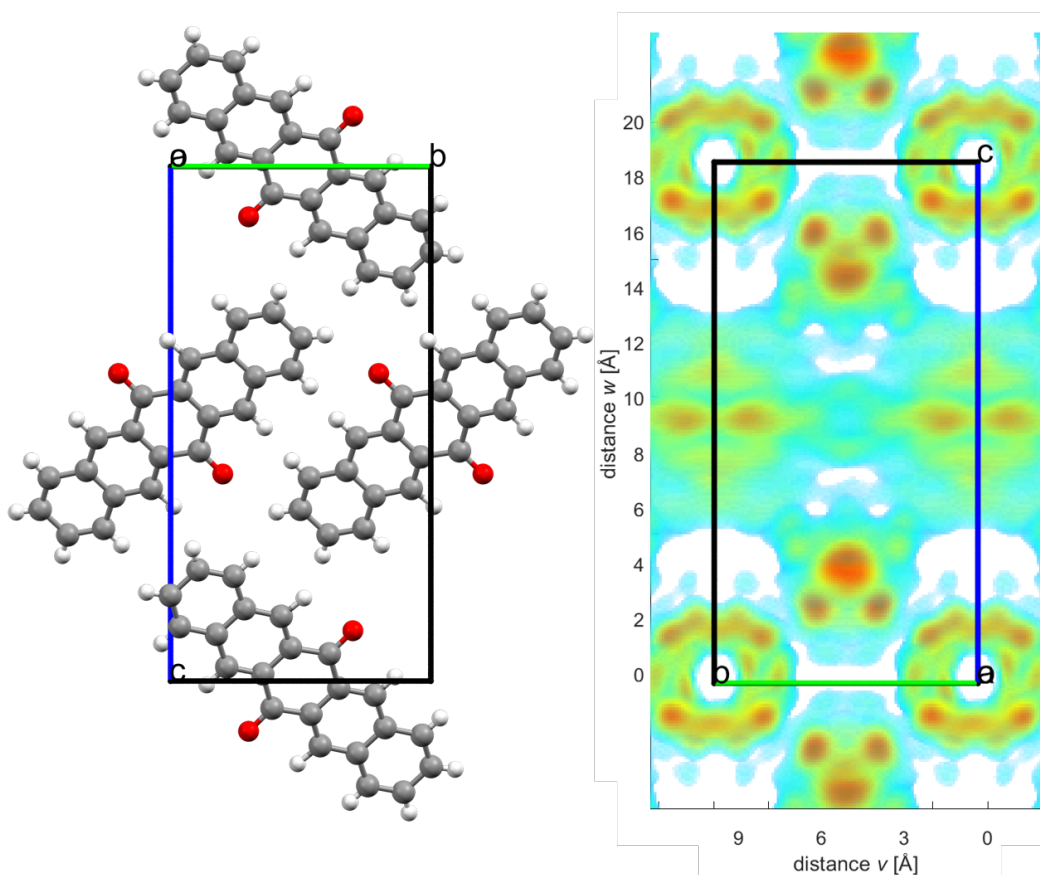
Figure 3.3: Crystal structure of P2O (left) (C (grey), O (red), H (white)) [28] and the theoretical Patterson function scaled to the unit cell (right). Both viewed along the a-direction.

The small electron density difference between carbon and oxygen does not produce a real contrast, to distinguish C-C from C-O correlations. Solely, the slightly higher intensities at roughly $v = 5\,\text{Å}$, $w = 4.5\,\text{Å}$ hint at interatomic vectors between O-O pairs.

If there are a few heavy atoms in a structure, their contributions to a Patterson function stand out noticeably. This makes it possible to assign Patterson maxima to heavy-heavy atom and even heavy-light atom pairs, providing a contrast between specific regions in the function space. The function argument $\boldsymbol{u}$, where these maxima occur, determines the vector between the atom pair.

The ratio for atoms with atomic number Z in a structure should be close to 1

$$r = \frac{\sum\limits_{heavy} Z^2}{\sum\limits_{light} Z^2} \tag{3.7}$$

for the heavy-atom method to be feasible for structural solutions. This is merely a rule of thumb, as for the previous example of vitamin B_{12}, a structure solution could still be achieved with a ratio of 0.14. [29]

Magnitudes of Patterson maxima generally are proportional to the squared electron density maxima, which can simply be expressed by the atomic number of the involved atoms. A pair of C atoms would produce a peak proportional to $Z_C{}^2 = 36$, while a peak of a Cu atom pair would have a height proportional to $Z_{Cu}{}^2 = 841$.

 Copper(II) phtalocyanine (CuPc), seen in Fig. 3.4, is a molecule with an organometallic complex and similar to hemoglobin and chlorophyll. In this case the complex is crystallized in the α-phase, with space group P-1. Cu at the center out-weights the other constituents (C, N, H). Using the same procedure as for P2O, a theoretical Patterson function of CuPc was determined. The resulting Patterson function resembles the actual structure phenomenally well. Even different rings occurring in the structure are in clear contrast to the background. Every interatomic vector between Cu and C or N in the crystal, seems to correspond to a distinct feature in the Patterson function. Intensities of Cu-N correlations can clearly be distinguished from Cu-C peaks. Those peaks would be proportional to $Z_{Cu}Z_C = 174$ and $Z_{Cu}Z_N = 203$. The single Cu atom appears to provide a contrast well enough, to solve the structure by eye and without more sophisticated methods.

Patterson functions of structures with several heavy atoms can be far more challenging to analyze, than the ideal example of CuPc. For structures with more than one heavy atom, there are heavy-heavy atom pairs with intensities almost
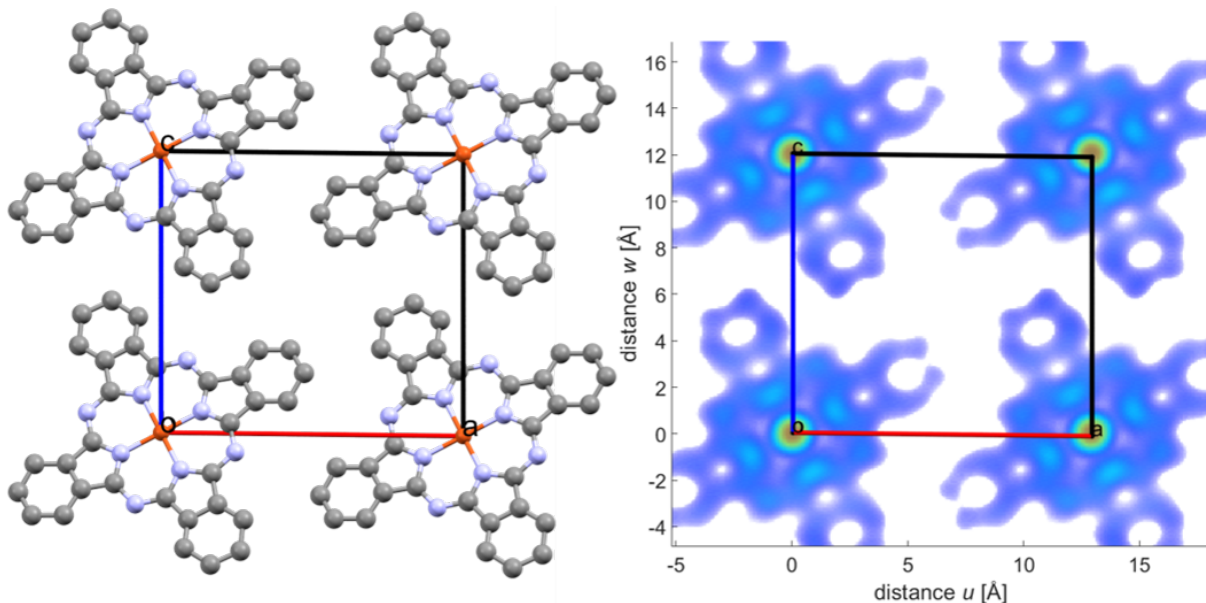
Figure 3.4: Crystal structure of CuPc (left) (Cu (orange), C (grey), N (blue)) [30] and the theoretical Patterson function scaled to the unit cell (right). Both viewed along the *b*-direction.

comparable to the origin peaks and also several additional heavy-light peaks, for every additional heavy atom in the structure. A mix of heavy atoms, with only slight differences in atomic number, makes matters even more complicated. The Patterson function won't resemble the structure, as for CuPc, since every atom's position will now be mapped in relation to more than one heavy atom. Several approaches and concepts can be utilized for a more sophisticated analysis of Patterson functions. Those include *origin removal* and *sharpening* for improving the signal-to-noise by reducing the overshadowing of peaks by origin peak superpositions, the *Patterson Vector Superposition*, symmetry considerations in the form of *Harker lines and planes* and *Fragment Search Methods*, where parts of the structure are already known and their theoretical model functions rotated, translated and compared to the experimental function. Two of those concepts, namely the *Harker* symmetries and the *Superposition Search*, are elucidated in the following sections.

3.2.1 Harker Symmetry

Symmetries occurring in crystal structures determine how atomic positions are related to one another and where equivalent positions of atoms in the asymmetric unit can be found. Those symmetries can be e.g. screw axis or glide planes and are summarized in the space group of the structure. Equivalent positions are dic-

tated by the space groups symmetry operations. Harker symmetries arise from the distance vectors between symmetry related atoms. Relations through rotation axes result in Patterson peaks on characteristic planes and relations through glide or mirror planes on characteristic lines [29]. Interatomic vectors $\boldsymbol{u}_{AB}$ can be defined between atomic position $\boldsymbol{r}_A$ and $\boldsymbol{r}_B$, including symmetry equivalent positions, as

$$u_{AB} = -u_{BA} = r_B - r_A. \tag{3.8}$$

One example for a Harker symmetry is provided by a glide plane along the c axis and perpendicular to the b axis of a crystal with the symmetry equivalent positions $\boldsymbol{r}_1 = (x, y, z)$ and $\boldsymbol{r}_2 = (x, \text{-}y, \frac{1}{2} + z)$. Resulting Patterson peaks accumulate on the line $\boldsymbol{u} = < 0, -2y, \frac{1}{2} >$.

In a second example, space group $P2_1/c$ has four equivalent positions, due to its screw axes and glide planes. These are $\boldsymbol{r}_1 = (x,\ y,\ z)$, $\boldsymbol{r}_2 = (\text{-}x, \frac{1}{2}+y, \frac{1}{2}\text{-}z)$, $\boldsymbol{r}_3 = (\text{-}x, \text{-}y, \text{-}z)$ and $\boldsymbol{r}_4 = (x, \frac{1}{2}\text{-}y, \frac{1}{2}+z)$, resulting in a $2/m$ inversion symmetry, Harker lines and Harker planes:

$$2/m \text{ inversion symmetry:.}$$
$$u_{12} = u_{21} = < -2x, -2y, -2z >$$
$$u_{34} = u_{43} = < 2x, -2y, 2z >.$$
$$\text{Harker lines:}$$
$$u_{14} = u_{41} = < 0, \tfrac{1}{2} - 2y, \tfrac{1}{2} >$$
$$u_{23} = u_{31} = < 0, \tfrac{1}{2} + 2y, \tfrac{1}{2} >.$$
$$\text{Harker planes:}$$
$$u_{13} = u_{31} = < -2x, \tfrac{1}{2}, \tfrac{1}{2} - 2z >$$
$$u_{24} = u_{42} = < 2x, \tfrac{1}{2}, \tfrac{1}{2} + 2z >$$

In case of structures with heavy atoms, finding maxima on Harker sections often leads to a direct way of calculating at least the heavy atom's and its symmetrical equivalent pendants' positions inside the unit cell.

Identifying Patterson maxima on Harker sections, with correlation peaks between symmetry equivalent heavy atoms, opens the possibility to calculate the atomic positions. The coordinates of one atom are assumed at $(x, y, z) = (0, 0, 0)$ and the observed vector (u, v, w) equated with the symmetry operation of the Harker section, where it was found. For Harker planes or lines, either one or two vector components are constant values, making the determination of (x, y, z) possible.

3.2.2 Superposition Search

The idea behind this search method is very simple. First $P(\boldsymbol{u})$ is calculated. The whole function space is then translated, to place a specific peak into the origin at $\boldsymbol{u} = (0,0,0)$. Afterwards, the translated and original Patterson functions are superimposed and new maxima arise. If the Patterson functions have been successfully superimposed, the function should resemble the actual structure, for non-centrosymmetric unit cells. Combining several superpositions of different translations to the origin result, in the optimal case, in peaks reflecting the asymmetric unit. "In theory, a judiciously selected second superposition is generally sufficient to provide the relative positions of the atoms in a non-centrosymmetric unit cell." [25].

This process can also be viewed from the angle of atomic connections. Superimposing two Patterson functions with a specific peak at the origin is the same as, placing one atom arbitrarily at the unit cell origin and a second atom at a position at the end of a Patterson vector. A second vector added to the first connects a third atom, if there exist a third vector in the Patterson function, that is the sum of vector one and two. For additional vectors the same principle has to apply. This is equivalent to combining several superpositions, but considering the real space unit cell. Since even moderately large structures have a large amount of Patterson peaks, this process is arduous and mostly performed by computer algorithms, but for a selected amount of heavy-heavy pair peaks manageable.

Chapter 4

Preparation of the Cu-INA thin film samples

The fINA sample series are metal-organic framework thin films, composed of copper (Cu) metal centers and isonicotinic acid (INA) linkers. The aim of the fINA synthesis was replicating the $Cu(INA)_2$ framework *UFUMUD* [12] or creating a similar metal-organic framework, according to R. Ameloot's group at KU Leuven who prepared the fINA sample series. Contrary to the hydrothermal synthesis of single-crystals grown in solution by Lu & Babb [31], the fINA samples are thin films synthesized on silicon wafers. Inspired by the research on solvent-free synthesis of Cu-INA frameworks by mixing solid reactants [32], [33], the samples were prepared analogous to the previous work on CuBDC [34].

Precursor layer

All 18 samples were prepared on <100> silicon wafer substrates with native oxide. Copper oxide films or copper hydroxide nanobelts were applied as precursors. Copper oxide (CuO) precursor films were deposited on the Si wafers via physical vapor deposition using a magnetron sputter coater and a CuO target and their thicknesses (100 nm, 20 nm and 10 nm) varied through the deposition time. Aligned copper hydroxide $(Cu(OH)_2)$ nanobelt films floating on water are applied by dipping a wafer's surface onto the accumulated floating carpet of fibers. The nanobelts on the wafer should therefore have a preferred alignment along their long axis, which lies also parallel to the sample surface. The Cu-INA frameworks converted from nanobelt precursor films should, in theory, have some form of preferred orientation along the fiber axis parallel to the surface.

Metal-organic framework synthesis

For the conversion of the precursor into a framework, the samples were placed in an evacuated Schlenk tube next to a glass boat containing 500 mg of INA. Samples 04 to 07 were placed in a double-neck Schlenk tube, where 100 µL water was inserted and added during the synthesis, creating humidified conditions. The tube was placed inside a forced convection oven for 16 hours at temperatures 150°C, 175°C and 200°C, depending on the sample. Evaporated INA is engaging with the precursor film in a solid-vapor reaction, incorporating itself into the precursor layer. Samples were thermally activated after the synthesis, removing water and other byproducts from the MOF film.

In Tab. 4.1 synthesis temperatures and precursor thicknesses and types of the 18 samples are listed. While the preparation of fINA11 to 13 was a repetition of fINA01 to 03, their observed structures appear to be fundamentally different.

Table 4.1: List of fINA samples and their synthesis parameters:

Sample	Precursor	T [°C]	Additive
fINA01	CuO 100 nm	200	
fINA02	CuO 20 nm	200	
fINA03	CuO 10 nm	200	
fINA04	CuO 100 nm	200	100 µL H_2O
fINA05	CuO 20 nm	200	100 µL H_2O
fINA06	CuO 10 nm	200	100 µL H_2O
fINA07	$Cu(OH)_2$ nanobelts	200	100 µL H_2O
fINA08	CuO 100 nm	150	
fINA09	CuO 20 nm	150	
fINA10	CuO 10 nm	150	
fINA11	CuO 100 nm	200	
fINA12	CuO 20 nm	200	
fINA13	CuO 10 nm	200	
fINA14	$Cu(OH)_2$ nanobelts	200	
fINA15	CuO 100 nm	175	
fINA16	CuO 20 nm	175	
fINA17	CuO 10 nm	175	
fINA18	$Cu(OH)_2$ nanobelts	175	

Chapter 5

X-ray Diffraction

5.1   In-house set-up for X-ray diffraction

Specular X-ray diffraction scans of all 18 samples of the fINA series were performed using the in-house *Panalytical Empyrean* X-ray diffractometer, in a parallel beam set-up.

Displayed in Fig. 5.1 are the diffractometer and its individual components. Highlighted in red are the X-ray source (1), the parallel beam mirror (3) and the Söller slit (8), which were left unchanged for sample alignments and measurements. The X-ray tube is operated at a voltage/current of 40 kV/40 mA and is emitting Cu-Kα radiation with a wavelength of 1.54187 Å. After passing the parallel beam mirror, the primary beam incident on the sample (6) is monochromatic and parallel. Scattered beams with a horizontal divergence greater than 0.02 rad are blocked by the Söller slit from reaching the detector.

The divergence slit (2), the beam mask (2) and the anti-scatter slit (7), highlighted in green, could be mechanically changed. For sample alignment, a divergence slit restricted the vertical divergence to $\frac{1}{32}$° and for the performance of measurements $\frac{1}{8}$° was used. The narrow anti-scatter slit of 0.1 mm width was used for sample alignment, where the detector (9) uses only one vertical channel. For X-ray diffraction measurements, a wider 8 mm anti-scatter slit was deployed. Beam masks, limiting the beam width to either 10 mm or 4 mm were used, depending on the lateral sample dimension.

Highlighted in blue are devices, controllable and adjustable by the computer. The beam attenuator (4) could be switched off for measurements above $2\theta \approx 6$° and was only active during alignment, protecting the detector from beam damage at
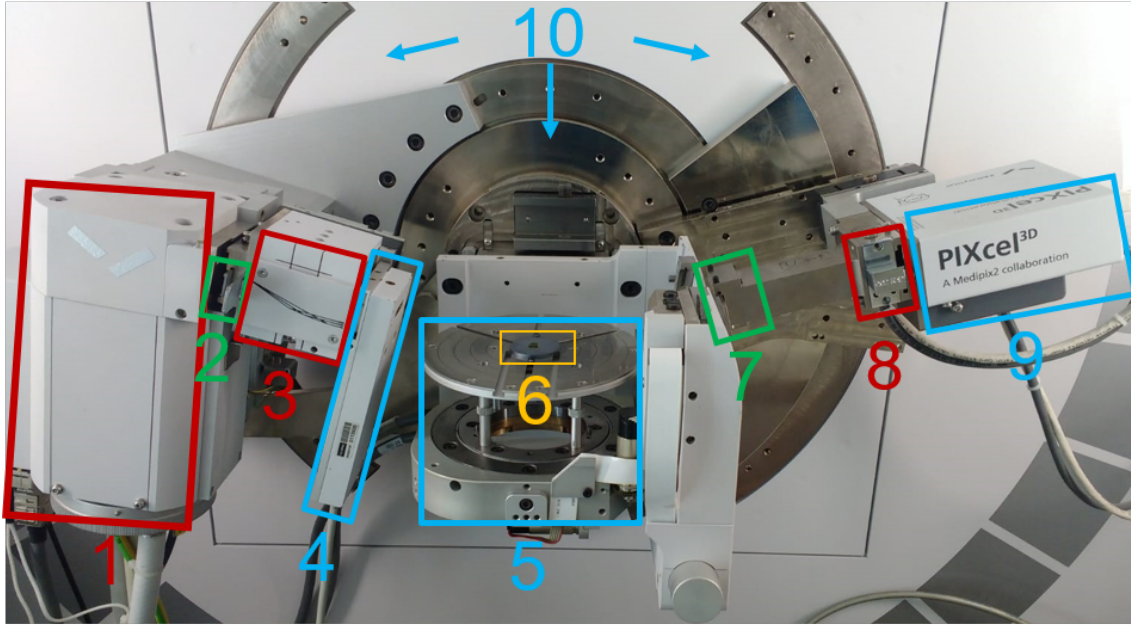
Figure 5.1: *Panalytical Empyrean* diffractometer in a parallel beam set-up: X-ray tube (1), divergence slit and beam mask (2), parallel beam mirror (3), beam attenuator (4), 3-axis cradle (5), positioned sample (6), anti-scatter slit (7), Söller slit (8), *PIXcel*^{3D} detector (9) and goniometer motor and turning circle (10).

small incident angles. The 3-axis cradle (5) was used for the alignment of the sample height and the goniometer (10) for variation of ω and 2θ during the experiment.

5.2 $\theta/2\theta$ scans of the fINA sample series

With the *PIXcel*^{3D} detector in a scanning line configuration, where all 255 vertical channels are used, $\theta/2\theta$ scans were performed in a range from $2\theta = 8°$ to $50°$. Diffraction patterns of all 18 fINA samples were converted from 2θ to q via Eq. 2.5 and are presented in the following figures. The forbidden Silicon 200 peak (see [35]) was removed from the diffractograms and its position marked accordingly.

Diffractograms in Fig. 5.2 for fINA01 to fINA03 show peaks associated with the MOF at $q = 0.85\,\text{Å}^{-1}$ and $q = 1.21\,\text{Å}^{-1}$ and an additional peak at $q = 0.96\,\text{Å}^{-1}$, only featured in fINA02. Interestingly, the diffraction patterns of these first three samples, differ substantially from those of later samples.

A new set of diffraction peaks, associated with the MOF structure, can be seen in Fig. 5.3 for fINA04 to 07, at $q = 1.42\,\text{Å}^{-1}$, $2.13\,\text{Å}^{-1}$ and $2.84\,\text{Å}^{-1}$. Since they
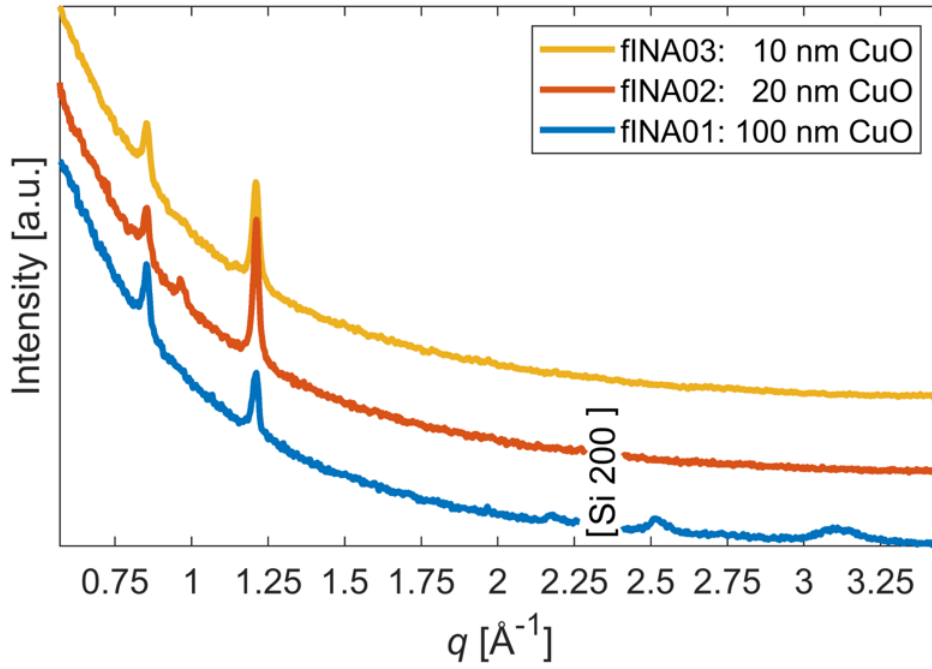
Figure 5.2: Specular scan of fINA01, fINA02 and fINA03.

evidently appear every $0.71\,\text{Å}^{-1}$, the two later peaks seem to be higher orders of the $1.42\,\text{Å}^{-1}$ peak, in terms of their Laue indices *hkl*. An additional diffraction peak at $q = 0.71\,\text{Å}^{-1}$, would also be expected for these equidistant peaks and under close inspection, the diffractogram of fINA04 also shows hints of a peak at $0.71\,\text{Å}^{-1}$. For clarity, accompanying measurements with a far higher exposure time, in the range of $2\theta = 9°$ to $11°$ were recorded. Although the measurements in Fig. 5.4 are still noisy to some degree, at least for fINA04, a diffraction peak at $q = 0.71\,\text{Å}^{-1}$ could indeed be confirmed.

Despite featuring the prominent MOF peak at $q = 1.42\,\text{Å}^{-1}$, the samples 08 to 10 in Fig. 5.5 also show a new diffraction maximum at $q = 1.07\,\text{Å}^{-1}$. Even though not visible in the logarithmic depiction in Fig. 5.3, this peak is also present in the diffractogram of fINA07, but far less intensive.
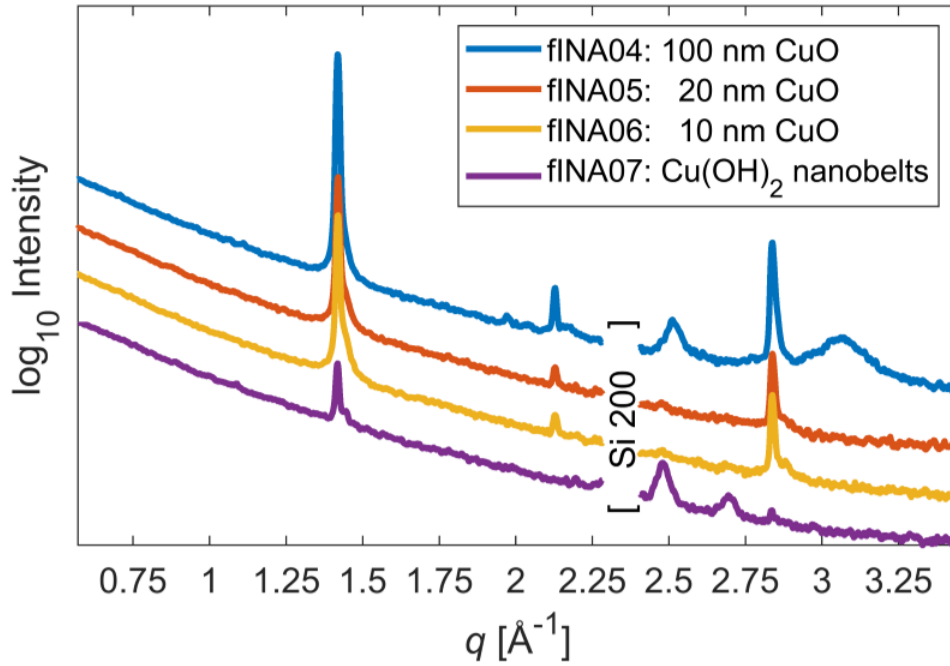
Figure 5.3: Specular scan of fINA04, fINA05, fINA06 and fINA07, with intensities in logarithmic scale.
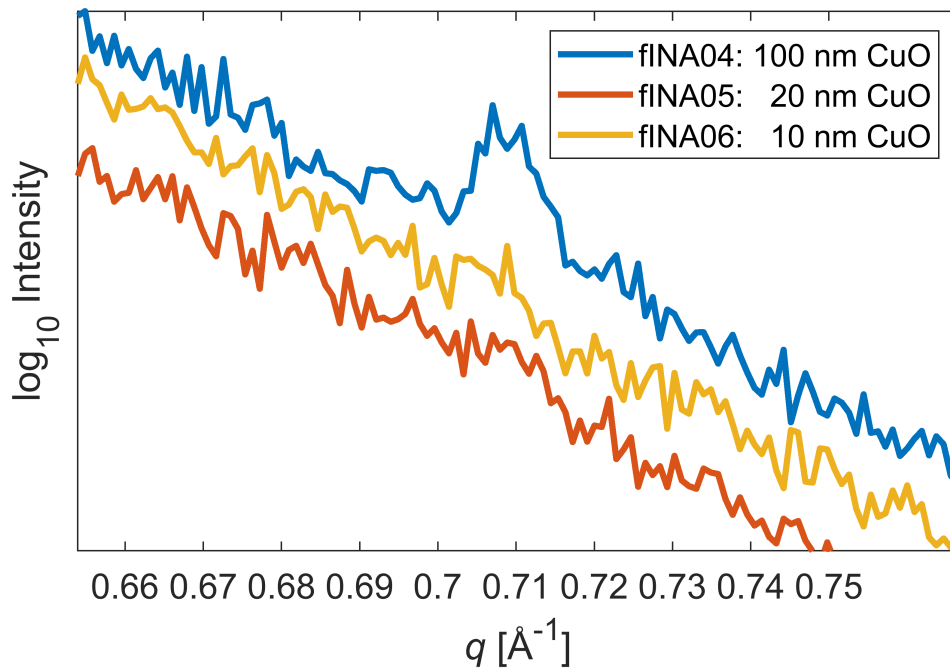
Figure 5.4: Specular scan with high exposure time of fINA04, fINA05 and fINA06, with intensities in logarithmic scale.

In Fig. 5.6, the diffraction patterns of fINA11 to 14 are resembling those in Fig. 5.3 of fINA04 to 07, with the exception of fINA12 and 13's unique, broad
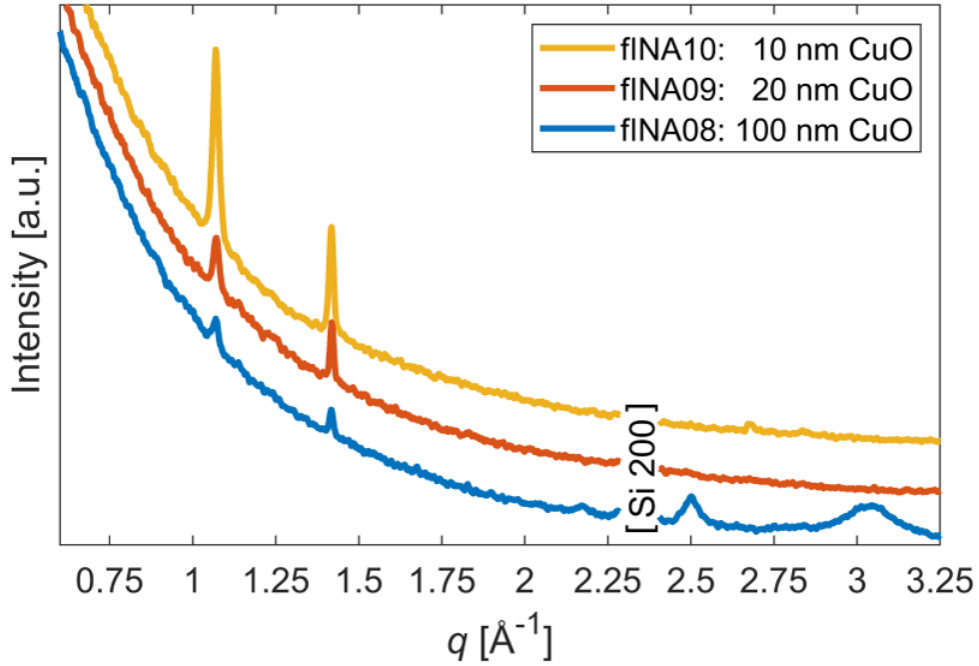
Figure 5.5: Specular scan of fINA08, fINA09 and fINA10

maxima at $q = 1.83\,\text{Å}^{-1}$. The peak around $q = 0.71\,\text{Å}^{-1}$ in fINA13's diffraction pattern, is far more intensive than in the pattern of fINA04.

Akin to fINA08, 09 and 10, the diffraction pattern of fINA15 in Fig. 5.7 features the peak at $q = 1.07\,\text{Å}^{-1}$. This peak is exactly between the first and the second MOF peak and therefore also belongs to the MOF peak series. The index corresponding to the reciprocal lattice vector (Eq. 2.3) normal to the surface, represents the order n of those peaks and is always an integer. If the order of the four previously discussed MOF peaks would be an odd integer, the order of the intermediate peak would be even and vice versa. Hence, fINA08, 09, 10 and 15 very likely have the same crystallographic unit cell or at least the lattice vector normal to the surface is the same, as for the samples with the equidistant MOF peaks starting at $q = 1.42\,\text{Å}^{-1}$.

In fINA16 and 17, only the second and fourth of the MOF peak series are present, a phenomenon also observed in other samples. While the first and third MOF peak seem to have no or only low intensities, the second and fourth are the prominent maxima in the diffraction patterns of fINA 04, 05, 06, 12, 13, 16 and 17.

Sample 16 also featured a Si 111 diffraction peak at $q = 2\,\text{Å}^{-1}$, present due to randomly aligned Si dust from cutting the wafer.
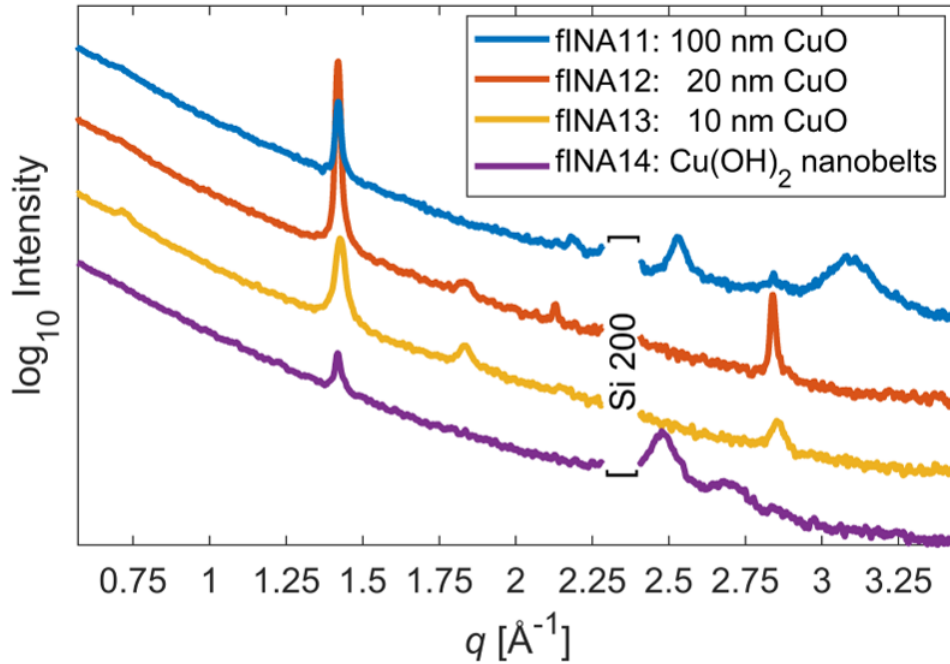
Figure 5.6: Specular scan of fINA11, fINA12, fINA13 and fINA14, with intensities in logarithmic scale.

Omitting fINA01 to 03, the whole sample series featured diffraction peaks belonging to, what appears to be, just one structure. Laue indices hkl in Tab. 5.1 refer to a indexing solution from later chapters. Only a few, low-intensity maxima are inconsistent. Recorded prior to the synchrotron beamtime, information from the specular scan influenced expectations and preparations for GIXD experiments on the samples.

Table 5.1: Cu-INA metal-organic framework diffraction maxima:

hkl	q [Å^{-1}]	fINA
002	0.71	04, 13
003	1.07	07, 08, 09, 10, 15
004	1.42	04-18
006	2.13	15
008	2.84	04-06, 11-13, 16, 17
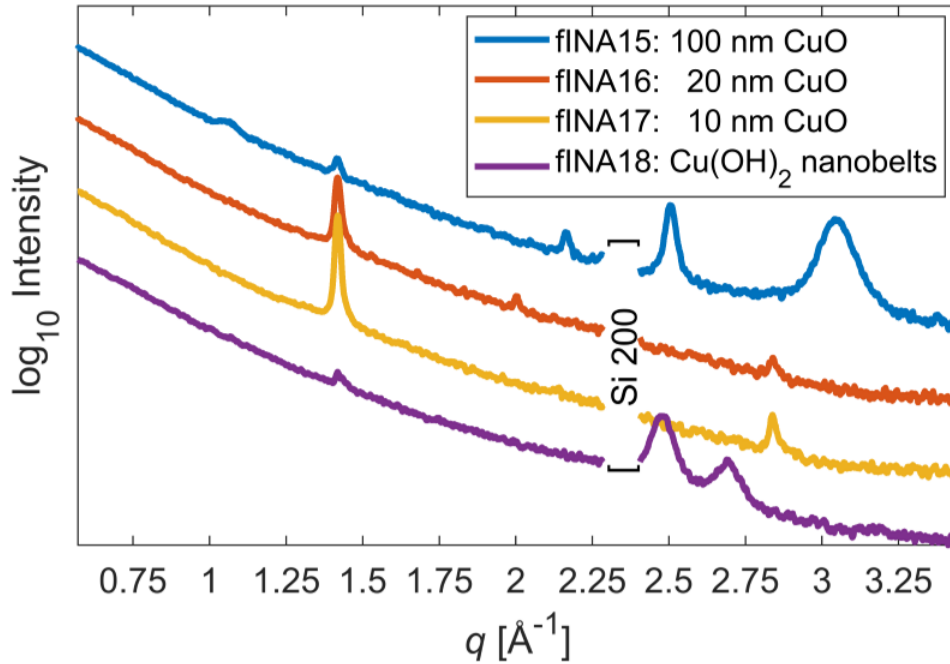
Figure 5.7: Specular scan of fINA15, fINA16, fINA17 and fINA18, with intensities in logarithmic scale.

5.2.1 Residual Copper Oxide

Copper oxide (CuO) diffraction maxima can be seen in the pattern of several samples and their intensities correlate with the reported CuO precursor thicknesses. Samples with a CuO layer thickness of 100 nm, feature peaks of CuO 110 at $q = 2.28\,\text{Å}^{-1}$ and 002, 11-1 and 111 around $q = 2.5\,\text{Å}^{-1}$. Slightly above $q = 3\,\text{Å}^{-1}$ is also a broad peak coinciding with the Cu 111 and CuO 201 and 11-2 peaks. These maxima indicate the presence of a significant amount of not-converted CuO. Residual CuO suggests a self limiting solid-vapor reaction synthesis process, resulting in similar MOF film thicknesses, regardless of the precursor thickness. Correlations between the intensities of MOF and residual CuO peaks are also apparent in Fig. 5.2 and Fig. 5.5. Intensities of MOF and CuO peaks are inversely related.

5.2.2 Copper Hydroxide nanobelts

Diffraction patterns of all samples with a nanobelt substrate only seem to feature the intensive MOF peak at $q = 1.42\,\text{Å}^{-1}$ and at most the intermediate peak at $q = 1.07\,\text{Å}^{-1}$ for fINA07. Strangely, the two broad substrate peaks, appearing for all nanobelt samples between $q = 2.5\,\text{Å}^{-1}$ and $2.75\,\text{Å}^{-1}$, belong to CuO and potentially Cu_2O, but not $Cu(OH)_2$. Copper hydroxide is metastable and a decomposition

process producing CuO and H_2O is known to occur [36]. Since the samples were synthesized almost two years before the XRD experiments, this hypothesis seems plausible.

Chapter 6

Grazing Incidence X-ray Diffraction

Measurements were carried out at the *XRD1* beamline at the *Elettra* synchrotron facility. Before measurements could be carried out, a sample detector distance (SDD) had to be set, which required an accompanying calibration measurement. Knowing roughly in what range of q to expect diffraction maxima from the specular scans, a SDD of 200 mm was chosen. At the chosen distance a GIXD pattern of a LaB_6 powder sample (NIST standard) featuring very sharp Debye-Scherrer rings was recorded. The calibration tool in *GIDVis* is creating a mapping between the pixel positions recorded by the detector and reciprocal space coordinates, by using the known diffraction rings of LaB_6 as a reference. This enables a visualization in a physically meaningful measure for recorded GIXD scans, where intensity values are displayed at the reciprocal space coordinates $\boldsymbol{q} = (q_{xy}, q_z)$. As a result of this mapping, a wedge shaped area can be seen in the GIXD pattern. Reciprocal space positions within this area are not accessable for detection and the size and shape of the wedge depend on the incident angle ω. A specular scan provides a diffractogram along the q_z direction, which can not be accessed in GIXD experiments. Therefore the information gathered by both experiments is complementary. Due to the mosaicity of the crystallites in the fINA samples, intensities from specular diffraction peaks can partly be seen distributed left and right of the wedge.

For every fINA sample, several static measurements were recorded by variation of the incident angle ω. A subsequent rotating GIXD measurement was performed with higher exposure times at selected incidence angles.

6.1 Grazing Incidence X-ray Diffraction Pattern of CuO samples

The diffraction patterns of samples with CuO precursor films showed no sign of *axial* orientation, only *uniplanar* orientation [17]. Therefore, rotating GIXD measurements were solely performed for better statistics of the recorded diffraction maxima. While rotating the sample by 360° in total, six GIXD patterns were recorded by integrating the measured intensity for 60° of rotation, respectively. The software *GIDVis* has the option to sum up the intensities of several selected measurement files, making it possible to add-up intensity values of six GIXD scans obtained during rotation. For the following figures depicting the GIXD patterns, it is specified if the pattern is displayed with a linear or logarithmic scale for the intensity and if the displayed scan was a single measurement or if it was summed up.
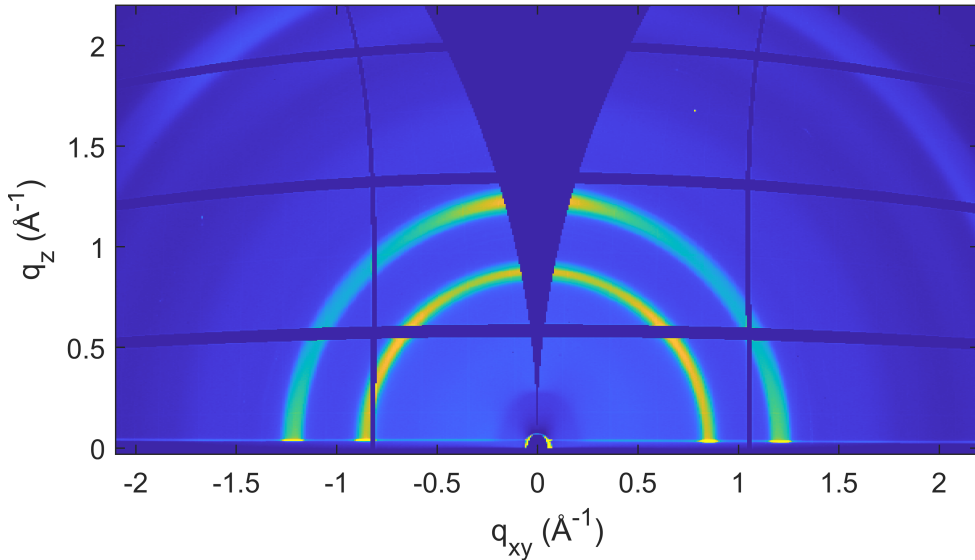
Figure 6.1: Linearly displayed GIXD pattern of sample fINA01 at incident angle $\omega = 0.2°$.

Diffraction maxima are azimuthally smeared arcs, rather than circular spots, due to the slight mosaicity of the otherwise out-of-plane aligned crystallites. Depending on the incidence angle, diffraction maxima are also radially smeared. At lower incidence angles, larger areas of the samples get illuminated and despite the best efforts during alignment, sample surfaces are not necessarily perfectly perpendicular to the detector surface. A good illustration of the scope of this effect are the Si 111 peaks in Fig. 6.3, showing two azimuthally shifted peaks with radial smearing,
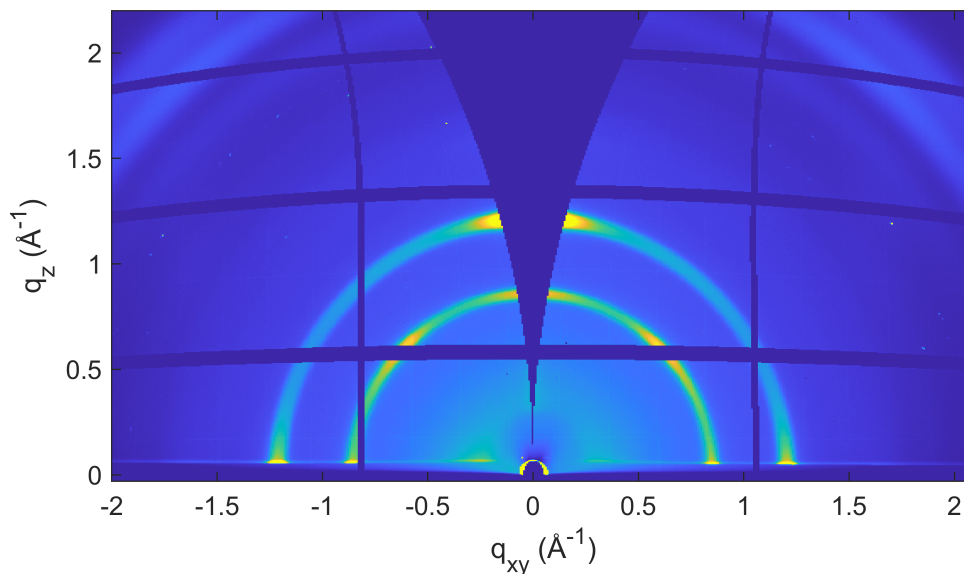
Figure 6.2: Linearly displayed reciprocal space map of summed up rotational GIXD patterns of the sample fINA02 at incident angle $\omega = 0.5°$.

instead of sharp single-crystal peaks. Those shifted peaks appeared 180° apart during rotation, indicating some wobbling of the sample. Slight wobbling can be overlooked as long as the peak shift from the theoretical position is uniform for both appearing maxima and summation of scans obtained during rotation mitigate this effect.

The diffraction pattern of fINA01 (Fig. 6.1), fINA02 (Fig. 6.2) and fINA03 (Fig. 6.3) are inherently different from the remaining samples. Structures of samples 01 to 03 are therefore a distinct phase. Besides some lower intensities around $q = 2.5\,\text{Å}^{-1}$ from the CuO substrate, the only diffraction maxima are the broad rings at $q = 0.85\,\text{Å}^{-1}$ and $q = 1.21\,\text{Å}^{-1}$. Intensity distributions of the rings nonetheless indicate some form of preferred *uniplanar* orientation for a high percentage of crystallites. The rings show higher intensities in the form in-plane peaks at $q_z = 0$, as well as accumulation at the edge of the wedge towards $q_{xy} = 0$. Those peak positions are in agreement with the specular scan. More noticeable in fINA02 and fINA03, the inner ring also features a higher intensity distribution at roughly 45°. The diffraction maximum can either be attributed to a maximum not related to the peak seen in the specular scan or be the same peak, but from crystallites with a tilt in regard to the contact plane. The specular scan of fINA02 shows a noticeable, albeit less intensive, peak at $q = 0.96\,\text{Å}^{-1}$. Strangely, despite the two rings coinciding with the specular peaks, the $q = 0.96\,\text{Å}^{-1}$ peak is not present in any form in the GIXD
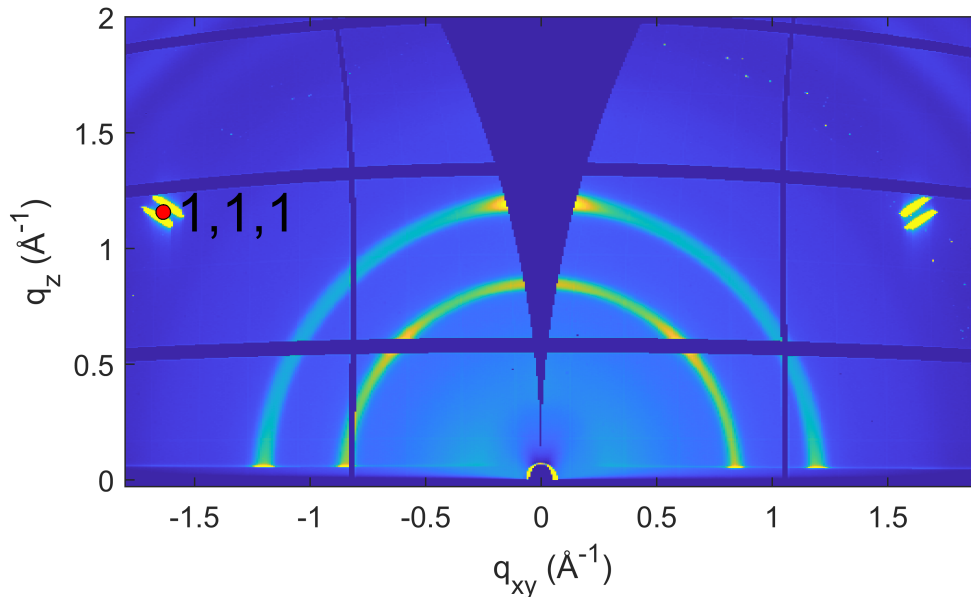
Figure 6.3: Linearly displayed and summed GIXD pattern of sample fINA03 at incident angle $\omega = 0.5°$

pattern in Fig. 6.2.

Similarities in diffraction patterns for fINA04 to fINA18 were to be expected, from comparing the specular scans. In a first step to solve the crystal structure of the presented Cu-INA framework, the crystallographic unit cell was determined through indexing. The GIXD patterns in the following figures are already compared to theoretical maxima positions for a solution of the unit cell.

A small excursion into Indexing

Indexing describes the determination of the crystallographic unit cell parameters through assigning systematically varied Laue indices *hkl* to diffraction peaks. Since solutions for unit cells are non-unique, several variations of parameters could describe the same pattern and generally, the solution whose theoretical maxima positions deviate the least from experimental peak positions, is accepted.

An in-house algorithm makes indexing of grazing incidence diffraction peaks from thin film samples possible. Implementations of the algorithm and its mathematical backbone are thoroughly described in the work of J. Simbrunner et al. [37].

Sample 04 was chosen for the indexing, because it featured the highest number of distinguishable peaks and the examined measurement was performed at a relatively high incidence angle of 3°. At higher incidence angles, intensities of substrate peaks unfortunately increase substantially and the otherwise visible in-plane peaks at $q_z =$

0 Å^{-1} are lost, but radial smearing gets diminished, resulting in sharper peaks. Using the *Peak Finder* module in *GIDVis*, diffraction peak positions could be precisely determined via a Gaussian fit, despite the azimuthal smearing of the peaks.
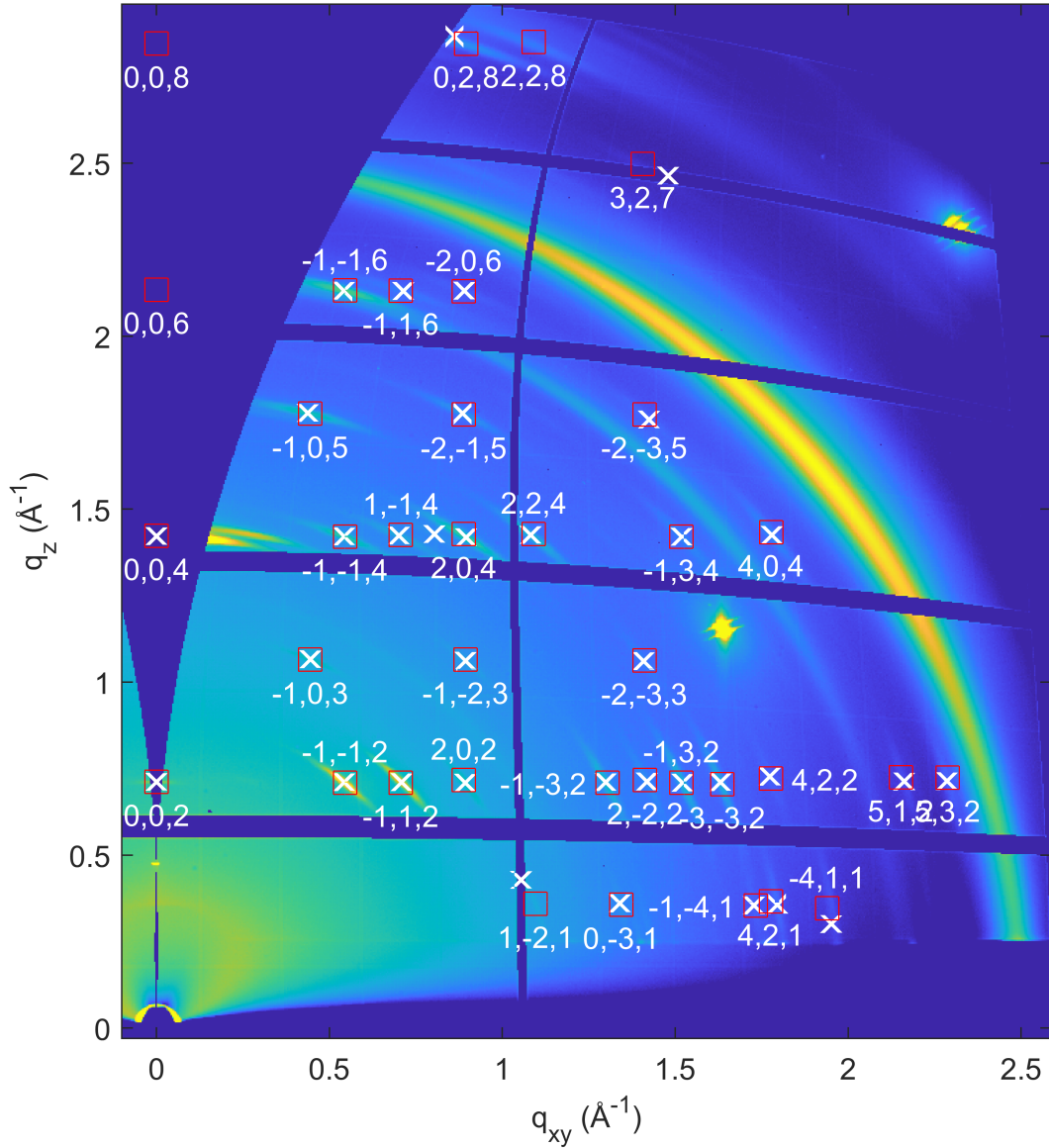
Figure 6.4: Logarithmically displayed and summed GIXD pattern of sample fINA04 at incident angle $\omega = 3°$. Peak positions fed into the indexing algorithm (white crosses) and theoretical peaks (red squares) of the unit cell solution and their Laue indices are indicated.

The diffraction pattern visualized in Fig. 6.4 was recorded at $\omega = 3°$ and can therefore barely be labeled as "grazing incidence" anymore. Marked in white crosses are peak positions provided to the indexing algorithm, while the red squares depict

Table 6.1: Unit cell parameters determined through indexing:

a, b, c, α, β, γ...Lattice parameters of the unit cell.

(uvw)...Crystallographic plane parallel to the substrate surface.

a	b	c	α	β	γ	(uvw)
14.616 Å	14.503 Å	17.667 Å	90.07°	90.33°	75.36°	(001)

theoretical diffraction maxima positions and their Laue indices, corresponding to the unit cell determined by the indexing. The lattice parameters and contact plane orientation of the triclinic unit cell are displayed in Tab. 6.1.

Besides loading reported and solved structures in the form of *.res* files, the *Crystal Module* in *GIDVis* allows typing in unit cell parameters and contact plane orientations and in turn display the corresponding theoretical diffraction peaks of the crystal. Theoretical diffraction peaks of the unit cell in Tab. 6.1, fitting to experimental peaks, were plotted as an overlay to the GIXD patterns. It has to be emphasized, that the theoretical diffraction maxima derived from fINA04 were more or less in coherence with the GIXD patterns of samples 05 to 18.
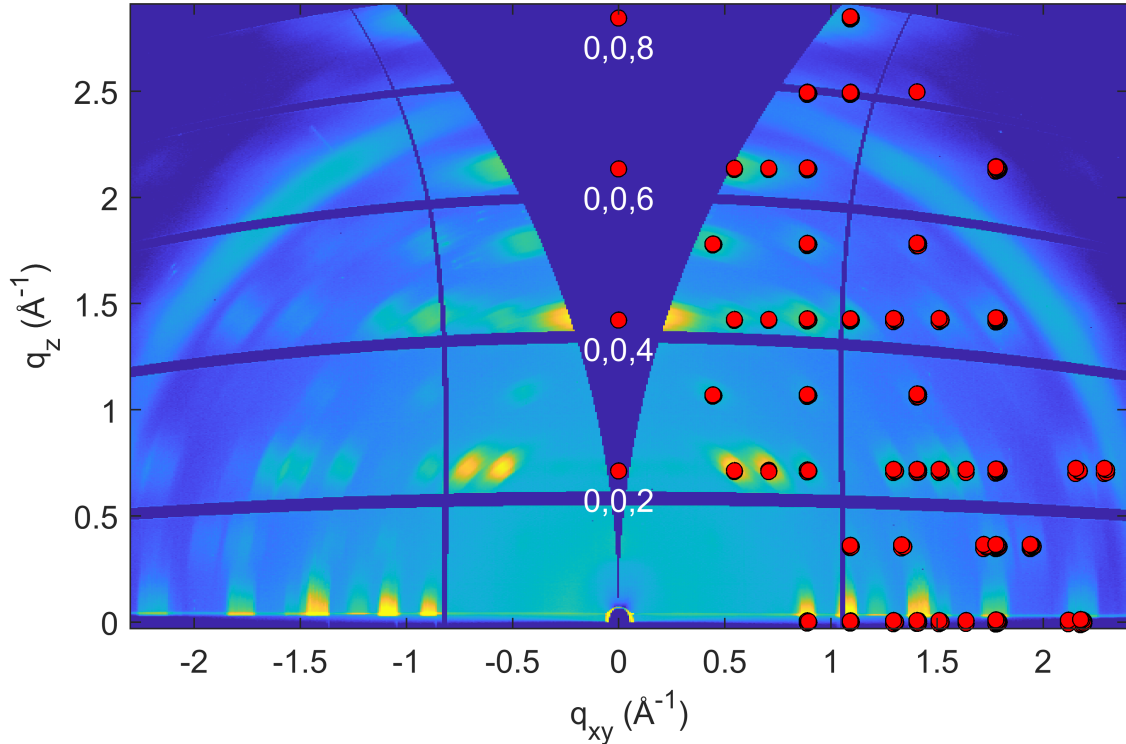
Figure 6.5: Logarithmically displayed GIXD pattern of sample fINA04 at incident angle $\omega = 0.2°$, with theoretical diffraction peaks indicated.

The measurement in Fig. 6.5, recorded at real "grazing incidence" angle of 0.2°

is showing a more complete picture of the diffraction pattern of fINA04. The effects of the film sensitive penetration depth are immediately apparent. The conspicuous, broad ring around $q = 2.5\,\text{Å}^{-1}$ belonging to CuO is far less intensive in Fig. 6.5 as in Fig. 6.4 and the ring seen around $q = 2.2\,\text{Å}^{-1}$ in Fig. 6.4 completely vanishes, leaving no doubt about his origin not being rooted in the CuO precursor.
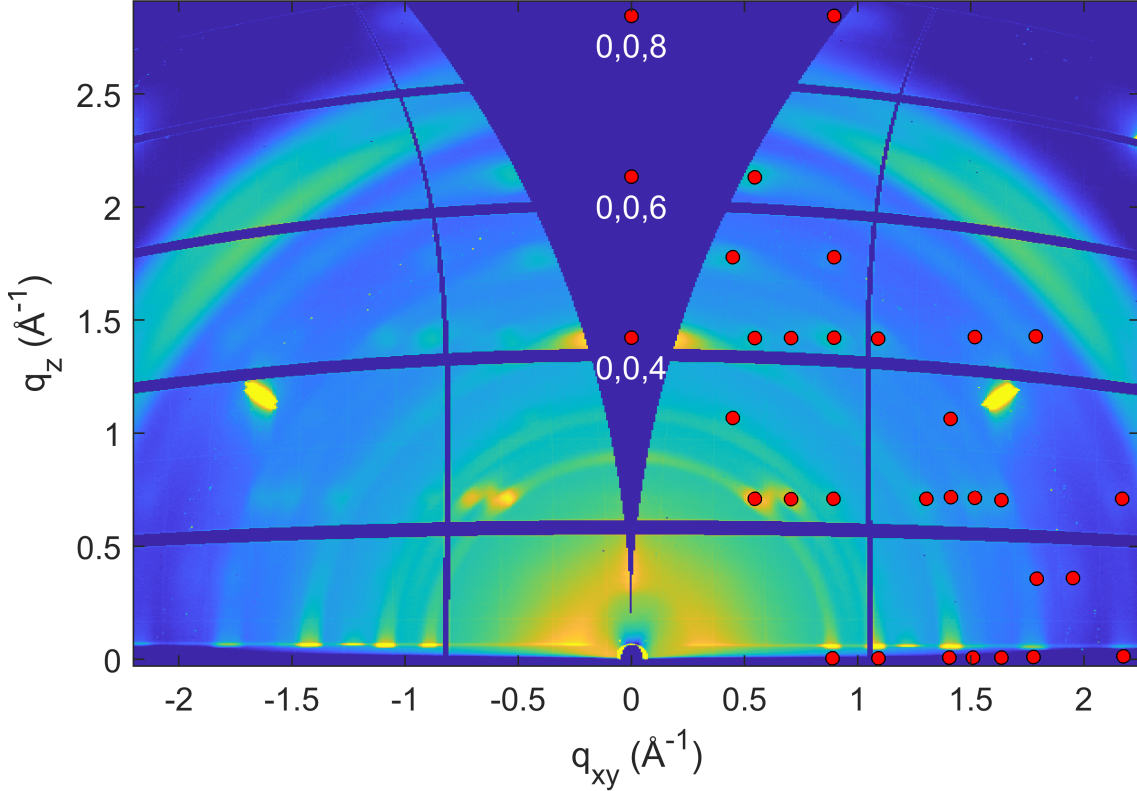
Figure 6.6: Logarithmically displayed GIXD pattern of sample fINA05 at incident angle $\omega = 0.5°$, with theoretical diffraction peaks indicated.

Diffraction peaks with odd values for the index l appear to be less frequent and their other two indices hk combinations not shared by peaks with even l at lower and higher q_z. In other words, these odd row peaks don't appear to be higher orders, repeating peaks from even rows below, in regards to l. For example the ± 103 and ± 105 appear to have intensities, while the $\pm 1 \pm 13$, $\mp 1 \pm 13$ etc. appear to have extinct intensities. Due to these odd row peaks the unit cell length $c = 17.667$ Å is also twice in length, even though a length of 8.83 Å sufficiently describes the diffraction peaks in even rows, as well as the specular scans of most fINA samples. One could argue about the impact of added water on the structure during synthesis, leading to more pronounced and distinguishable diffraction peaks. Water occupying void spaces in the MOF and keeping the framework upright is one speculation.

The GIXD pattern of fINA05 recorded at $\omega = 0.5°$ (Fig. 6.6) and fINA06 at $\omega = 1.0°$ (Fig. 6.7) look mistakenly similar, with the exception of the slightly more prominent CuO precursor diffraction ring for fINA05. The structure is clearly related to fINA04 and theoretical peaks also fit well, but the appearance of diffraction peaks, especially in odd l rows, is less common. In addition to that, the more intensive peaks exhibit accompanying rings, suggesting some MOF crystallites are randomly aligned, but with a statistical tendency for the c-vector of the lattice to be perpendicular to the surface.
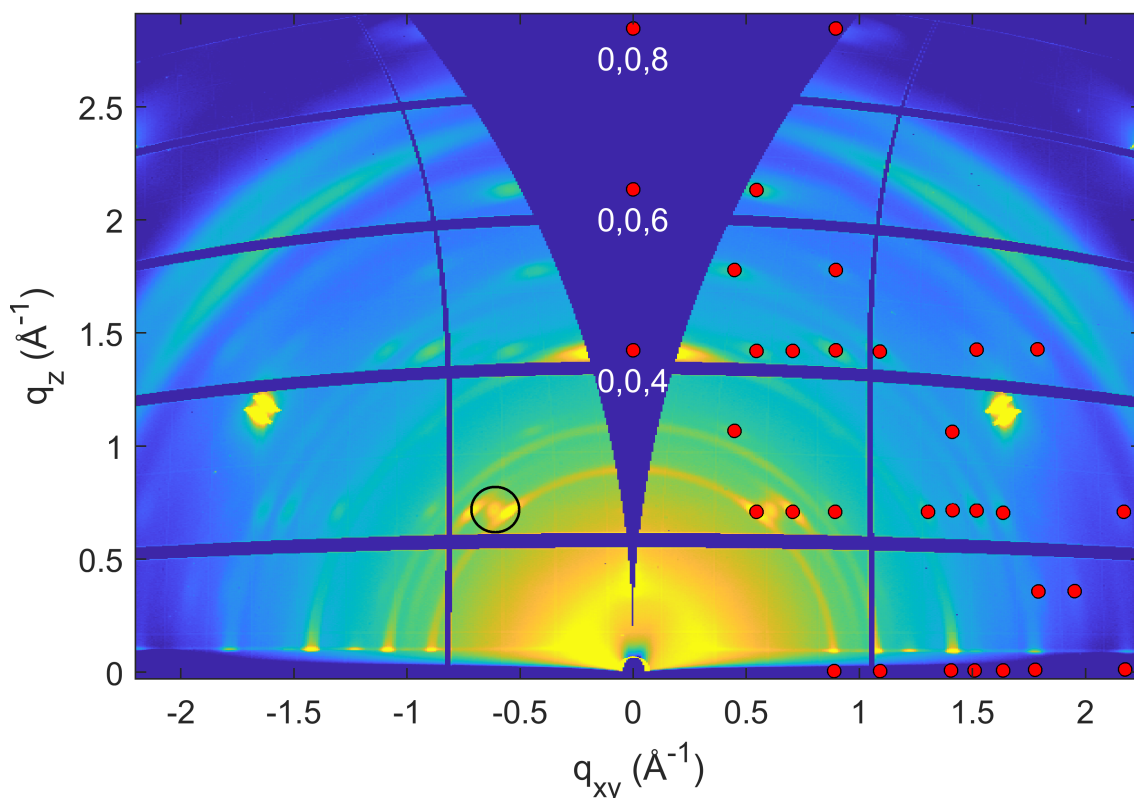
Figure 6.7: Logarithmically displayed and summed GIXD pattern of sample fINA06 at incident angle $\omega = 1.0°$, with theoretical diffraction peaks indicated and unknown features highlighted.

Both samples show these spherical features (highligthed in Fig. 6.7) between the ± 112 and 112 peaks, which to not fit to any theoretical diffraction maximum and their shape also suggests that they don't belong to the MOF film. While the Cu-INA peaks are azimuthally smeared, these features are spherical.
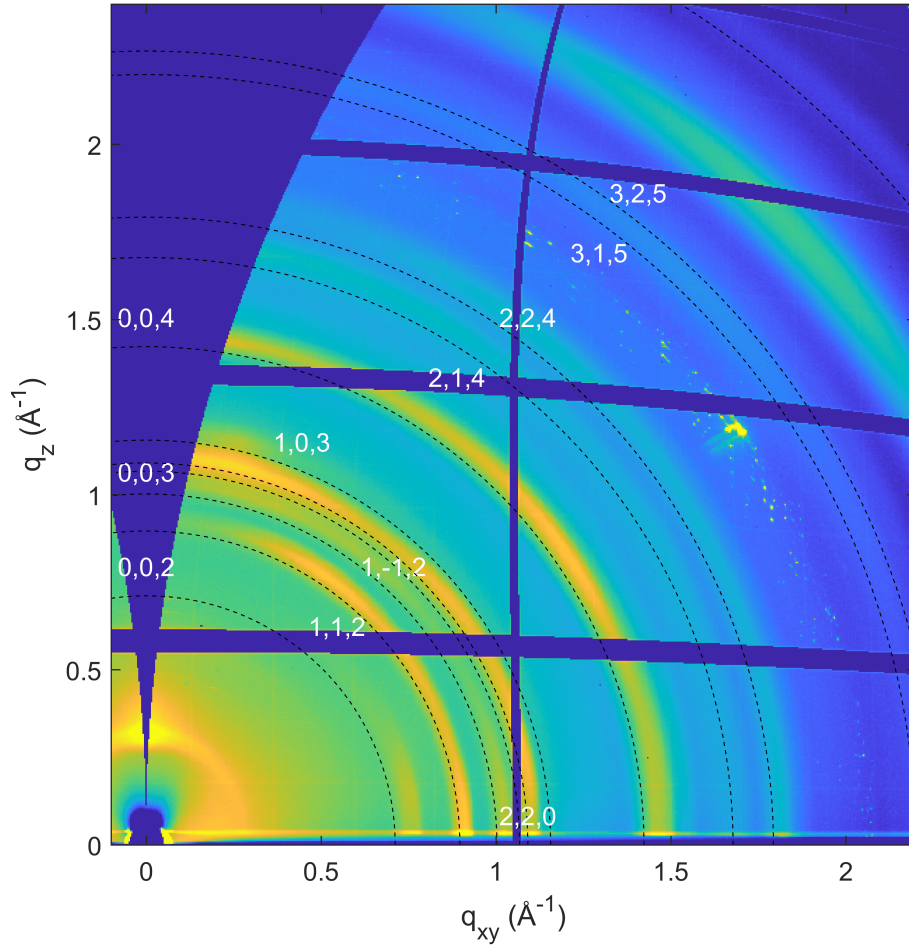
Figure 6.8: Indexed and logarithmically displayed GIXD pattern of sample fINA08 at incident angle $\omega = 0.2°$.

On first glance the theoretical diffraction pattern derived from fINA04 does not align with the diffraction rings of fINA08 seen in Fig. 6.8. The rings all appear to have q values, that are slightly higher than the theoretical values, but the spacing between the diffraction rings appears to be the same as for the theoretical rings. Lattice lengths that are a little shorter for this samples structure could be the cause of this shift. The high intensity rings at $q = 1.08\,\text{Å}^{-1}$ and $q = 1.44\,\text{Å}^{-1}$ are more or less in agreement with the specular scan, where this shift was not recognized previously.

Evidence for the structure's relatedness to the previously discussed samples are also the intensities of the rings. Comparable intensities are observed in the rings' corresponding diffraction peaks in e.g. Fig. 6.5, where 112, -112 and 004 peaks are also the dominating maxima.
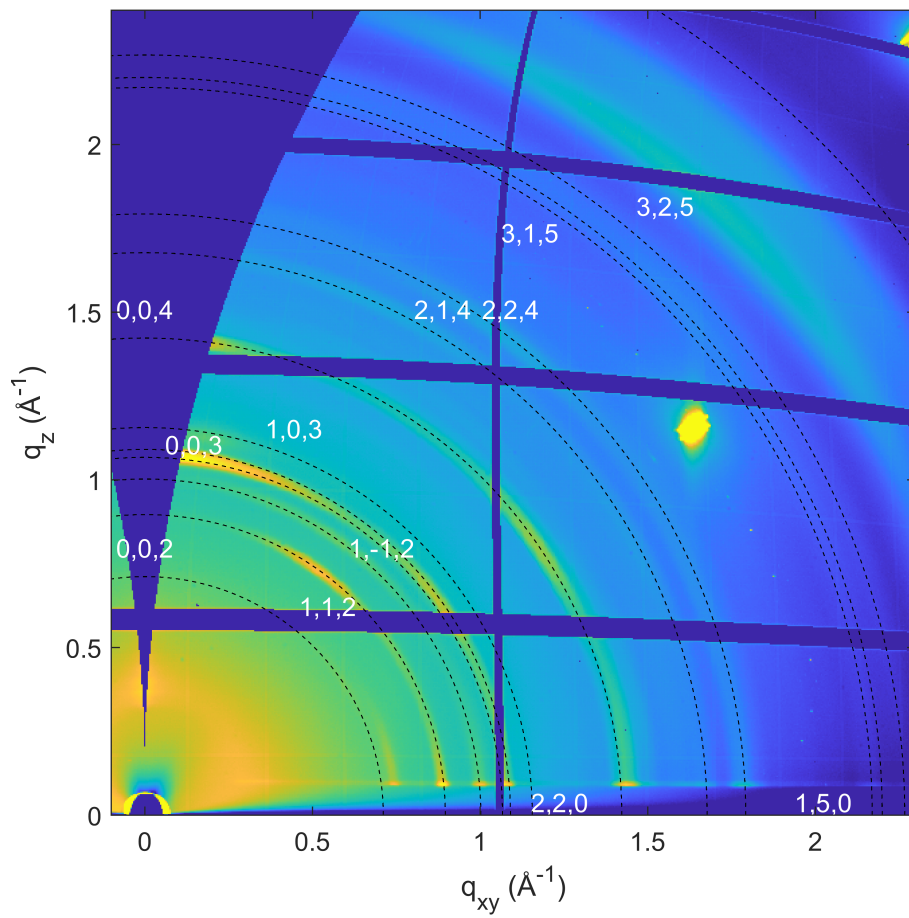
Figure 6.9: Indexed and logarithmically displayed GIXD pattern of sample fINA09 at incident angle $\omega = 1.0°$.
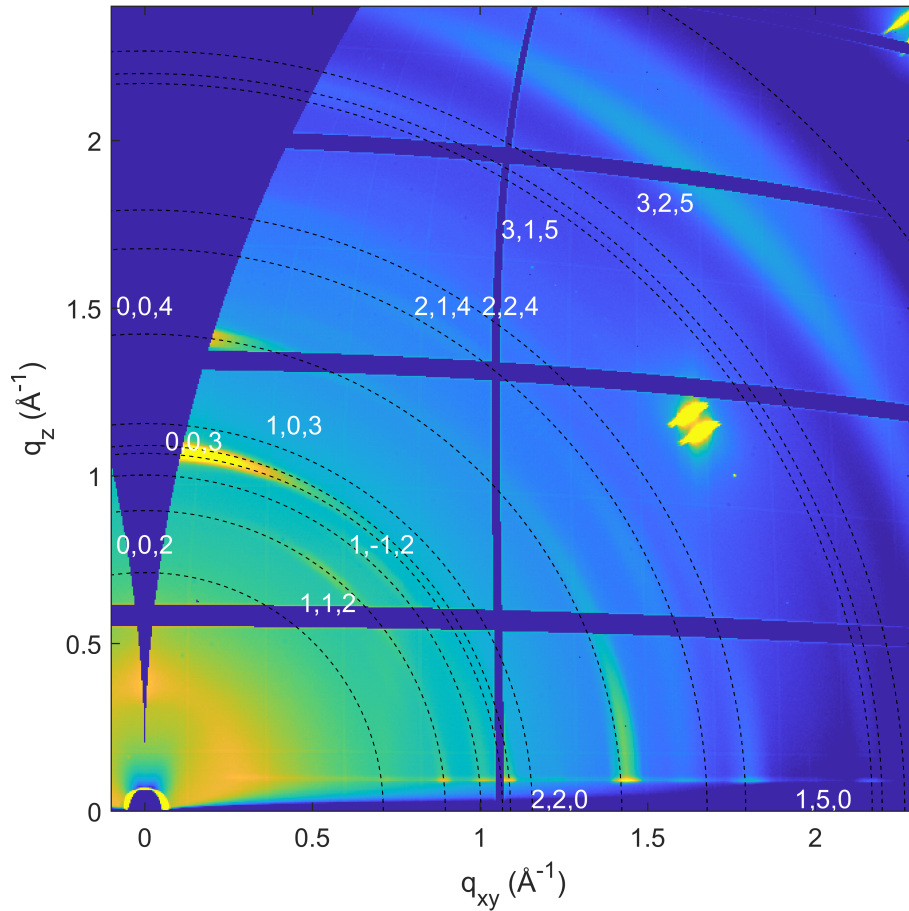
Figure 6.10: Indexed and logarithmically displayed GIXD pattern of sample fINA10 at incident angle $\omega = 1.0°$.

Sample 09 and 10 also appear to have a high degree of random alignment, derived from the diffraction rings featured in their respective GIXD scans. The theoretical structure is in far better agreement with the observed maxima of fINA09 and 10, compared to fINA08. The theoretical Debye-Scherrer rings seen in Fig. 6.9 coincide neatly with the observed diffraction rings. Differences to fINA10 are very small and the same rings can be seen in Fig. 6.10. The only noticeable difference is the lower intensity for some diffraction peaks of fINA10. The intensity of the precursor ring is naturally lower, since the CuO layer of sample 10 was only 10 nm compared to 20 nm, but the 112 and -112 MOF peaks and some segments of the ring corresponding to the 004 peak appear to lack the intensity seen in Fig. 6.9. One reason could be the self limiting conversion process, where a 10 nm precursor layer is not thick enough to reach the limit for MOF growth.
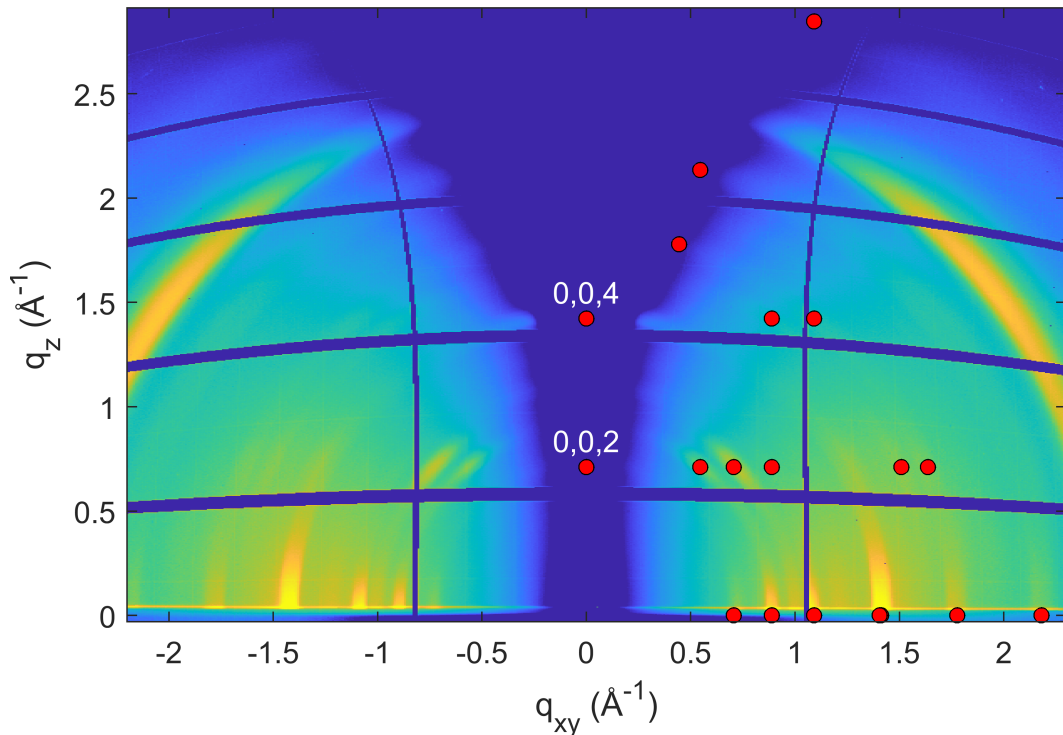
Figure 6.11: Indexed and logarithmically displayed GIXD pattern of sample fINA11 at incident angle $\omega = 0.2°$.

The measurement set-up at the XRD1 beamline allowed switching the pin hole attachment, a steel cylinder where the synchrotron radiation exits the beam guide to incide on the sample. Depending on the size and geometry of the sample, it was necessary to change the long model for a shorter pin hole cylinder, to allow the rotation of larger samples. The measurement series of fINA11 was performed with a short pinhole, increasing the effect of air scattering and adding a diffuse background to the measurements. For better visualisation of the GIXD pattern of fINA11 in Fig. 6.11, correction factors were applied. The software *GIDVis* provides several options for correction factors (see *GIDVis* Manual [38]) and the Lorentz velocity factor and the Polarization correction factor were applied to the intensity value map of fINA11.

The diffraction pattern was again in coherence with the unit cell solution from indexing. Despite the grazing incidence angle of 0.2°, the CuO precursor peak is very pronounced and intensive, hinting at a large amount of unconverted CuO. Almost no diffraction maxima, appear in the odd l rows, except for the ± 115 peak, only visible without correction factors.
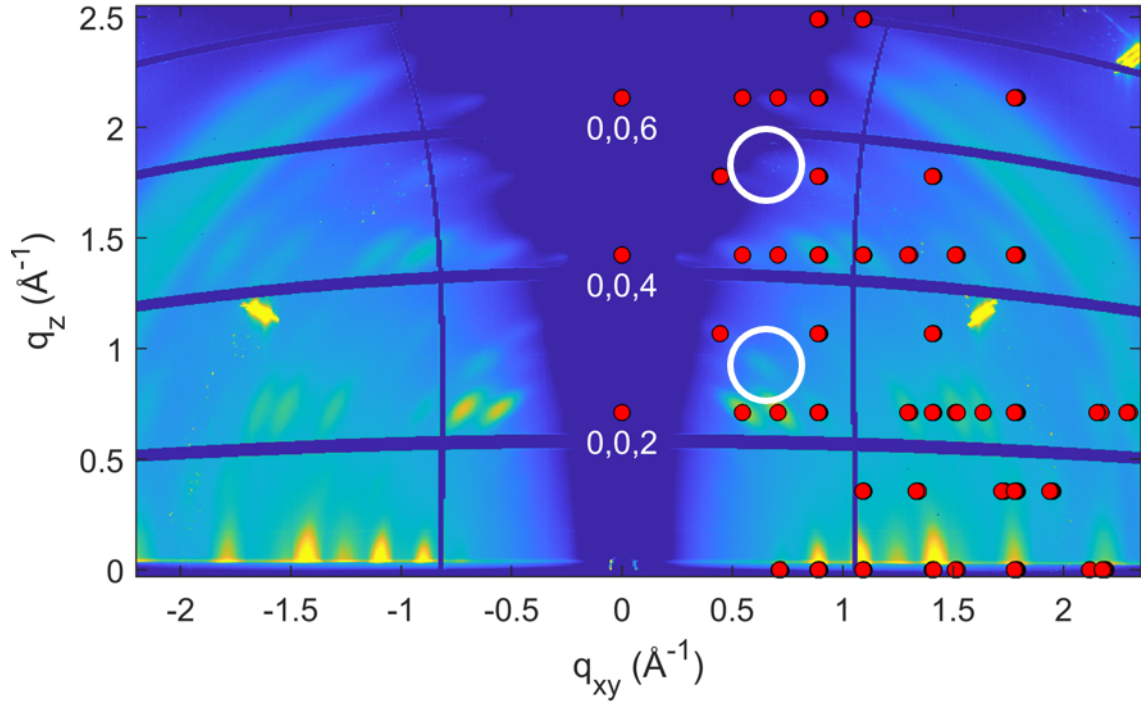
Figure 6.12: Logarithmically displayed and summed GIXD pattern of sample fINA12 at incident angle $\omega = 0.2°$, with theoretical diffraction peaks indicated and interstitial peaks highlighted.

As for to the diffraction pattern of fINA04 (Fig. 6.5), the pattern of fINA12 featured a large number of distinguishable peaks, with only minor azimuthal smearing. Astonishingly, the peaks in rows with odd l appear in the same commonness as in fINA04, where water was added during the synthesis. In addition to those peaks, two features not related to the theoretical peaks, can be seen in Fig. 6.12. The highlighted feature occurs between the $l = 2$ and $l = 3$ rows at $q_{xy} = 0.63 \, \text{Å}^{-1}$, $q_z = 0.94 \, \text{Å}^{-1}$ and is repeated at $q_z = 1.87 \, \text{Å}^{-1}$. The shape and azimuthal smearing of the interstitial maximum suggest that it belongs to the Cu-INA structure.

Looking at the following diffraction pattern of fINA13 in Fig. 6.13, the highlighted, interstitial feature appear again and two more can be seen, additionally. The cause of these peaks is still not understood. Whether the cause is from a distinct structure with a different unit cell or some other effect plays a role can not be said.

Besides the intensive in-plane peaks at $q_z = 0 \, \text{Å}^{-1}$, fINA13 features almost no diffraction peaks and is more akin to fINA11 in Fig. 6.11, than fINA12. The synthesis parameters of sample 11, 12 and 13 only differed in the precursor thickness, but sample 12 appears to have a much higher order and crystallinity.
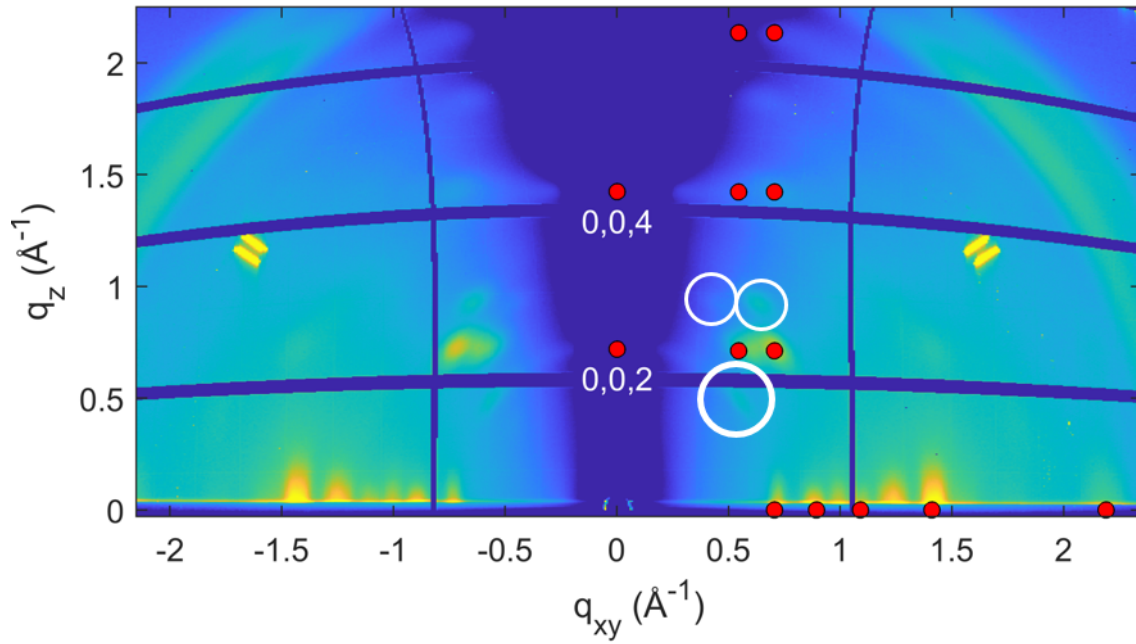
Figure 6.13: Logarithmically displayed and summed GIXD pattern of sample fINA13 at incident angle $\omega = 0.2°$, with theoretical diffraction peaks indicated and interstitial peaks highlighted.

Consequently, unknown factors, not documented by the researches during the preparation or synthesis, have to be regarded as a possibility for the divergent results.

As expected due to the specular scan, the GIXD pattern of fINA15 features the smeared out 003 peak at $q = 1.06\,\text{Å}^{-1}$. Otherwise the diffraction pattern in Fig. 6.14 fits well to the theoretical diffraction peaks. The 001 peak would be expected in a region close to the area covered by the primary-beam stopper. It is hard to tell, if the accumulation of intensity at $q_z = 0.36\,\text{Å}^{-1}$ could be attributed to a smeared specular 001 diffraction peak or only to the commonly occurring halo of the beam stopper, especially since the specular scan did not hint at its presents.

Sample 16 in Fig. 6.15 and 17 in Fig. 6.16 differ from 15, since their GIXD patterns do not show the smeared 003 specular peak and the intensity distributions look like they are quite the opposite, with respect to the l rows. While fINA15 has the dominating feature at $l = 3$ and the in-plane peak intensities extend far into the $l = 1$ row, fINA16 and 17 solely have peaks in even l rows, with the exception of the faint ± 105 peak for fINA16. Sample 16 also features far more diffraction peaks, indicating a higher crystallinity. This sample trio, with varied precursor thicknesses, appear to follow the same trend seen in the sample group of fINA11
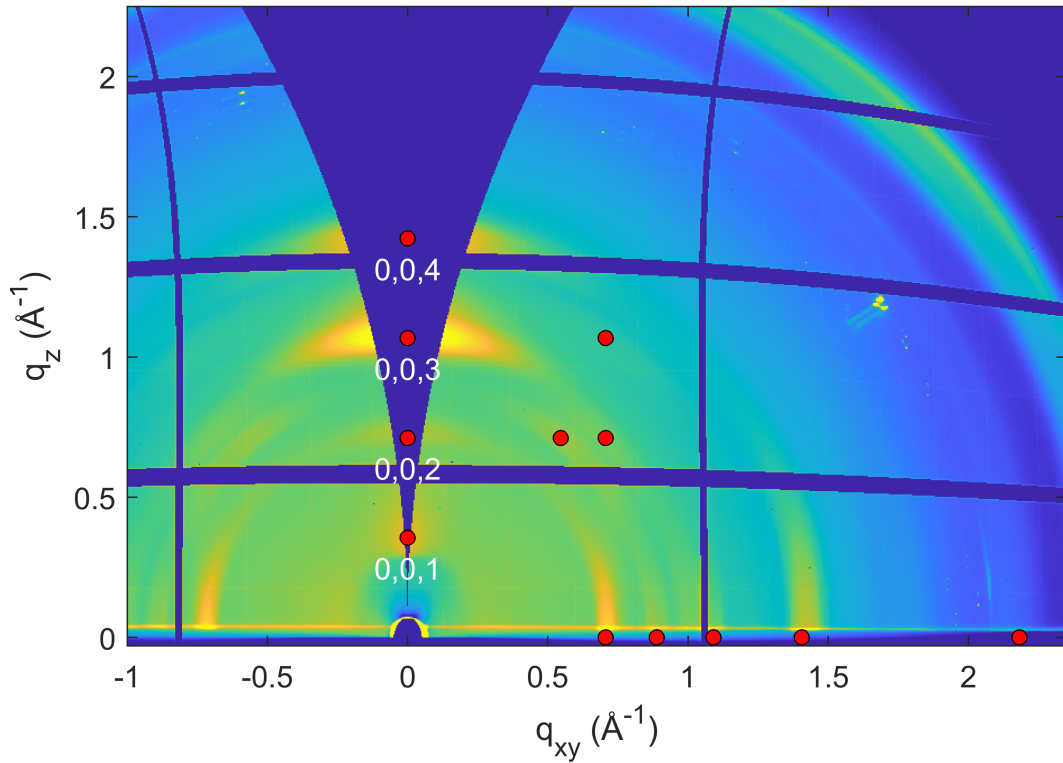
Figure 6.14: Logarithmically displayed and summed GIXD pattern of sample fINA15 at incident angle $\omega = 0.2°$, with theoretical diffraction peaks indicated.

to fINA13, where only fINA12 with a precursor thickness of 20 nm featured a high number of distinguishable and ordered diffraction maxima.

An additional diffraction peak, not related to the determined unit cell, can be seen for fINA04 to 06, 11 to 13, 16 and 17, as well as fINA07, 14 and 18 with nanobelt precursor layers. The in-plane diffraction peak at $q_{xy} = 1.22\,\text{Å}^{-1}$ can not be explained by any of the theoretical peaks, with the crystal in (001) orientation. Its scattering vector length q somehow coincides with the outer diffraction ring seen in the GIXD patterns of fINA01 to 03 (Fig. 6.1, 6.2, 6.3). In all the presented measurements, this in-plane peak is only absent in GIXD patterns, where the 003 diffraction peak at $q_z = 1.06\,\text{Å}^{-1}$ is featured (see Fig.6.8, 6.9, 6.10, 6.14). The cause of this phenomenon is still unexplained.

With one exception (fINA02) the grazing-incidence diffraction patterns of the fINA samples are in accordance with diffraction patterns from the specular scans. Additionally, a unit cell determined by diffraction peak positions of sample 04 through indexing, is in agreement with the diffraction pattern of all samples, bar fINA01 to 03 and fINA08 to some degree. Diffraction peaks in rows with an odd

index l were only consistently exhibited in fINA04, 05 and 06 and fINA12.
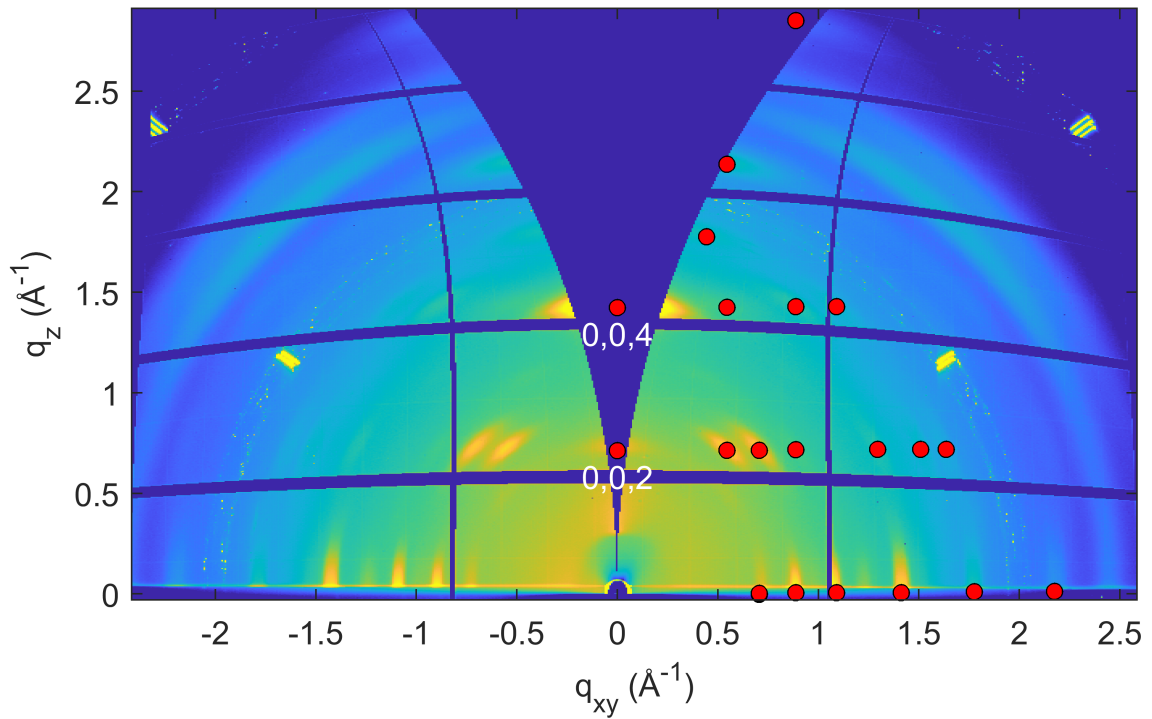
Figure 6.15: Logarithmically displayed and summed GIXD pattern of sample fINA16 at incident angle $\omega = 0.2°$, with theoretical diffraction peaks indicated.
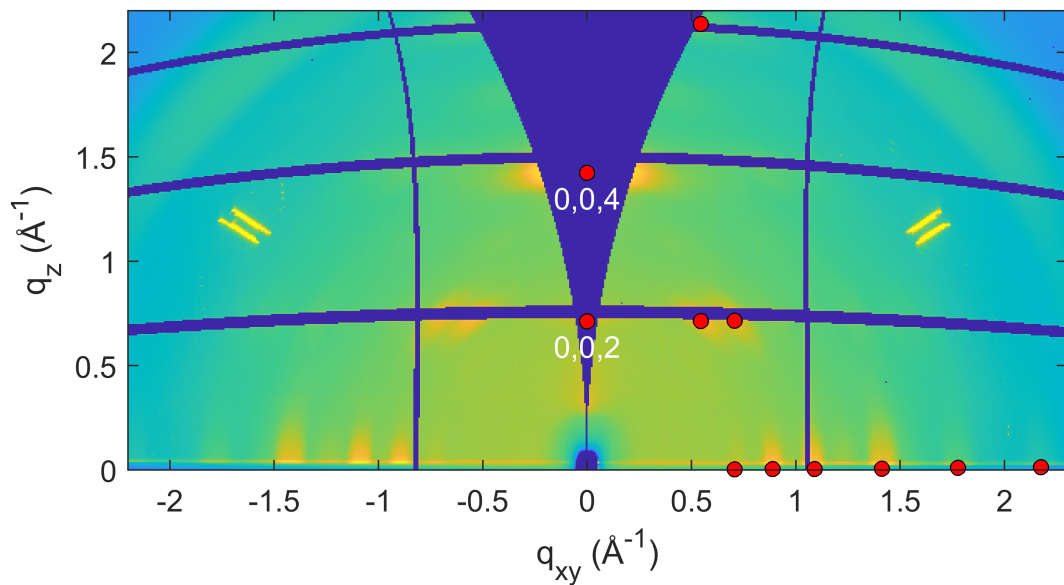
Figure 6.16: Logarithmically displayed and summed GIXD pattern of sample fINA17 at incident angle $\omega = 0.2°$, with theoretical diffraction peaks indicated.

6.2 Grazing Incidence X-ray Diffraction Pattern of Cu(OH)$_2$ samples

Copper hydroxide nanobelt samples exhibited *axial* orientation, therefore more thorough rotating GIXD measurement were performed by recording 180 GIXD patterns while integrating over 2° of rotation, respectively.
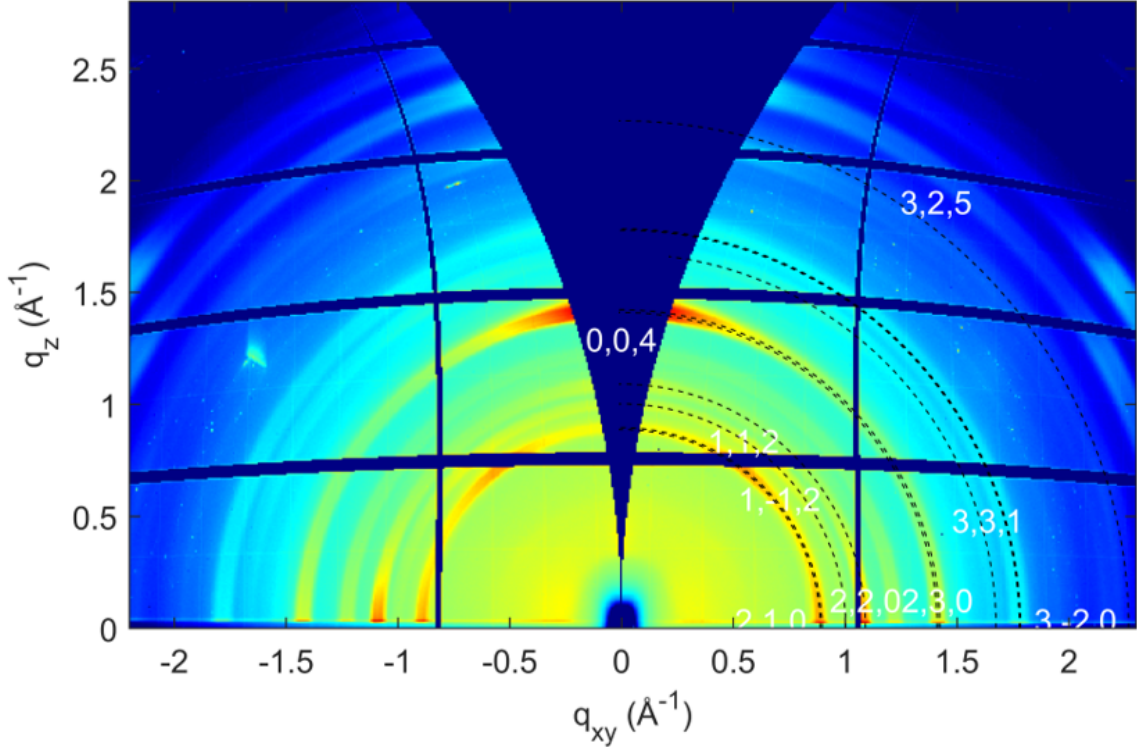
Figure 6.17: Logarithmically displayed, indexed and summed GIXD pattern of sample fINA07 at incident angle $\omega = 0.2°$, with theoretical diffraction peaks indicated.

A summed up rotational measurement of fINA07 is presented in Fig. 6.17. The 180 GIXD patterns featured diffraction rings, where some segments had higher intensities. These high intensity segments changed their locations along the ring, over the course of the 360° rotation. In the presented summation, the most common spots for intensity accumulations along the rings stand out. Incidentally, these are the positions where the 112 and -112 peaks would for example be found. The diffraction pattern is clearly related to the determined unit cell and the previously discussed samples with CuO precursor films. The in-plane peak at $q = 1.22 \,\text{Å}^{-1}$ is also featured in the diffraction pattern of fINA07, 14 and 18 (Fig. 6.17, 6.19 and 6.21).
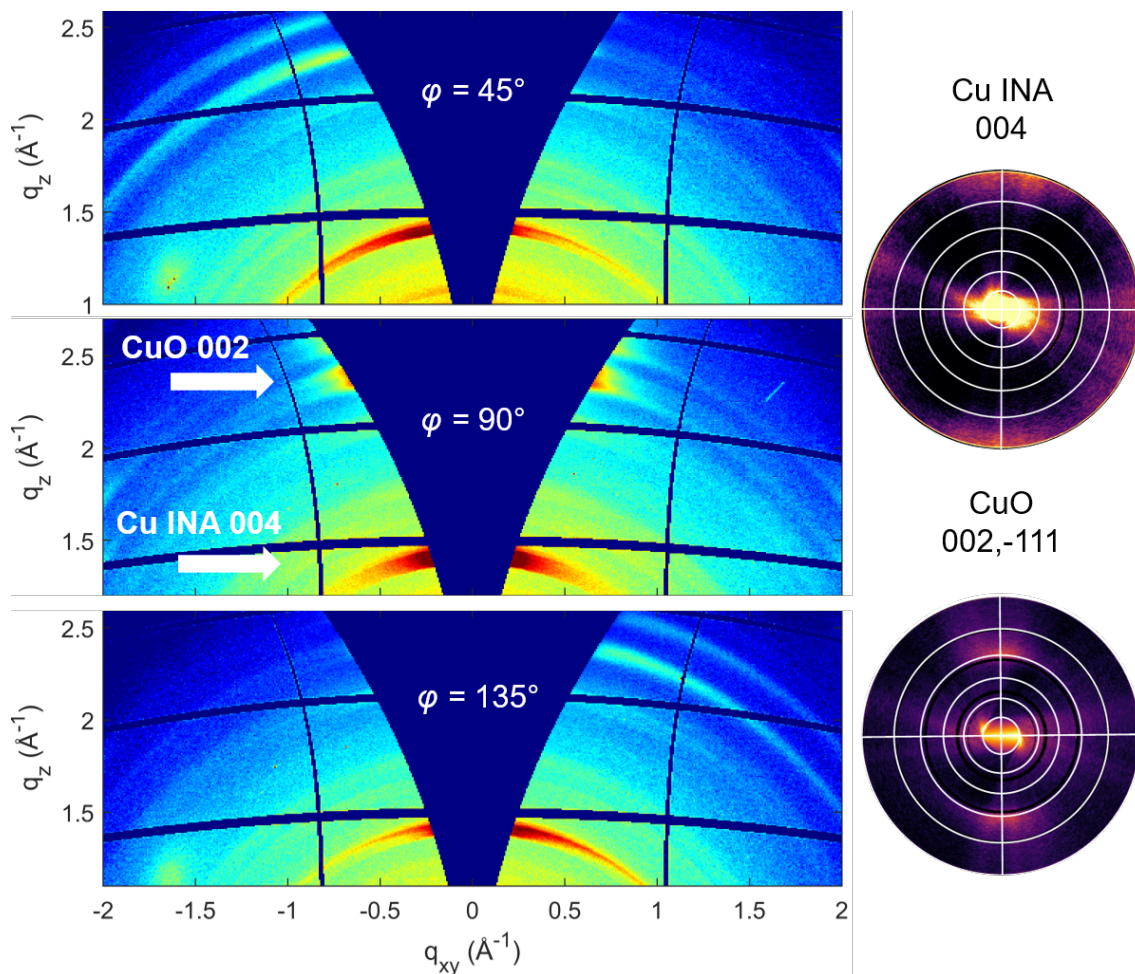
Figure 6.18: GIXD patterns of sample fINA07 at rot. angles $\phi = 45°, 90°, 135°$ (left), with the CuO 002 and Cu-INA 004 peaks highlighted. Pole figures correspond to the Cu-INA 004 (top right) and the CuO 002, -111 peaks (bottom right).

For better visualisation of the epitaxial relationship between the residual CuO and the synthesized metal-organic framework, a series of GIXD scans of fINA07 at different rotation angles are shown in Fig. 6.18. Starting at a relative rotational angle of 45°, the CuO 002 peak appears to be accumulated on the left side of the inaccessible wedge, while the intensity of the Cu-INA 004 also tends to lean more on the left. Rotating an additional 45° shows both diffraction peaks being symmetrically distributed and smeared across the wedge. Going 45° further to a relative rotational angle of 135° and both peaks are now seen on the right side of the wedge.

The summed diffraction pattern of fINA14 also solely features diffraction rings and compared to fINA07, the intensities of the rings appears to be more uniformly distributed. The same is true for the summed GIXD pattern of fINA18 in Fig. 6.21,
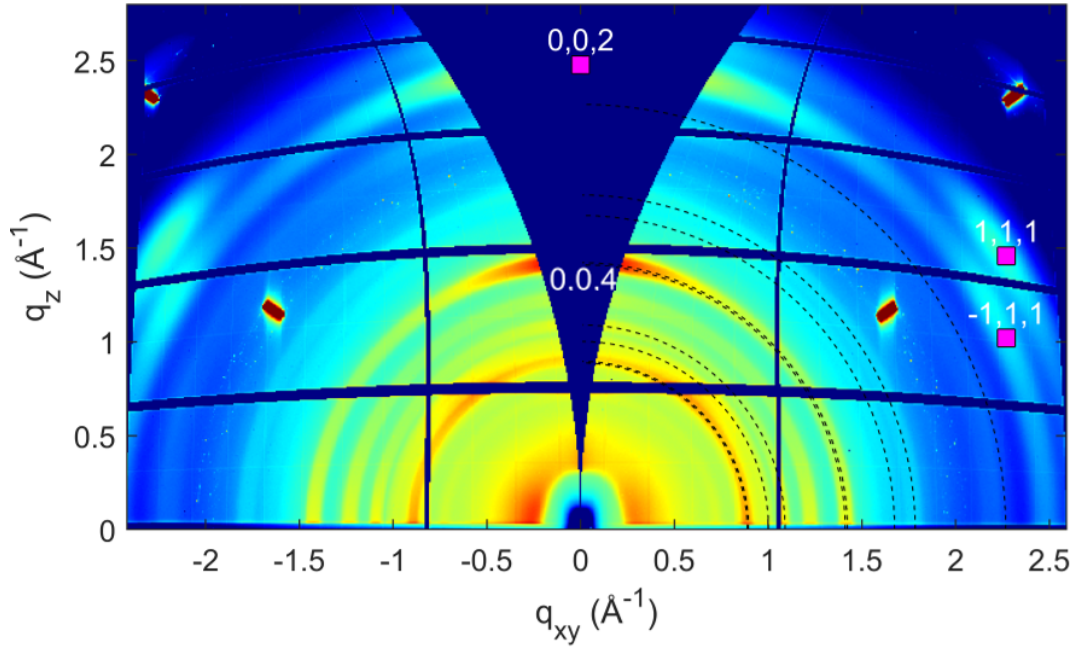
Figure 6.19: Indexed, logarithmically displayed and summed GIXD pattern of sample fINA14 at incident angle $\omega = 0.2°$.

where the theoretical diffraction peaks corresponding to the observed rings are highlighted as well. Included are the theoretical positions of the CuO 002, 111 and -111 peaks with the (001) plane parallel to the substrate. The indicated CuO peaks are traversing across the GIXD map along their q value during rotation, due to the preferred *axial* orientation inherited by the parent substance $Cu(OH)_2$.

In Fig. 6.20 the epitaxial relationship is examplified for fINA14. Again, the GIXD patterns presented at three consecutive rotational angles with a stepsize of 45° are shown and the same observation as for fINA07 can be made.

The pole figures depicted on the right of Fig. 6.18, 6.20 and 6.22 display the stereographic projections representing the spatial distributions of crystal lattice plane orientations. The pole figures were generated in the software *GIDVis*, using the 180 rotated GIXD measurements. For the Cu-INA 004 pole figure, the area along $q = 1.42 \, Å^{-1}$ was selected and for the CuO 002, -111 pole figure, the area along $q = 2.49 \, Å^{-1}$ was selected.

This depiction is quite useful in showing the rotational dependence of the peak intensity of Cu-INA 004 and how the intensity distribution coincides with the intensity distribution of the CuO peaks. The pole figures of the GIXD patterns of fINA18 in Fig. 6.22 illustrates the epitaxial relation between the framework and the residual precursor even better.
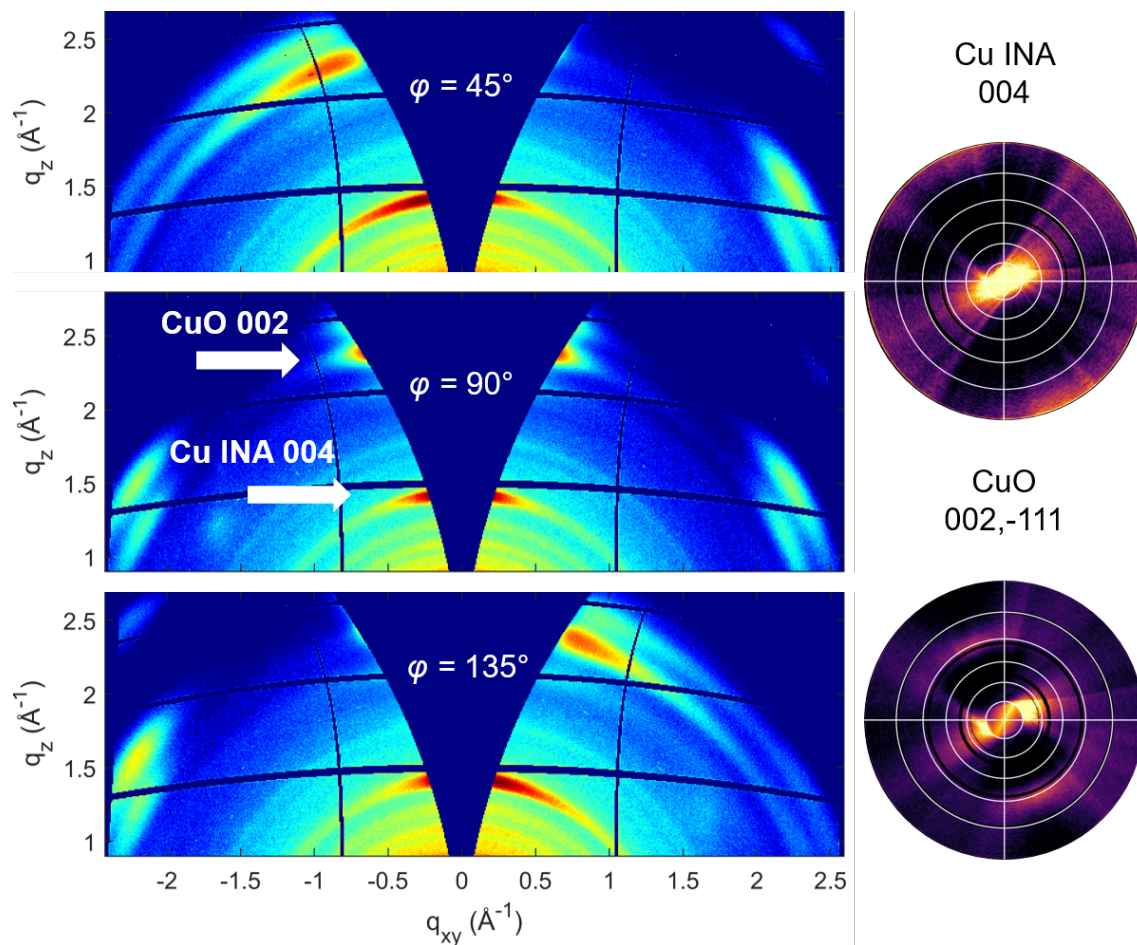
Figure 6.20: GIXD patterns of sample fINA14 at rot. angles $\phi = 45°, 90°, 135°$ (left) and the related CuO 002 and Cu-INA 004 peaks highlighted. Pole figures correspond to the Cu-INA 004 (top right) and the CuO 002, -111 peaks (bottom right).

The indices of the theoretical diffraction peaks, that fit to the GIXD patterns of the nanobelt samples, can be seen in Fig. 6.21 plotted over the diffraction pattern of fINA18. The theoretical peak positions match the observed ring positions well.

Grazing incidence diffraction patterns of the three samples synthesized from $Cu(OH)_2$ nanobelt precursor layers feature more or less the same diffraction maxima. Compared to the CuO precursor samples, the synthesized metal-organic framework exhibited no *uniplanar* preferred orientation, but the same *axial* preferred orientation as the nanobelt precursor layer itself. This was expressed by the observed diffraction rings, which had shifting intensity distributions, dependent on the rotational angle ϕ during the rotated GIXD experiment. The observed maxima positions match the theoretical unit cell obtained by indexing fINA04. Furthermore,
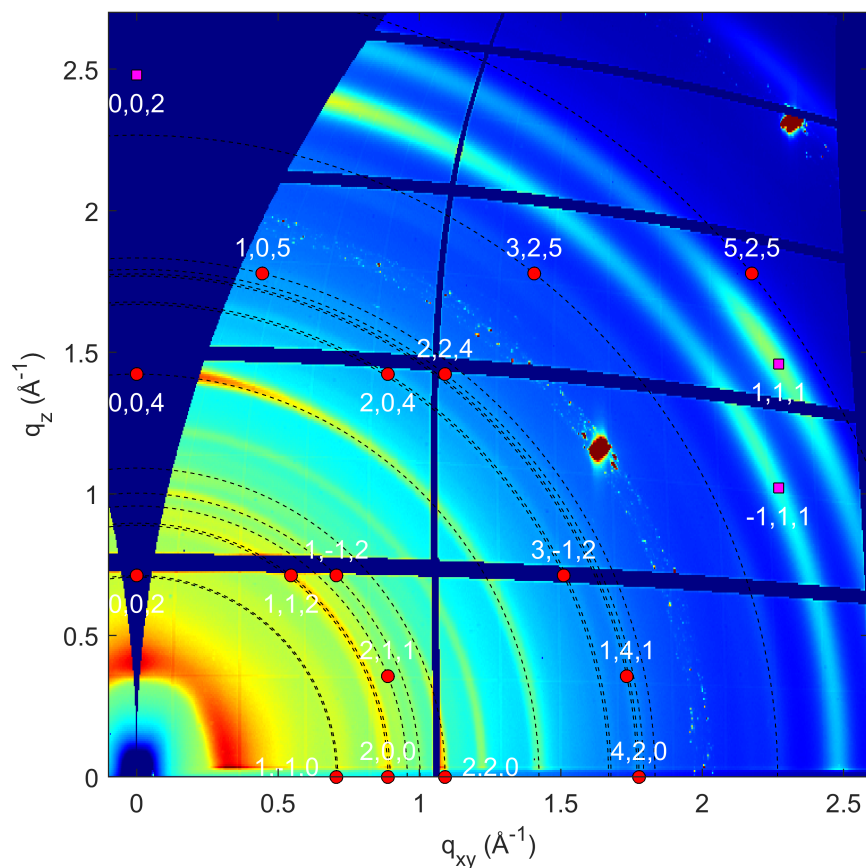
Figure 6.21: Linear and summed GIXD pattern of sample fINA18 at incident angle $\omega = 0.2°$. CuO peaks (magenta squares) and theor. diffraction peaks (red circles) and rings are indicated.

the residual precursor diffraction peaks belong rather to CuO with preferred *axial* orientation, than to $Cu(OH)_2$. This is suggesting a decomposition process, where the orientation seems to be conserved, occurring at some stage of the preparation.
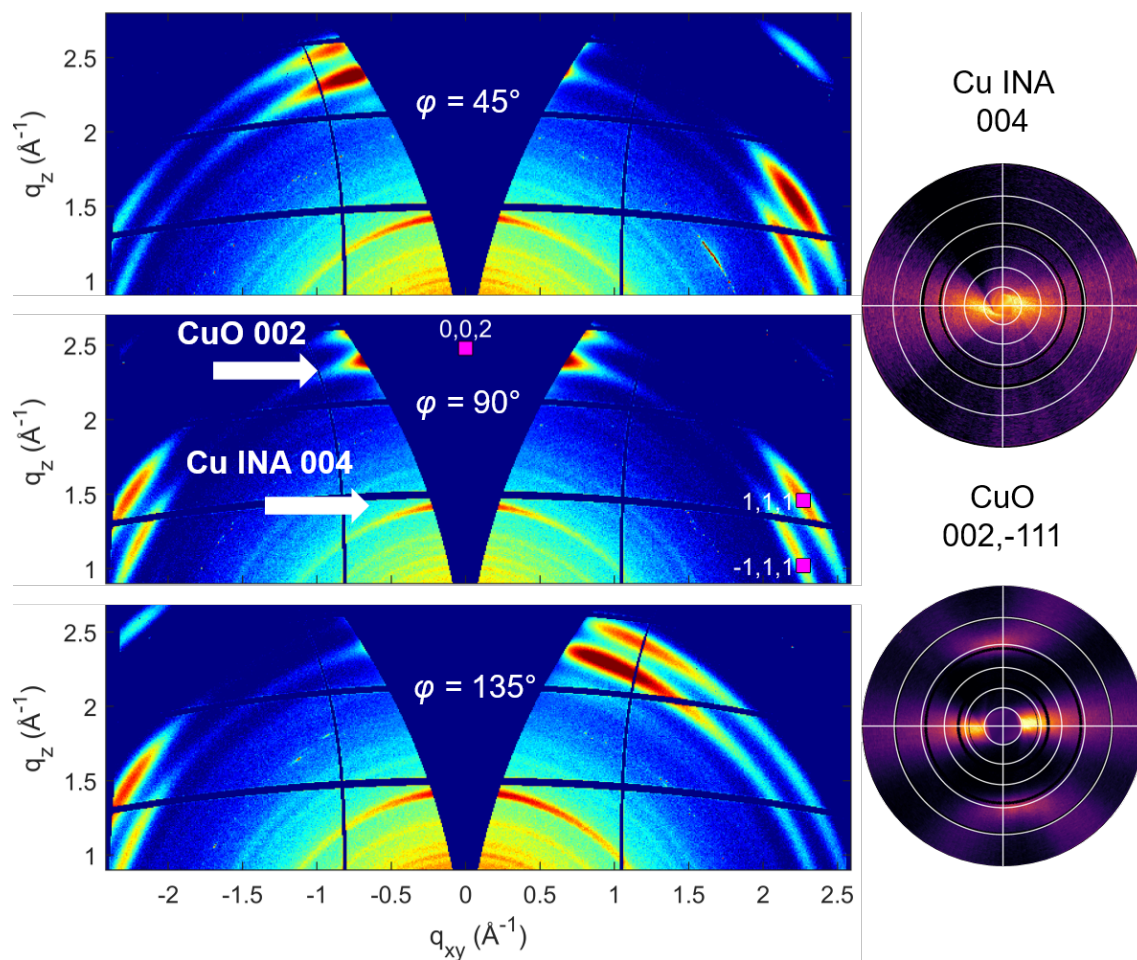
Figure 6.22: GIXD patterns of sample fINA18 at rot. angles $\phi = 45°, 90°, 135°$ (left). CuO 002, 111, -111 diffraction peaks are indicated (magenta squares) and the related CuO and Cu-INA peaks highlighted. Pole figures correspond to the Cu-INA 004 (top right) and the CuO 002, -111 peaks (bottom right).

Chapter 7

Heavy-Atom Method I: Testing the routine

The observed diffraction patterns of the fINA samples have been compared with theoretical diffraction patterns of several suitable structures like *UFUMUD* and other Cu-INA frameworks registered on the Cambridge Crystallographic Data Center. The database was also searched for structures with unit cell parameters coinciding with the parameters determined by indexing. Neither search produced a matching structure, therefore the crystal structure would have to be solved to derive the topography of the framework and atomic content in a unit cell.

Organic crystals usually follow the principle of closest packing [39] during their formation. After diffraction patterns have been indexed to determine a unit cell, preliminary assessments of molecular positions and orientations in the unit cell can be made, based on the lengths of the molecule. Further refinements for the orientations and positions of molecules and atoms can then be made with molecular dynamic simulations or density functional theory calculations.

Closest packing is contrary to the definition of a metal-organic framework and MOF unit cell sizes are generally much larger than the involved organic linker molecules and metallic ions or clusters. Deducing molecular positions inside the unit cell, based on coinciding lengths, is therefore not feasible.

Nowadays, the conventional method for crystal structure solutions is *Direct Methods*, e.g. implemented in *SHELX* [40]. With Direct Methods atomic positions inside a unit cell are determined via varied test structures and the statistical correlations between their structure factors and observed diffraction intensities. The experimental input for a Direct Methods solution usually comes in the form

of single-crystal diffraction data, consisting of a very large number of diffraction maxima. The investigated samples at hand were thin films with solely uniplanar oriented crystallites and for the samples with the most diffraction peaks, fINA04 and 12, only around 40 peaks were recorded. Direct Methods are not suitable for solving the fINA crystal structure.

Copper is relatively heavy, compared to the elements occurring in the organic linker INA, which is why the *Heavy Atom Method* based on the Patterson function was considered as a possible approach for gaining insight into the atomic makeup of this Cu-INA framework. The porosity of the framework and the disparity in electron density between organic linker and copper atoms should provide circumstances, where the method might be applicable. Patterson function based solution algorithms were usually applied to single-crystal or powder diffraction data and in the current versions of the Direct Methods software SHELX, the determination of Patterson vectors plays an integral role in solving structures containing heavy atoms from single-crystal data.

7.1 Heavy-Atom Method Routine

Existing software packages for the calculation of Patterson function values or Patterson maps were deemed not suitable or too antiquated for the needs at hand. The lack of options can be correlated with the decline in use of this method. For that reason, a custom Patterson function calculation routine was constructed. The routine is based on the previously discussed chapter from D. W. Bennett [25], namely the practical form of the Patterson function in Eq. 7.1 and was implemented in *Matlab*. It can be roughly separated into three parts. Calculating a Patterson map $P(u, v, w)$, determining the maxima and the corresponding Patterson vectors and the processing of said vectors and their subsequent utilization to determine positions of heavy atoms inside the unit cell.

$$P(u, v, w) = \frac{1}{V_c} \sum_{hkl} I(hkl) \, \cos[2\pi(h\,u + k\,v + l\,w)], \qquad (7.1)$$

7.1.1 Calculating a 3D Patterson map

The evaluation of the Patterson function in the form of Eq. 7.1 was set up to require the following additional input values, explained in the following section:

- Unit cell parameters a, b, c, α, β and γ,

- Intensity values I of diffraction maxima,

- Laue indices *hkl* of diffraction maxima,

- Resolution parameter *res* in Å,

- Fractional coordinate limits *fracmin* and *fracmax* for the unit cell dimensions.

The arguments of a Patterson function $P(u,v,w)$, at which the function is evaluated, are the fractional coordinates $u, v, w \, \epsilon \, [0,1]$ of the crystallographic unit cell. In *Matlab* the function can be evaluated at all coordinate positions at once, creating a 3D function map, with discrete, predetermined values for (u,v,w). The step sizes $\Delta u, \Delta v, \Delta w$ between two coordinate values depend on the resolution parameter *res* and are defined as

$$\Delta u = \frac{res}{a}, \; \Delta v = \frac{res}{b}, \; \Delta w = \frac{res}{c}, \tag{7.2}$$

resulting in equal spacing for the coordinates, when converted into real space distance in Å. Values for the resolution have a large impact on the calculation time, since e.g. changing the value from the default 0.1 Å to 0.05 Å leads to 2^3 more entries in the Patterson map.

The limits *fracmin* and *fracmax* determine the range of fractional space coordinates used for calculating the Patterson function, hence the size of the Patterson map. For limits exceeding the default values of $[0,1]$, interatomic vectors extending into adjacent unit cells are depicted more comprehensible. Due to the centrosymmetric and periodic nature of the function, going beyond one unit cell is usually not necessary. On the other hand, limiting the fractional coordinates below the full size of one unit cell has the practical advantage of enabling the use of smaller resolution parameters for a more exact examination of regions of interest, while avoiding a memory overflow.

Laue indices are multiplied with every coordinate of the Patterson map simultaneously, meaning every combination of the coordinates u, v and w is preallocated in an array and separated into three vectors $\boldsymbol{U}$, $\boldsymbol{V}$ and $\boldsymbol{W}$, which are then multiplied by h, k and l respectively. The phase factor of the Patterson function is the cosine of the sum of those vectors. A simple *for*-loop, over the number of diffraction peaks, calculates the Patterson map for one set of intensity I and *hkl* and adds those maps together. Calculating a Patterson map however is straight forward and was achieved by following the mathematical formulations from D. W. Bennett [25].

Determining Patterson vectors, in the form of local maxima, on the other hand, required an inconvenient and cumbersome approach.

7.1.2 Detecting Patterson Vectors

A global maximum, as a function value at a single coordinate (u_i, v_i, w_i) of the 3D Patterson map, is determined. Peaks in the Patterson function can be considered Gaussian, where the determined maximum would be the apex. The whole Patterson map is then translated to place the apex in the center position at $u = v = w = 0.5$. Due to periodic boundary conditions, maxima have to be placed in the center, to avoid detecting the same peak multiple times. Saving the information of peak intensity P_i^{max} and the position (u_i, v_i, w_i) of the detected peak i, is followed by determining the distance from the apex to the closest minima in all three dimension. Calculating an ellipsoid, with semi-axes corresponding to distances to the minima, allowed the approximation of the shape and spatial expansion of the Patterson peak. Now, all function values of the Patterson map inside the ellipsoid are set to $-P_i^{max}$ and the whole map is translated to its original state. This operation is continued in a *while*-loop until the global maximum is either smaller or equal to zero or no neighbouring minimum in any direction for a peak can be found. With several other methods for peak detection tested, this approach was deemed the most reliable at detecting the maxima of higher intensities, associated with heavy atom pair peaks. The drawbacks are artifacts emerging at edges of the cut-out ellipsoids, which are registered further down the list during the *while*-loop.

7.1.3 Processing Patterson Vectors

The list of Patterson peaks is ordered by descending intensity. For an easier evaluation, Patterson vectors in fractional coordinates can be converted to real space coordinates. First a matrix has to be constructed from the unit cell parameters as

$$\boldsymbol{A} = \begin{pmatrix} a & b \, \cos \gamma & c \, \cos \beta \\ 0 & b \, \sin \gamma & -c \, \sin \beta \, \cos \alpha^* \\ 0 & 0 & c \, \sin \beta \, \sin \alpha^* \end{pmatrix} \tag{7.3}$$

$$\cos \alpha^* = \frac{(\cos \beta \, \cos \gamma - \cos \alpha)}{\sin \beta \, \sin \gamma}, \ \sin \alpha^* = \frac{V}{a \, b \, c \, \sin \beta \, \sin \gamma}$$

and the unit cell volume V. The matrix product between unit cell matrix $\boldsymbol{A}$ and Patterson vectors in fractional space, produces real space distance vectors in Å.

Deciphering the atom pair type causing a Patterson peak is accomplished by comparing the peak intensities. Peaks with high intensities can generally be assigned to heavy atom pairs (H–H) while, depending on the investigated structure, light atom pair peaks (L–L) are drowned by noise or larger, superimposing peaks. A selected number of H–H vectors can subsequently be used for the construction of a model structure of heavy atoms. With the current routine, this is either accomplished by looking at *Harker* symmetries, requiring knowledge of the space group, or by vector *superposition.*

The conventional method for a superposition would be to sum a Patterson map with a second map, that was translated by a selected Patterson vector. For the resulting superimposed map, maxima would be determined, saved and the process repeated for several more vectors from the list. Similar results were achieved at a lower computational effort by simply adding vector pairs from the list of selected H–H peaks, instead of entire Patterson maps. If the sum of two vectors is equal or almost equal to a third vector, three atoms can be connected and their relative positions be determined.

If the limits of the unit cell are chosen as [0,1], maxima can only be detected at positive coordinates. Some Patterson vector sums are therefore leaving the unit cell boundary and entering an adjacent cell from the opposite side, making the process of finding a matching third vector tedious, since all distance vectors are mapped into the same unit cell. This can be circumvented by extending the unit cell limits to e.g. [-1,1] or [-0.5,0.5], albeit no additional information is gained, as can be seen in Fig. 7.1 b.), where four adjacent 2D unit cells are depicted. For this hypothetical structure of two C_6H_5I molecules in a unit cell in Fig. 7.1a.), several distance vectors between the same two iodine atoms can be defined. The displayed vectors both have solely positive components and both can be found as high intensity H–H peaks in the Patterson map to the right. The direct vector between the iodine pair, not crossing unit cell boundaries, can only be found, when extending into negative unit cells in Patterson space. This example also highlights why the Patterson function is centrosymmetric and why one atom pair results in several distance vectors. Vector sums need to conform to the periodic boundary conditions and in practice this was implemented via a modulo division to the fractional limits of the unit cell and the sum of two vectors has to full fill

$$\vec{v_3} = \mathrm{mod}(\vec{v_2} + \vec{v_1}, 1) \tag{7.4}$$

to project onto a third Patterson vector.
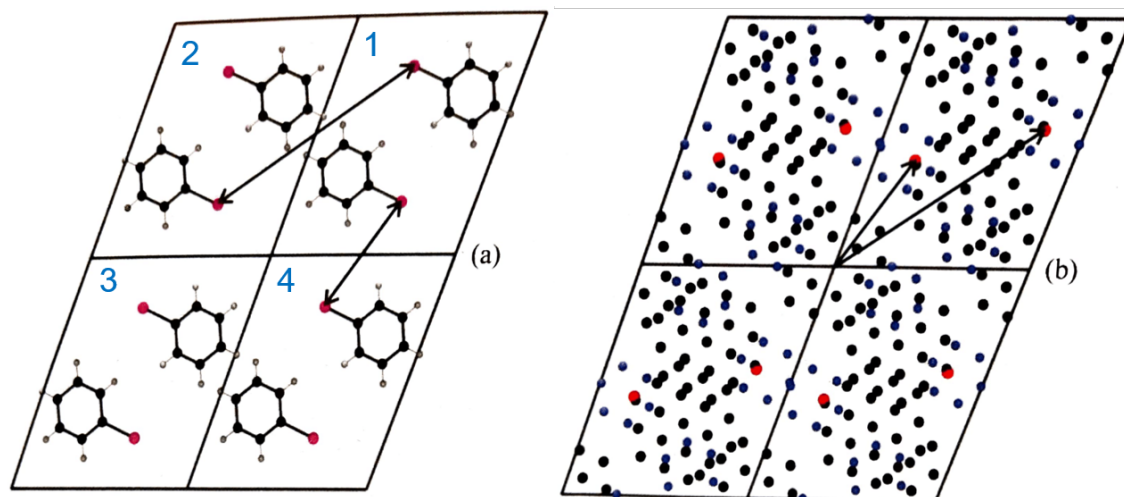
Figure 7.1: a.) Four unit cells containing two C_6H_5I molecules each. Distance vectors between the iodine atoms are indicated. b.) Illustration of the Patterson maxima associated to the structure on the left. The same distance vectors are marked. Printed from [25].

Before using the routine on diffraction data from fINA04, it was tested by determining the heavy atom positions of known structures. With the software *Mercury*, theoretical powder diffraction patterns of reported structures can be calculated. Powder patterns contain squared structure factors, proportional to the intensity, and Laue indices of diffraction peaks. Previously presented Patterson maps, e.g. of Copper(II) phthalocyanine (CuPc) in Fig. 3.4, were calculated using the *Matlab* routine. Additionally, the positions of iron atoms in the organometallic compound Ferrocene were determined with H–H vector superposition and by looking at *Harker* symmetries as well.

7.2 Testcase Ferrocene

Ferrocene has an organometallic complex of two cyclopentadienyl rings bonding to an iron atom from opposite sides. Investigated here, was the originally deposited crystal structure solution of 1'-Acetyl-1-benzoyl-ferrocene (Fig. 7.2), with the space group $P2_1/c$. Four iron atoms can be found in the unit cell. The lengths of the distance vectors between the iron atoms can also be seen in Fig. 7.2. A powder
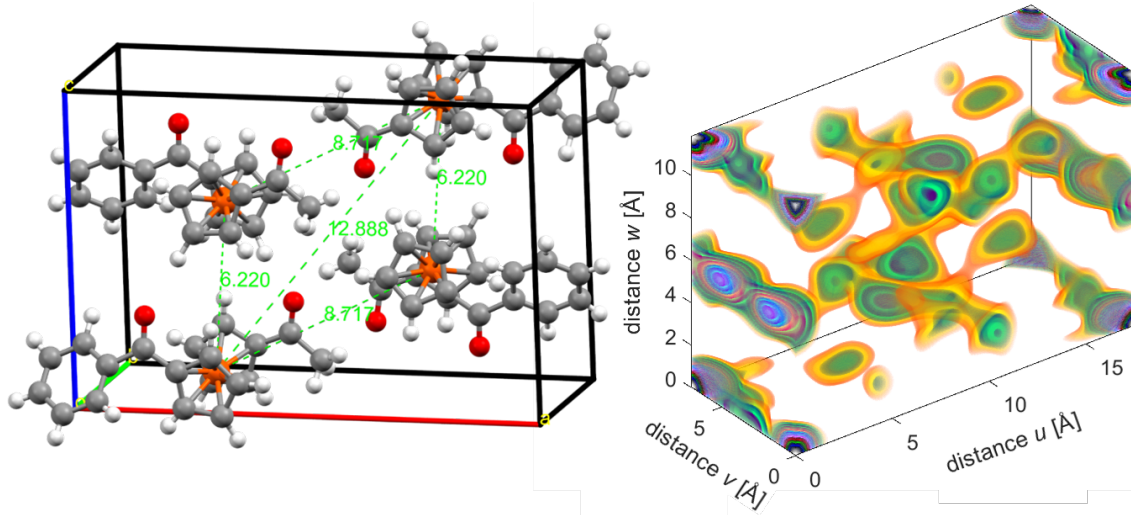
Figure 7.2: Crystal structure of 1'-Acetyl-1-benzoyl-ferrocene (*ABFERC10*) with indicated interatomic distances of iron (left). 3D Patterson map of ferrocene converted to real space coordinates (right).

pattern created from the structure file was used as an input for the Patterson function routine. The unit cell limits were set to $u, v, w \, \epsilon \, [0,1]$ and the resolution chosen as 0.025 Å, resulting in an array for the Patterson map with $(704 \times 282 \times 476)$ function values. The map is visualised on the right in Fig. 7.2 and already converted to real space distances in Å. The dominating peaks are the origin peak (dark violet), seen on all eight corners, and the two features related via centrosymmetry at $u = 0, 1$ and various peaks in the center (green to violet).

From the 101 Patterson peaks detected by the routine, the majority were disregarded on the basis of their low intensities. For this analysis, only interatomic vectors between heavy Fe atoms were of interest. The relevant detected Patterson vectors can be seen in Tab. 7.1 and have been manually selected from a list. Discriminable artifacts, whose peak width was by far too small to be considered as a physical relevant maximum, were removed. Fractional coordinate vectors were converted to real space vectors in Å to calculate the real space length of the vectors.

Table 7.1: List of selected Patterson vectors of ferrocene.

I...Peak intensity of Patterson maxima in arbitrary units.

u...Distance vector component in x as a fraction of a.

v...Distance vector component in y as a fraction of b.

w...Distance vector component in z as a fraction of c.

L...Length of the distance vector in Å.

	I [a.u.]	u	v	w	L [Å]
0.	405	0	0	0	0
1a.	211	0	0.27	0.50	6.20
1b.	211	0	0.74	0.50	7.87
2a.	112	0.59	0.51	0.73	13.95
2b.	112	0.42	0.49	0.27	8.68
3a.	95	0.41	0.23	0.77	11.74
3b.	95	0.59	0.77	0.24	12.07

7.2.1 Vector superposition

Patterson vectors are written with angled brackets as "$\langle$u,v,w$\rangle$" and are distance vectors between atoms, while atomic coordinates are denoted by round brackets as "(x,y,z)".

As the first vector, $\boldsymbol{v}_{1a} = \langle 0,0.27,0.50 \rangle$ from Tab. 7.1 is chosen. Generally, starting with the shorter of two centrosymmetry-related vectors is preferable for the superposition. The next pair of distance vectors is added to $\boldsymbol{v}_{1a}$:

$$\text{I: } \vec{v}_{1a} + \vec{v}_{2a} = \langle 0, 0.27, 0.50 \rangle + \langle 0.59, 0.51, 0.73 \rangle = \langle 0.59, 0.78, 0.23 \rangle$$
$$\text{II: } \vec{v}_{1a} + \vec{v}_{2b} = \langle 0, 0.27, 0.50 \rangle + \langle 0.42, 0.49, 0.27 \rangle = \langle 0.42, 0.76, 0.77 \rangle$$

At first glance, neither sum I or II appear to be equivalent to the vectors $\boldsymbol{v}_{3a}$ or $\boldsymbol{v}_{3b}$ in the list above. Analogous to Fig. 7.1, the vectors can also be interpreted as originating from a translated origin point. In this case, the v-component of vector $\boldsymbol{v}_{3a}$ has to be modified to $1-0.23 = 0.77$, to coincide with the sum of vector $\boldsymbol{v}_{1a}$ and $\boldsymbol{v}_{2b}$. The modified vector $\widetilde{\boldsymbol{v}}_{3a} = \langle 0.41, 0.77, 0.77 \rangle$ is more or less equivalent to sum II and atomic positions can be derived. Assuming the first Fe iron can be found at the origin of the unit cell at $\vec{r}_1 = (0,0,0)$, coordinates of the next atoms are set at:

$$\vec{r}_2 = \vec{r}_1 + \vec{v}_{1a} = (0.00, 0.27, 0.50)$$
$$\vec{r}_3 = \vec{r}_1 + \vec{v}_{2b} = (0.42, 0.49, 0.27)$$
$$\vec{r}_4 = \vec{r}_1 + \vec{v}_{1a} + \vec{v}_{2b} = \vec{r}_1 + \widetilde{\vec{v}}_{3a} = (0.41, 0.77, 0.77)$$

.

Knowing the space group of the structure features a center symmetry, the central point of the four atoms can be translated to the center of the unit cell. The distance between unit cell center and the central point of the Fe atoms is determined as

$$\vec{d_c} = (0.5, 0.5, 0.5) - \frac{\vec{r_4}}{2} = [0.295, 0.115, 0.115]$$

and the positions of the four iron atoms are adjusted by $\boldsymbol{d}_c$ accordingly. The translated coordinates are listed in Tab. 7.2.

Table 7.2: Positions of Fe atoms determined with the Heavy-Atom routine in comparison with the Fe positions of the solved structure listed in the *.cif*-file.
x_S, y_S, y_S...Fractional atomic coordinates in ferrocene, derived with vector superposition.
x_H, y_H, y_H...Fractional atomic coordinates derived from Harker symmetries.
x_C, y_C, y_C...Fractional atomic coordinates, listed in the *.cif*-file of the solved structure [41].

Atom	x_S	y_S	z_S	x_H	y_H	z_H	x_C	y_C	z_C
Fe1	0.295	0.115	0.115	0.290	0.115	0.115	0.2925	0.1164	0.1141
Fe2	0.295	0.385	0.615	0.290	0.385	0.615	0.2925	0.3836	0.6141
Fe3	0.715	0.605	0.385	0.710	0.615	0.385	0.7075	0.6164	0.3859
Fe4	0.705	0.885	0.885	0.710	0.885	0.885	0.7075	0.8836	0.8859

7.2.2   Harker Symmetries

To examine a Patterson map for *Harker* symmetries, knowledge of its space group is required. Depending on the crystal system and reflection conditions present in the diffraction pattern, guesses can be made if the space group is unknown. The symmetries in Patterson space can be calculated from the symmetry equivalent positions corresponding to the space group and the positions can be looked up in the "*International Table for Crystallography Volume A: Space-Group Symmetry*" [42] or in a more convenient way, on a website of the University of London [43]. Distance vector symmetries are calculated by subtracting the atomic coordinates (x,y,z) from the symmetry equivalent positions. Equivalent coordinates and Patterson symmetries of space group $P2_1/c$ can seen in Tab. 7.3.

Those symmetries are then compared with the Patterson vectors in Tab. 7.1. Vectors $\boldsymbol{v}_{1a}$ and $\boldsymbol{v}_{1b}$ were identified as Harker lines with symmetry IV, vectors $\boldsymbol{v}_{2a}$ and $\boldsymbol{v}_{2b}$ were identified as Harker planes with symmetry II, as can easily be compared by searching for Patterson vectors with values around 0.5 or 0 for the components where those values also occur in the Harker symmetries. The following

equations arise as a result and atomic coordinates (x, y, z) can be determined:
$$\text{IV} = \vec{v}_{1a} : \left\langle 0, \tfrac{1}{2} - 2\,y, \tfrac{1}{2} \right\rangle = \left\langle 0.00, 0.27, 0.50 \right\rangle$$

$$\frac{1}{2} - 2\,y = 0.27 \Rightarrow \underline{\underline{y = 0.115}} \tag{7.5}$$

$$\text{IV} = \vec{v}_{1b} : \left\langle 0, \tfrac{1}{2} - 2\,y, \tfrac{1}{2} \right\rangle = \left\langle 0.00, 0.74, 0.50 \right\rangle$$

$$\frac{1}{2} - 2\,y = 0.74 \Rightarrow \underline{\underline{y = -0.120}} \tag{7.6}$$

Here $\vec{v}_{1b}$, the longer of the two, results in a negative y coordinate.

$$\text{II} = \vec{v}_{2a} : \left\langle -2\,x, \tfrac{1}{2}, \tfrac{1}{2} - 2\,z \right\rangle = \left\langle 0.59, 0.51, 0.73 \right\rangle$$
$$2\,x = -0.59 \Rightarrow \underline{\underline{x = -0.295}}$$

$$\frac{1}{2} - 2\,z = 0.73 \Rightarrow \underline{\underline{z = -0.115}} \tag{7.7}$$

The longer of the two vectors results in negative coordinates for x and z, combining to the symmetry equivalent position $(-x, -y, -z)$ listed in Tab. 7.3.

$$\text{II} = \vec{v}_{2b} : \left\langle -2\,x, \tfrac{1}{2}, \tfrac{1}{2} - 2\,z \right\rangle = \left\langle 0.42, 0.49, 0.27 \right\rangle$$
$$\tfrac{1}{2} - 2\,z = 0.27 \Rightarrow \underline{\underline{z = 0.115}}$$
$$2\,x = -0.42,$$

and since a positive coordinate is expected, a translation into an adjacent unit cell with $x \,\epsilon\, [0, 1]$ is performed:

$$2\,x = -0.42 + 1 = 0.58 \Rightarrow \underline{x = 0.290} \tag{7.8}$$

Table 7.3: Symmetry equivalent coordinates and Patterson symmetry of $P2_1/c$

	Coordinates	Patterson symmetries
I	(x, y, z)	$\left\langle 0, 0, 0 \right\rangle$
II	$(-x, \tfrac{1}{2} + y, \tfrac{1}{2} - z)$	$\left\langle -2\,x, \tfrac{1}{2}, \tfrac{1}{2} - 2\,z \right\rangle$
III	$(-x, -y, -z)$	$\left\langle -2\,x, -2\,y, -2\,z \right\rangle$
IV	$(x, \tfrac{1}{2} - y, \tfrac{1}{2} + z)$	$\left\langle 0, \tfrac{1}{2} - 2\,y, \tfrac{1}{2} \right\rangle$

By inserting the calculated coordinates (x, y, z) into the equivalent positions in Tab. 7.3, the positions of all four Fe atoms in the structures unit cell can be determined. These positions were included next to the positions resulting from the

vector superposition and the positions reported in the solved structure in Tab.7.2. Coordinates determined by the two described methods were consistent and are practically equal to those of the solved structure of ferrocene, verifying the functionality of the implemented Heavy-Atom routine.

To test the Heavy-Atom routine for metal-organic frameworks and characterize the impact of the amount of diffraction maxima provided as input, Patterson maps for the Cu-INA framework *UFUMUD* were calculated.

7.3 Testcase *UFUMUD*

Analogous to ferrocene, a theoretical powder pattern was used to calculate Patterson maps for *UFUMUD*. Three separate maps were generated. Starting with a low amount of diffraction maxima. Limiting the input to only include peaks with scattering vector lengths q below $2.6\,\text{Å}^{-1}$, the experimental conditions of the GIXD set-up discussed in the previous chapter were imidated. A powder pattern, including 53 diffraction peaks, was used to calculate the Patterson map visualized in Fig. 7.3 a.). The Patterson map displayed in Fig. 7.3 b.) was calculated with 121 unique diffraction maxima, while for the calculation of the map presented in Fig. 7.3 c.) 3374 theoretical diffraction peaks were used. The resolution parame-
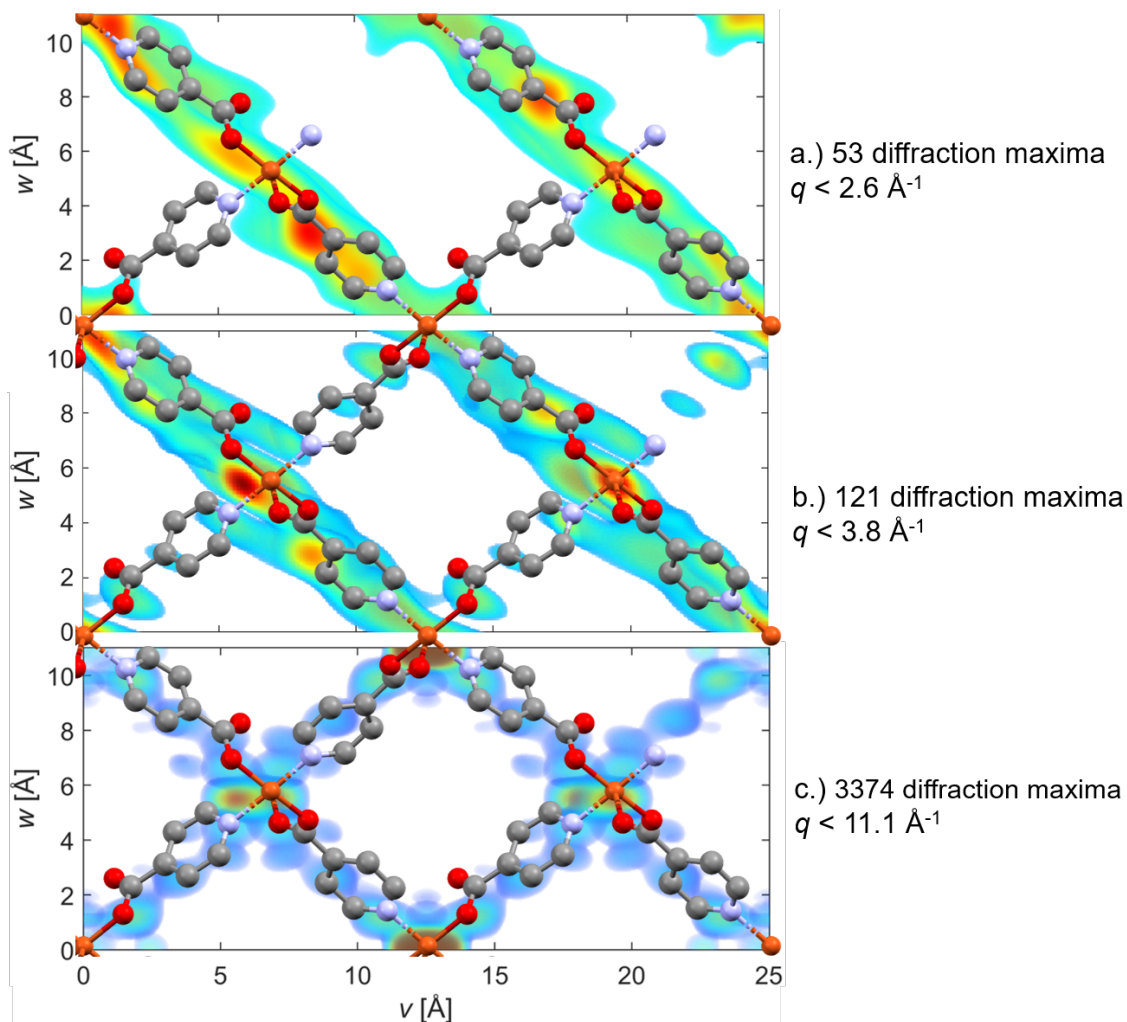
Figure 7.3: Structure of *UFUMUD* placed over three Patterson maps, with a consecutively larger number of diffraction maxima as input.

ter was $0.05\,\text{Å}$ for all three Patterson maps and the view angle is chosen along the

a-direction in which *UFUMUD* has the open channel. Placing the structure over the Patterson map shows a clear correlation between the Cu atom positions and high intensity regions in the map. The regular arrangement of metal ion and organic linker, results in a Patterson map with clearly distinguishable regions, since the occurring interatomic vectors are always the same, despite the large size of the unit cell. Unsurprisingly, a structure with large voids in the unit cell, leads to a Patterson map with volumes, where no maxima can be found.

Including more diffraction maxima for Fig. 7.3 b.) and c.) obviously improved the number and discriminability of Patterson maxima, to the point where the topology of the framework is reflected in the Patterson map. For Fig. 7.3 a.) Patterson peaks of high intensity, not coinciding with Cu atom distances, can be found.

Selected, high intensity peaks of all three maps were compared with interatomic distance vectors occurring between the four Cu atoms in the unit cell of the solved structure. The vectors found in the respective Patterson maps are listed in Tab. 7.4 next to the vectors determined from the solved structure file. Map a.) featured all four Cu–Cu vectors, but their intensities would not, necessarily, reveal them as the H–H peaks, while for maps b.) and c.), the peak intensities were ordered as expected. Vectors of map b.) appear to be less precise than vectors of map a.), which are very close to the interatomic vectors of the solved structure. Patterson vectors of map c.) were only marginally more precise, despite the substantially better representation of the topology and the large amount of distinguishable Patterson maxima. Taking this comparison into account, the use of the Heavy-Atom routine to determine the Cu atom positions in the fINA structure from the limited amount of indexed grazing-incidence diffraction peaks, does appear feasible.

Table 7.4: Interatomic vectors between the four Cu atoms in the unit cell of *UFUMUD*.
u_a, v_a, w_a...Patterson vectors, calculated with 53 diffraction maxima. Fig. 7.3 a.)
u_b, v_b, w_b...Patterson vectors, calculated with 121 diffraction maxima. Fig. 7.3 b.)
u_c, v_c, w_c...Patterson vectors, calculated with 3374 diffraction maxima. Fig. 7.3 c.)
u_S, v_S, w_S...Distance vectors of Cu atoms from the solved structure [12].

u_a	v_a	w_a	u_b	v_b	w_b	u_c	v_c	w_c	u_S	v_S	w_S
0.53	0.28	0.48	0.50	0.27	0.50	0.50	0.27	0.50	0.50	0.27	0.50
0.04	0.23	0.52	0.00	0.23	0.50	0.00	0.23	0.50	0.00	0.27	0.50
0.50	0.50	0.00	0.66	0.45	0.08	0.50	0.50	0.00	0.50	0.50	0.00
0.04	0.77	0.48	0.16	0.72	0.58	0.00	0.77	0.50	0.00	0.77	-0.50

Chapter 8

Heavy-Atom Method II: Structure solution of fINA

The novel idea to use indexed grazing-incidence diffraction maxima as input for the Heavy-Atom Method arose as a potential approach to solve the structure or at least determine the Cu atom positions of the Cu-INA framework at hand. The framework topology depends on the position of the metallic nodes, since an organic linker, per definition, has to connect two metal ions. Linker molecules are assumed to be located longitudinally between two metal sites of the framework and the molecules location and orientation are closely related to the positions of the Cu atoms.

It stands to question, if intensity distributions of grazing-incidence diffraction maxima are comparable to those recorded with single-crystal or powder diffraction methods. Ratios between intensities of GIXD peaks could deviate for some regions of reciprocal space, depending on the incidence angle ω. Diffraction peaks at $q_z = 0\,\text{Å}^{-1}$ are comparatively more intensive at lower incidence angles ω, where increased intensity due to the *Yoneda* peak [44] can be exhibited.

8.1   Experimental input for Heavy-Atom routine

To extract appropriate intensity values for the indexed diffraction peaks, the Lorentz and polarization correction factors had to be applied to the respective GIXD map. Besides determining the peak position in reciprocal space maps, the *Peak Finder* module in *GIDVis* was used to calculate the intensity elevation over the background and the peak widths in xy- and z-direction. The underlying fitting function is approximating diffraction maxima with 2D Gauss functions. The information used in

the Heavy-Atom Method is the distribution of intensity over the observable maxima with indices *hkl*, so ratios of peak intensities are sensitive factors for the success of the method. To make the comparison between observed peak intensities more accurate, the whole intensity volume was regarded. The approximation for the volume V under the curve of the Gaussian function was

$$V = 2\,\pi\,A\,\sigma_{xy}\,\sigma_z, \tag{8.1}$$

where A is the intensity elevation and σ_{xy} and σ_z are the spreads of the function in xy- and z-direction.

Considering the large number of diffraction maxima , the following investigations were performed on diffraction patterns of fINA04. Since rotating GIXD data was available and the sample was indexed using the same measurement, the GIXD pattern at $\omega = 3°$ was considered as input. However, the substantial azimuthal smearing of the fINA diffraction peaks, in combination with the minimal radial smearing influenced by the high incidence angle, made a meaningful determination of peak intensities unreliable. The high incidence angle and the lack of in-plane peaks disqualified the pattern. In Fig. 8.1 reciprocal space maps recorded at three different incidence angles are displayed. Regarding the peak shape and extend of their smearing, the diffraction pattern at $\omega = 1.0°$ appears to be more suitable for extracting intensity values as input for the Heavy-Atom Method.
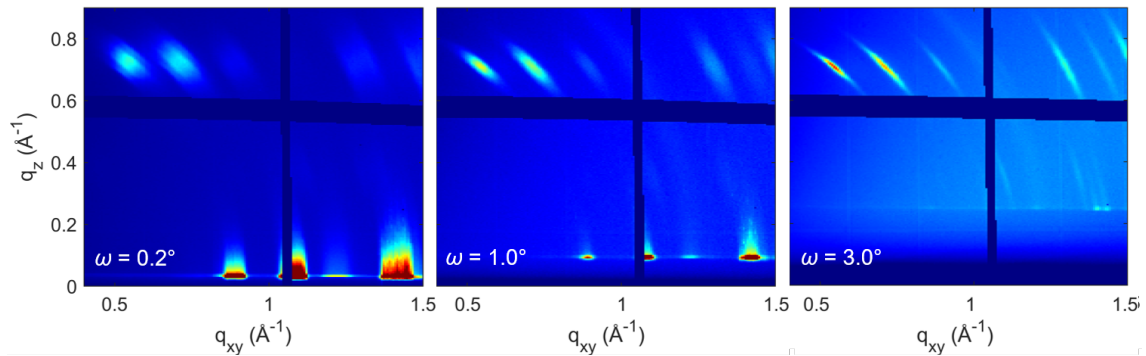
Figure 8.1: Reciprocal space maps of fINA04, recorded at incidence angle $\omega = 0.2°$, $\omega = 1.0°$ and $\omega = 3.0°$

A line scan similar to a powder pattern can be acquired by integrating intensity values of GIXD maps over q. Line scans acquired from the GIXD patterns at increasing ω were compared in Fig. 8.2. Radial smearing is noticeably stronger at $\omega = 0.2°$, than for $\omega = 1.0°$ and $3.0°$, to the point of making several maxima overlap and indistinguishable. Despite featuring much sharper peaks, crucial contributions

from in-plane peaks were obviously missing in the $\omega = 3.0°$ line scan. Contrarily, the contribution of in-plane peaks in the $\omega = 0.2°$ measurement appears to be too intense, compared with contributions from non-in-plane peaks. This is emphasized by the ratio of the three maxima between $q = 0.8$ to 1.2 Å^{-1}, where the third maxima is significantly larger than the second, due to the 220 in-plane peak. Taking the line scans and the shapes of diffraction peaks in the reciprocal space maps into account, the GIXD pattern recorded at $\omega = 1.0°$ was chosen to provide the input for the Heavy-Atom routine.
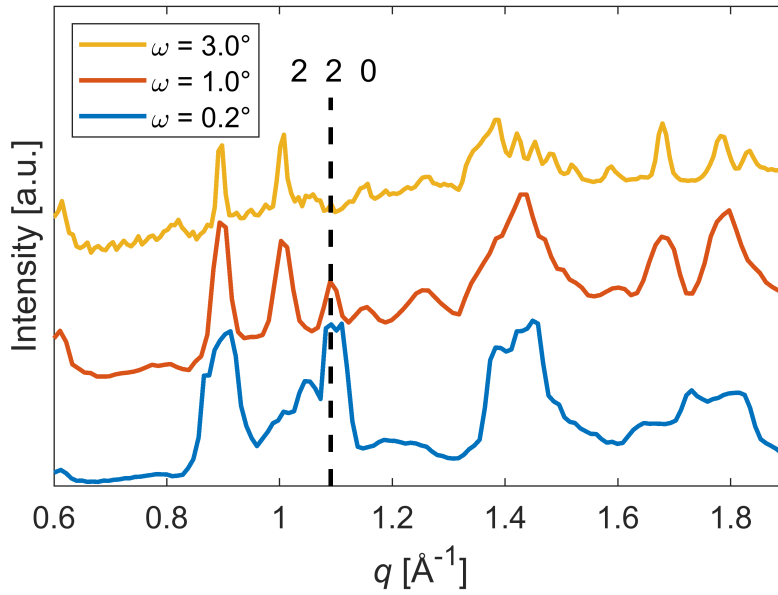
Figure 8.2: Integrated line scans of fINA04 at incidence angle $\omega = 0.2°$, $\omega = 1.0°$ and $\omega = 3.0°$, with the highlighted position of the 220 peak.

The crystal system of the unit cell was nominally determined as *triclinic*. Two unit cell angles, α and β, deviated only minimally from 90°. For the scope of the following analysis, both angles were modified to 90.0° and the crystal assumed to be *monoclinic* instead. In a monoclinic crystal system, several net planes are parallel, that would otherwise not be parallel in a triclinic system.

Table 8.1: Unit cell parameters determined by indexing of fINA04.

a	b	c	α	β	γ
14.616 Å	14.503 Å	17.667 Å	90.07°	90.33°	75.36°
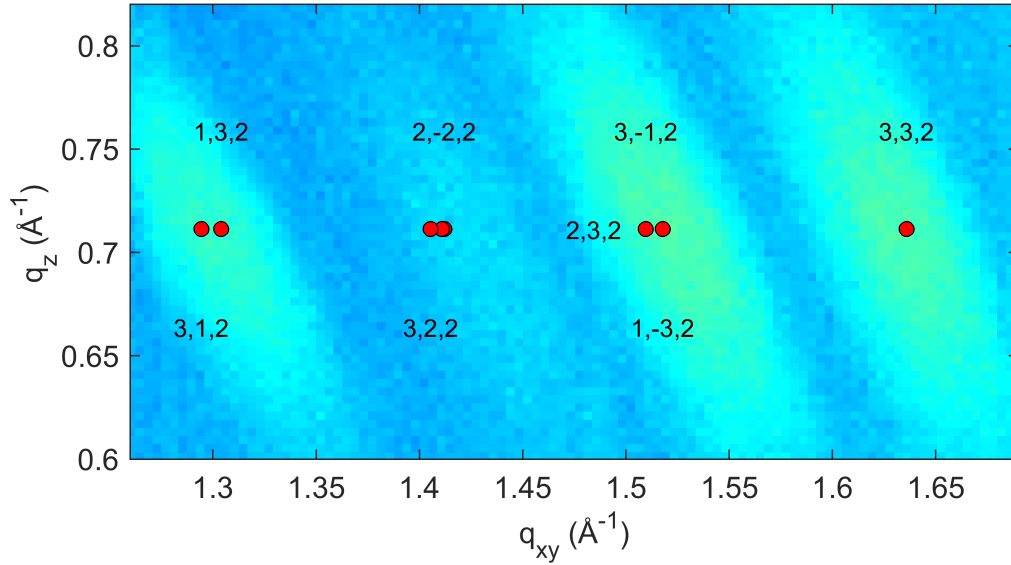
Figure 8.3: Section of the reciprocal space map of fINA04, recorded at $\omega = 1.0°$. Reflections that can be associated with the observed diffraction maxima are indicated.

Therefore their corresponding diffraction reflections occur at the same reciprocal space vector projection in q_{xy}, are regarded as *duplicates* and can be discarded. Since the lattice parameters a and b are also almost the same, the separation of reciprocal space positions of diffraction reflections in $\vec{q} = (q_{xy}, q_z)$ was by far smaller than the radial smearing of observed maxima. A multiplicity of theoretical reflections could be associated with one observed diffraction maximum, as illustrated by the eligible peaks indicated in Fig. 8.3. The lack of in-plane alignment made it not possible to separate peaks overlapping in the q_{xy} projection by rotating the sample. To create the input needed for the Heavy-Atom routine, the extracted peak intensities were simply averaged and assigned to all eligible reflections of the respective observed maxima. As an example, positions of the 132 peak and 312 peak seen in Fig. 8.3 almost coincidentally match in the (q_{xy}, q_z) projection. Both peaks would be eligible for the maximum, added to the input file and the intensity volume of their associated observed maximum divided by 2 and assigned to both of them. At higher q, the multiplicity can rise up to eight eligible indices per observed maximum and the full list used for the following calculation can be seen in the appendix in Tab. 10.1. An additional input file with solely the intensity elevation values, instead of the volume, was generated for comparison. Intensity values were extracted from 47 observed maxima and the input list bolstered to 262 entries, due to the occurring multiplicity. The file layout was akin to the established *.hkl*-file format.

8.2 Patterson Maps of fINA04

8.2.1 Disregarding the peak multiplicity: 47 input entries

A Patterson map was calculated and only the 47 diffraction maxima considered as input. The Laue indices for those peaks were chosen in a way, where the k value would always be the largest possible, from the indices of eligible peaks. As expected this wasn't resulting in a comprehensible 3D Patterson maps, as can be seen in Fig. 8.4. Currently it is only possible to display the Patterson maps in unit cells with $\alpha = \beta = \gamma = 90°$ in *Matlab*, despite the triclinic angle between the x- and y-axis for fINA04. The routine detecting the Patterson maxima was only able to
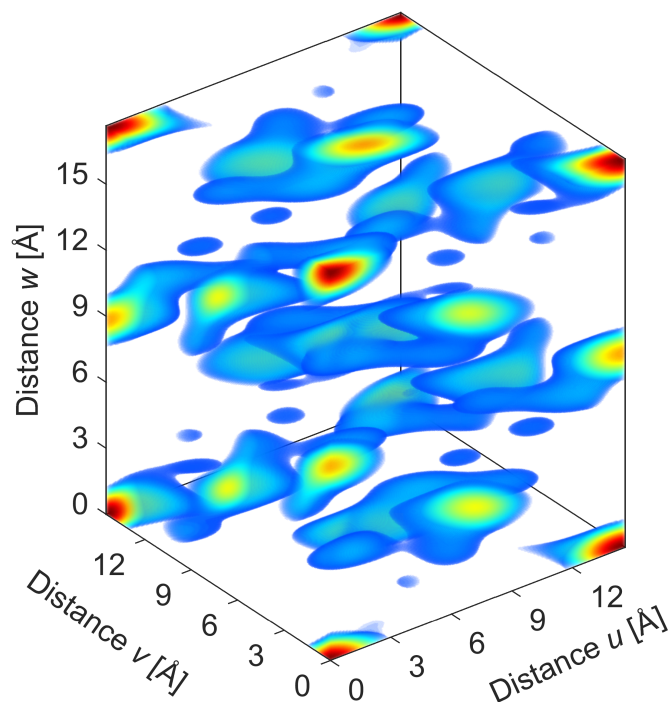
Figure 8.4: Patterson map of fINA04 calculated with disregard for the peak multiplicity.

register two unique maxima, besides the origin peak and no further analysis could be made.

8.2.2 Peak multiplicity: 262 input entries

Calculated from the *.hkl*-file bolstered to 262 entries, the 3D Patterson map in Fig. 8.5 features a great number of clearly distinguishable peaks. The view along the

w-direction and along the v-direction are displayed in Fig. 8.6 for clarity. The most intense peaks can be seen at $(u, v, w) = (0, 0, 0.5), (0.5, 0.5, 0.5)$ and $(0/0.5, 0.5/0, 0.25)$ and the rest of the detected 81 Patterson maxima is listed in Tab. 10.3 in the appendix.
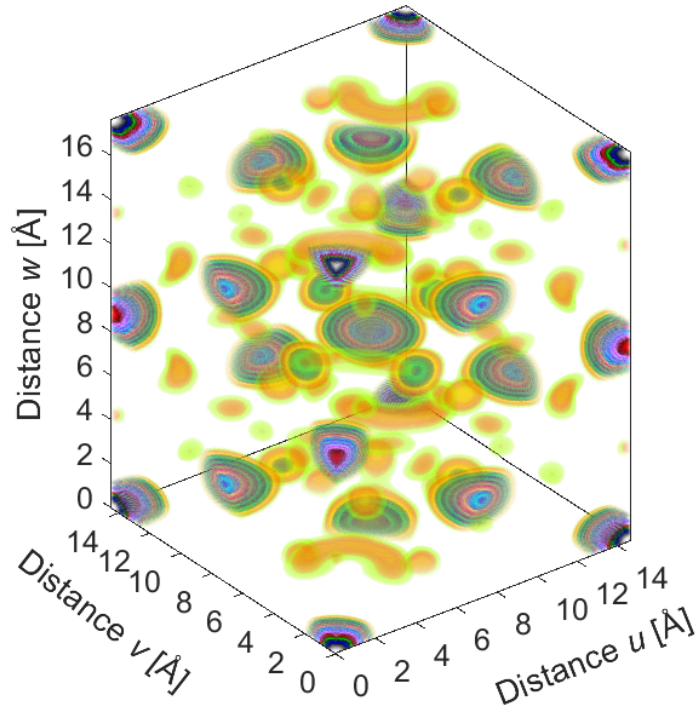
Figure 8.5: Patterson map of fINA04 calculated with 262 .*hkl* entries and converted to real space. Darker colors are more intensive regions.

Peak elevation as intensity: 262 input entries

The Patterson map displayed in Fig. 8.7 was calculated by using solely the intensity elevations of the observed peaks, rather than the intensity volume. Ratios between single value intensities and intensity volumes were deviating, so the resulting maps feature different Patterson maxima.

Most of the Patterson maxima in Fig. 8.7 also occur in Fig. 8.5 and 8.6, namely the $(u, v, w) = (0, 0, 0.5), (0.5, 0.5, 0.5)$ and $(0/0.5, 0.5/0, 0.25)$ maxima. Otherwise, the alternatively calculated map neither provided additional Patterson vectors, nor appears to be more insightful
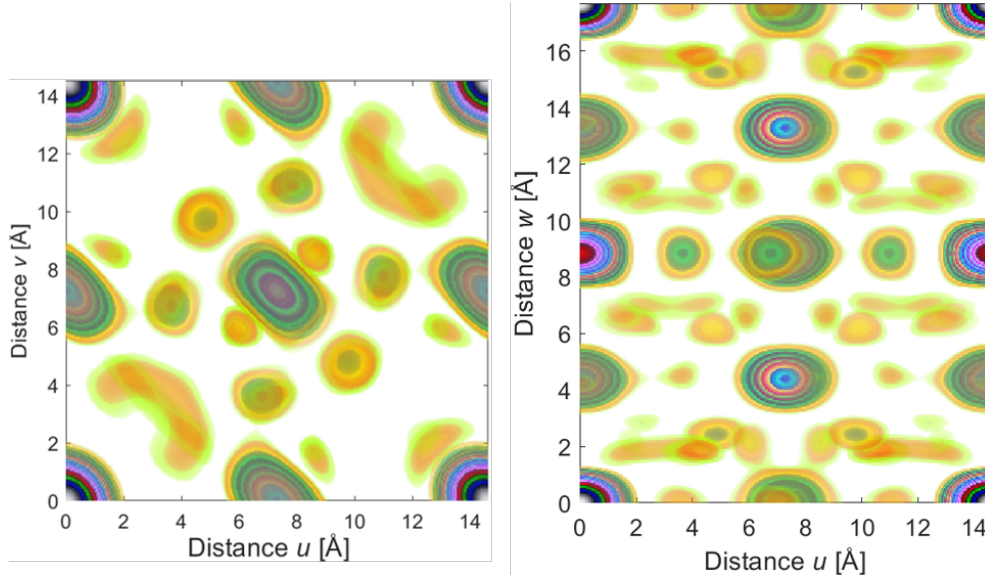
Figure 8.6: Patterson map from Fig. 8.5, viewed along the w-direction (left) and the v-direction (right). Darker colors are more intensive regions.

8.2.3 Reflection Conditions

Reflection conditions are describing the extinction of diffraction peaks with specific Laue indices hkl, depending on the space group of the crystal structure. Diffraction peaks fulfilling the conditions are in a sense "allowed" and can be observed, while those that do not, are extinct and can not observed. Since these conditions apply to all diffraction peaks, extinctions occur regularly, leading to systematic absence. The reason for extinct diffraction peaks are vanishing structure factors and the origin of their vanishing are symmetry elements in the crystal. There are three types of conditions regarding diffraction peaks with Laue indices hkl [42]:

1. General conditions: applies to all reflections hkl e.g.
   $hkl : h + k + l = k + l, h + l, h + k = 2n$ indicates a face-centered lattice.

2. Glide planes: depending on the orientation (uvw) of the glide plane, conditions for $hk0, h0l, 0kl$ arise, e.g. $h0l : h = 2n, h0l : l = 2n$ or $h0l : h + l = 2n$.

3. Screw axis: axis orientation $[uvw]$ and rotation symmetry dictate the conditions $h00, 0k0, 00l$, e.g. $h00 : h = 2n$ or $h00 : h = 4n$ indicate a screw axis with [100] orientation and 2-fold or 4-fold rotation symmetry.

The reciprocal space map of fINA04 is displayed in Fig. 8.8 with an overlay of theoretical diffraction peaks and their Laue indices. The systematic absences in rows with odd index l are quite noticeable. The peaks featured in odd l-rows
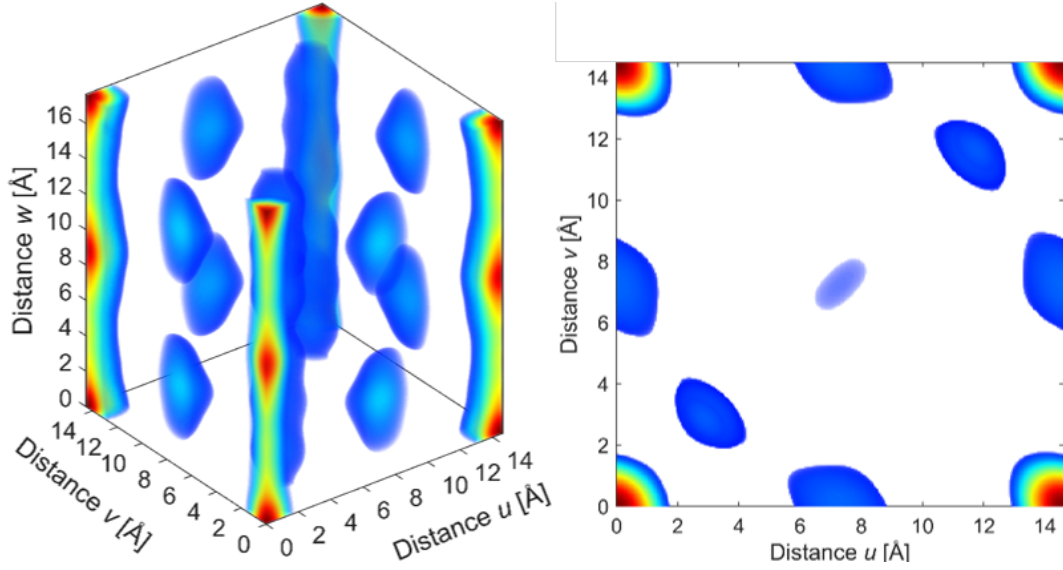
Figure 8.7: Patterson map calculated with single value intensities instead of intensity volumes.

don't appear to be higher orders of the even l peaks below and form a unique set of peaks. Maxima like the 103, 213 and 323 peaks belong to a series that is repeated in the rows with $l = 5$ and $l = 7$. The observed alternating peak series can be explained by applying the lattice centering condition $hkl : h + k + l = 2n$. Assuming the observed maxima are assigned Laue indices with an even sum of hkl, the combinations of indices h and k occurring in odd l-rows naturally have to be independent from those in even l-rows, since the sum of h and k would be even for even l and odd for odd l. The non-existent odd l specular peaks (003, 005, etc.) are underlining this assumption as well. Every observed maximum can still be assigned to one or several theoretical peaks, but some ambiguity about assignment of indices for the observed maxima is eliminated. Several consequential reflection conditions, regarding glide planes and screw axis, were observed additionally. The observed conditions are:

1. General condition: $hkl : h + k + l = 2n$

2. Glide planes: $0kl : k + l = 2n, h0l : h + l = 2n, hk0 : h + k = 2n$

3. Screw axis: $h00 : h = 2n, 0k0 : k = 2n, 00l : l = 2n,$

and are suggesting a crystal system with a body centered lattice. To find a body centered monoclinic system, unconventional space-groups with a unique z-axis instead of y-axis have to be considered. Space-groups with matching reflection conditions

81
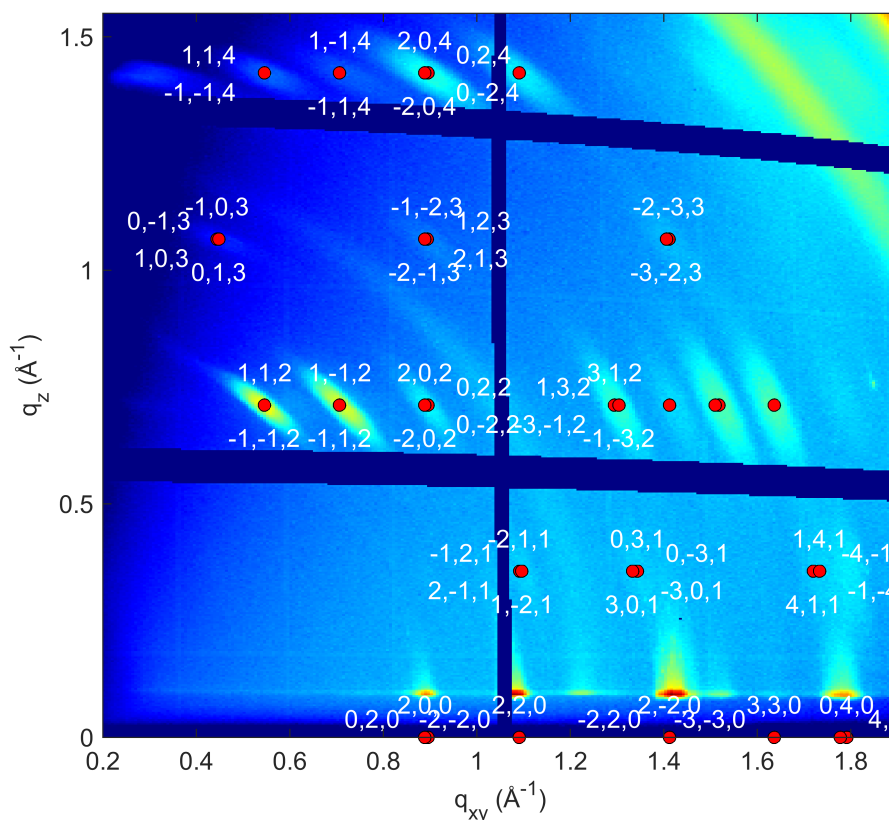
Figure 8.8: Reciprocal space map of fINA04 with indicated theoretical peaks. Some Laue indices labels have been omitted for clarity.

would be labelled by an "I" and are "$I112$", "$I11m$" and "$I112/m$". The theoretical diffraction peaks indicated in Fig. 8.8 are in accordance with the conditions listed above.

A new input file was generated and the intensity volumes of observed maxima again equally distributed to all eligible indices. The input entries can be seen in Tab. 10.2 in the appendix.

Applying reflection conditions: 172 input entries

The Patterson map displayed in Fig. 8.9 appears to be very similar to the map in Fig. 8.5 and they share the most intensive Patterson maxima. The views along the w- and v-direction reveal only minor differences. Maxima are much more defined for the Patterson map with input entries obeying the reflection conditions and the intensity of the Patterson peak at the center is comparable to that of the origin peak.
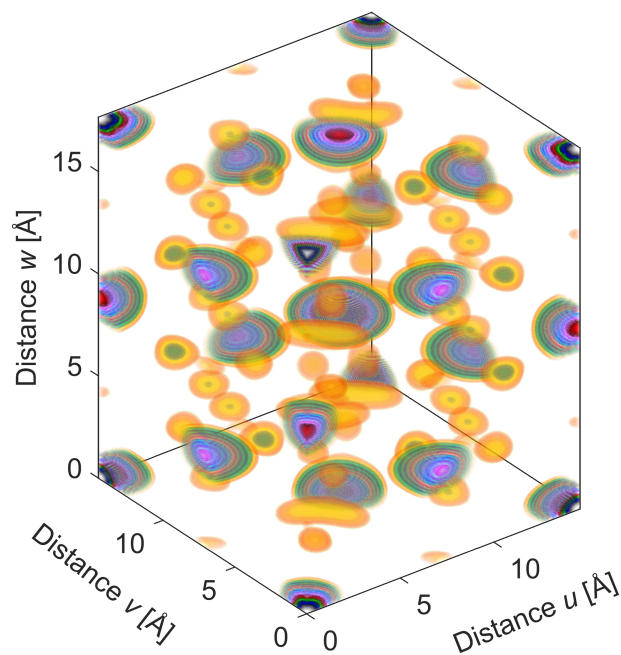
Figure 8.9: Patterson map of fINA04 calculated with 172 input entries obeying the diffraction conditions.
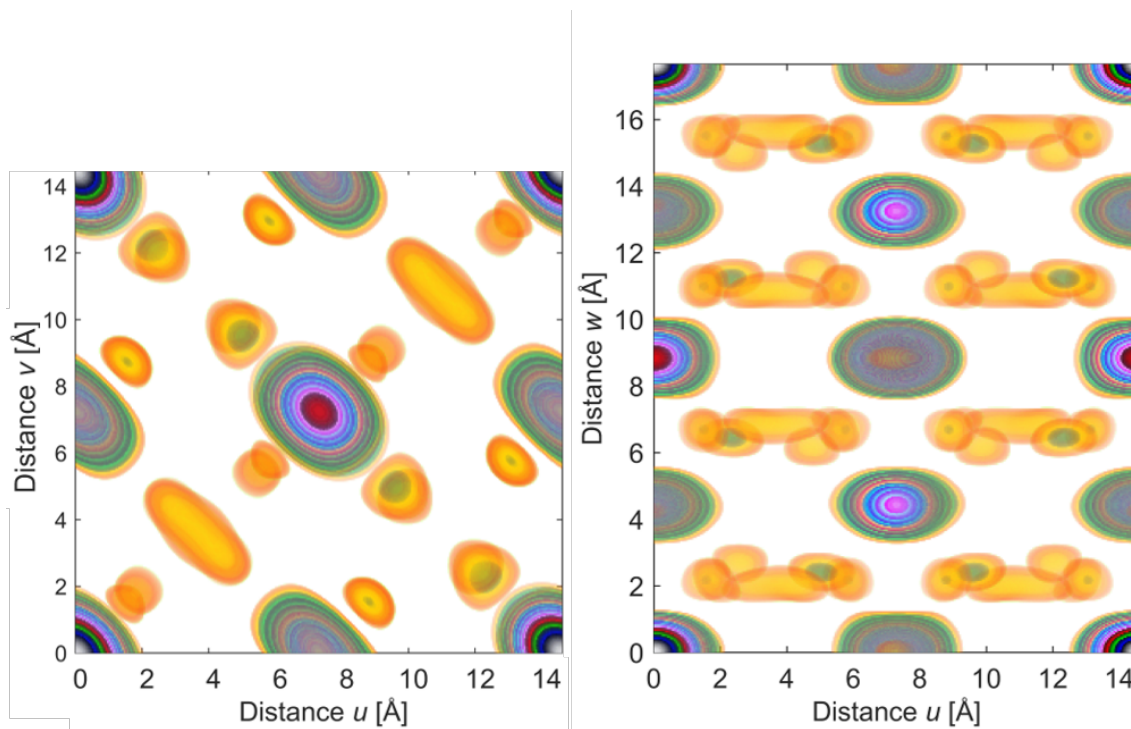
Figure 8.10: Patterson map from Fig. 8.9, viewed along the w-direction (left) and the v-direction (right).

8.3 Analysis of Patterson vectors for fINA04

Relevant detected Patterson maxima from Fig. 8.9 are listed in Tab. 8.2, next to real space lengths of the Patterson vectors. The full list can be seen in Tab. 10.4 in the appendix.

Interestingly, Patterson maximum 3 would suggest Cu atoms separated by 8.83 Å in z-direction, half of unit cell parameter c. This is in coherence with the specular scan, even though specular peaks have not been included in the input file.

Table 8.2: Patterson maxima of fINA04.

I_P...Intensity of Patterson maximum, normalized to the origin peak.

u, v, w...Fractional components of Patterson vector.

L...Length of Patterson vector in Å.

	I_P	u	v	w	L [Å]
0	10000	0	0	0	–
1	9997	0.50	0.50	0.50	14.52
2	6787	0.50	0.50	0.00	11.51
3	6786	0.00	0.00	0.50	8.83
4	5830	0.00	0.50	0.75	15.10
5	5830	0.50	0.00	0.75	15.12
6	5829	0.00	0.50	0.25	8.48
7	5829	0.50	0.00	0.25	8.52
8	1604	0.16	0.85	0.37	14.53
9	1604	0.66	0.35	0.14	12.14
10	1603	0.85	0.16	0.37	14.60
11	1603	0.34	0.66	0.14	12.04
12	1603	0.66	0.35	0.87	19.38
13	1603	0.16	0.85	0.63	17.18
14	1602	0.34	0.66	0.87	19.32
15	1602	0.85	0.16	0.63	17.24

For a better overview about what Cu–Cu distances could be expected in a Cu-INA framework, the Cu–INA–Cu and related distances of *UFUMUD* [12] are displayed in Fig. 8.11. The length between two Cu atoms linked by an INA linker, characteristic for such a framework, would be roughly 8.9 Å. Other lengths may vary due to different conformations and orientations of the benzene ring of INA.
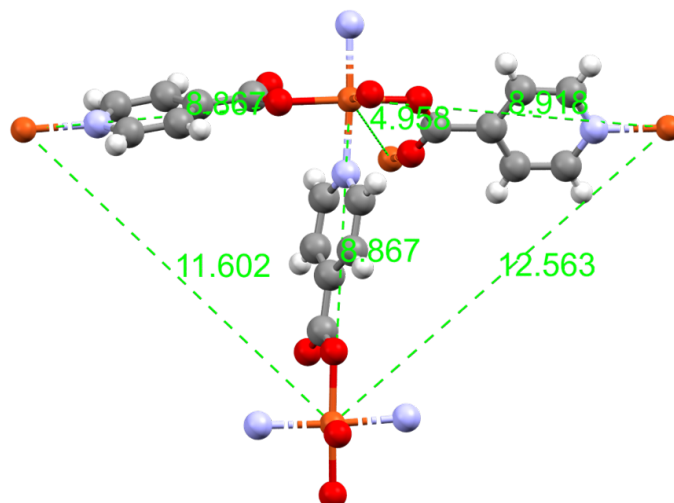
Figure 8.11: Fragment of the structure of *UFUMUD* [12] with indicated interatomic Cu–Cu lengths.

Coordination complexes containing more than one Cu atom, as discussed in chapter 1, can be ruled out by considering the acquired Patterson map. Assuming a coordination complex containing e.g. two Cu atoms such as *CIBFUR* [15], seen in Fig. 1.4. The close proximity of the Cu atoms, compared to the unit cell size, would result in a Patterson maximum close to the origin peak or even overlapping the origin peak. Shape and intensity of the origin peak would therefore be quite distorted from other maxima, which is not the case for the map in Fig. 8.9.

Since the vectors listed in Tab. 8.2 could have alternative origins, their components need to be expanded into adjacent Patterson unit cells. For the investigation of potential vector superpositions, plus/minus combinations of the vector components need to be tested. A preliminary model structure with a topology similar to *UFUMUD* can be build, by adjusting the signs of the vector components of vector 1 and vector 2. A vector superposition of adjusted vectors with sensible lengths occurs for

$$\vec{v_3} = (0.0, 0.0, 0.5) \text{ with } L = 8.83 \text{ Å}$$
$$\vec{v_2} = (-0.5, 0.5, 0) \text{ with } L = 8.90 \text{ Å}$$
$$\vec{v_1} = (-0.5, 0.5, 0.5) \text{ with } L = 12.54 \text{ Å},$$

where $\vec{v_3} + \vec{v_2} = \vec{v_1}$, which resembles distances occurring in Fig. 8.11. Vectors $\boldsymbol{v_2}$ (magenta) and $\boldsymbol{v_3}$ (blue) are illustrated in the unit cell in Fig. 8.12. Because of the characteristic Cu–INA–Cu length, INA linkers could be assumed connecting the Cu atoms corresponding to the interatomic distance vectors.

Finally, by adding vectors 6 and 7, positions for eight Cu atoms in the unit cell
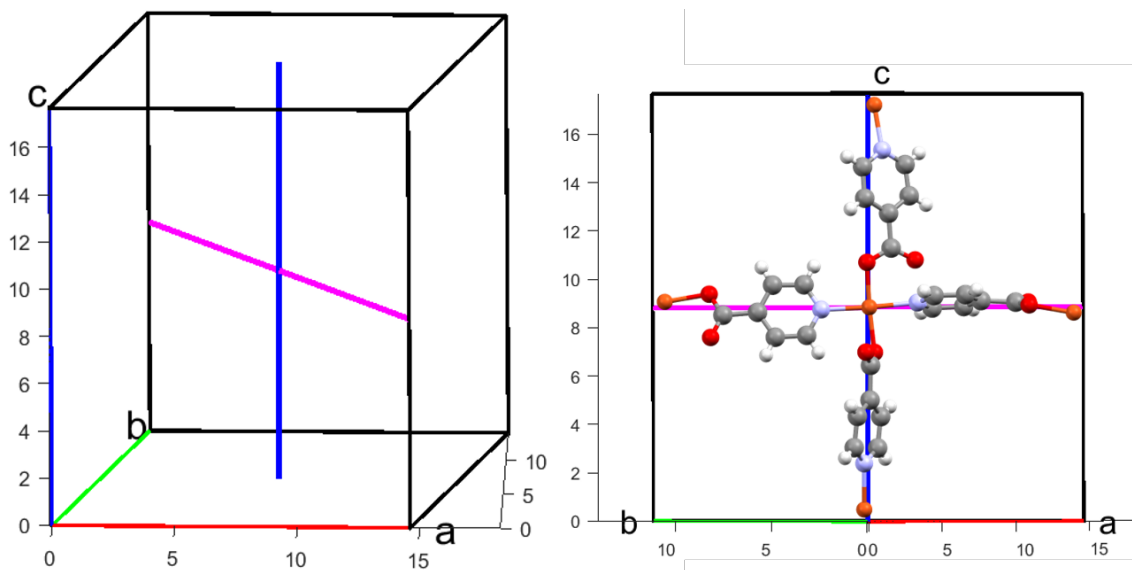
Figure 8.12: Patterson vectors v_2 (magenta) and v_3 (blue) indicated in the unit cell of fINA04 (left) and a presentation of the associated framework fragment (right).

could be determined, while the rest of the vectors from the Patterson map were discarded, since their intensity is much lower than for vectors 1 to 7. Centering the positions resulted in the fractional coordinates listed in Tab. 8.3 and the atoms depicted in the fINA unit cell in Fig. 8.13. Structure factors of the eight Cu atoms in the fINA unit cell and consecutively a theoretical powder pattern were calculated with the *Crystal Module* of *GIDVis*. The powder pattern was compared to the integrated line scan of fINA04 at $\omega = 1.0°$ in Fig. 8.13 and shows quite some similarity for the first three peaks of the experimental scan, despite not including INA at all. So far INA linkers can with certainty be placed between Cu atoms with the characteristic distance of 8.9 Å, but for a fully fleshed out crystal structure solution, information from an additional, unexplored angle would be needed.

Table 8.3: Cu atom positions (x, y, z) in the fINA unit cell, determined by Vector Superposition.

Atom	x	y	z
Cu1	0.25	0.25	0.37
Cu2	0.26	0.25	0.87
Cu3	0.25	0.75	0.12
Cu4	0.25	0.75	0.63
Cu5	0.75	0.25	0.12
Cu6	0.75	0.25	0.63
Cu7	0.75	0.75	0.37
Cu8	0.76	0.75	0.87
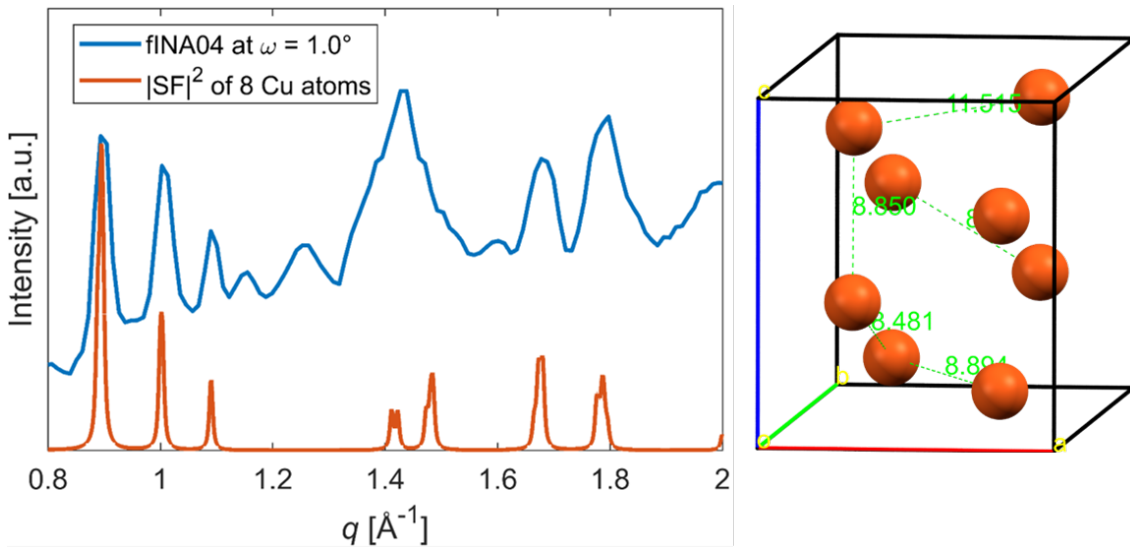
Figure 8.13: Experimental integrated line scan compared to the theoretical powder pattern (left) of the determined Cu atom positions in the unit cell (right). Interatomic distances are indicated.

Chapter 9

Conclusion

Thin film samples of a novel Cu-INA metal-organic framework, exhibiting crystalline properties, were investigated with suitable X-ray diffraction techniques. Grazing-incidence X-ray diffraction (GIXD) measurements were performed at the synchrotron facility *Elettra* and subsidized by in-house specular XRD scans. Since the frameworks were synthesized from either CuO or $Cu(OH)_2$ nanobelts substrate films, different crystal orientation were expected, depending on the substrate. While the CuO samples either exhibited uniplanar or quasi-random alignment, frameworks prepared on nanobelt films were expected to feature preferred axial alignment and were therefore investigated with rotated GIXD. Diffraction maxima of GIXD patterns and specular scans were compared and characterized for all 18 samples.

By including the specular diffraction peaks in the calculations, GIXD patterns of the Cu-INA samples were able to be indexed and a unit cell could be determined. Reciprocal lattice points of the determined unit cell were compared to the diffraction patterns of GIXD and specular XRD measurements and have been in coherence for all but three distinct samples. Besides the positions of the diffraction maxima coinciding, peak intensity distributions and systematic absences all follow the same pattern. The crystal structures of the samples are therefore demonstrably highly related.

Epitaxial relationships between Cu-INA films and their $Cu(OH)_2$ nanobelt substrate films have been revealed by the rotated GIXD experiments and were illustrated by polefigures calculated from GIXD data [20].

Heavy-Atom Methods based on the Patterson function were studied and implemented in a calculation routine, to obtain information of the crystal structure of the Cu-INA framework. For the lack of suitable software, a Heavy-Atom Methods routine had to be programmed in *Matlab* and its functionality and feasibility tested

and proven by determining the heavy atom positions in ferrocene and *UFUMUD* [12].

The novel approach of using indexed grazing-incidence diffraction data of the Cu-INA samples as input for Heavy-Atoms methods produced some preliminary results. Positions for eight Cu atoms in the determined unit cell were deduced from the calculated Patterson vectors and by knowing the characteristic Cu–INA–Cu length, guesses for some INA linker molecules could be made. Structure factors for the Cu atom positions were in partial agreement with the diffraction pattern of the sample. While the novel usage of the nowadays less used method showed some sensible and promising results, several questions about the reliability are still up in the air.

Chapter 10

Appendix

10.1 Heavy-Atom Routine: *Matlab* code

10.1.1 Calculation Patterson maps in *Matlab*

```matlab
1  function P = pattersonmap(It,h,k,l,res,a,b,c,Vol,fracmin,fracmax)
2      %It...input intensity with size (N x 1) or (1 x N)
3      %h,k,l Laue indices size (N x 1) or (1 x N)
4      %res...parameter for step size of u,v,w
5      %a,b,c...Unit cell lengths
6      %Vol...Volume of unit cell
7      %fracmin, fracmax...Limits for fractional coordinates
8
9      %P...3D Patterson map
10     It = It(:)';
11     %step sizes of fractional coordinates
12     du = res/norm(a);
13     dv = res/norm(b);
14     dw = res/norm(c);
15     %fractional coordinates
16     u = fracmin:du:fracmax;
17     v = fracmin:dv:fracmax;
18     w = fracmin:dw:fracmax;
19     %combination of three coordinates u,v,w
20     [U,V,W] = meshgrid(u,v,w);
21
22     array_size = size(U);
23     U = U(:);
```

```matlab
24      V = V(:);
25      W = W(:);
26      %for loop calculating Patterson map
27      P = 0;
28      for i = 1:size(It,2)
29          %Gives progress during calculation
30          if mod(i,round(size(It,2)/100)) == 0
31              disp(strcat(num2str(i/size(It,2)*100),' %'))
32          end
33          %Implementation Eq. 3.6
34          term = It(i).*cos(2*pi*(U*h(i) + V*k(i) + W*l(i)));
35          P = P + term;
36          if i == size(It,2)
37              disp('done')
38          end
39      end
40      %Form Patterson function to 3D array
41      P = reshape(P,array_size);
42      P = P/Vol;
43  end
```

10.1.2   Detection of Patterson Maxima

```matlab
1  K = size(u,2); %K,L,M are the dimensions [L x K x M] of the array
2  L = size(v,2);
3  M = size(w,2);
4  x = 1:K;
5  y = 1:L;
6  z = 1:M;
7  [X,Y,Z] = meshgrid(x,y,z);
8  xc = round(K/2); %Coordinates of Patterson array center
9  yc = round(L/2);
10 zc = round(M/2);
11 maxima = []; %Pre-allocation of output array.
12 while max(P(:)) > 0 %while loop detecting maxima of descending ...
       intensity
13     [Pmax,mid] = max(P(:)); %Determining the coordinates and ...
           intensity of highest Patterson maximum
14     [vid,uid,wid] = ind2sub(size(P),mid);
15
```

```matlab
16      Pshift = circshift(P,[yc-vid,xc-uid,zc-wid]); %Translating ...
            Patterson map to place origin at center
17      %Determining Distances to closest minima in x,y,z
18      Px = squeeze(Pshift(yc,:,zc));
19      xminima = find(islocalmin(Px));
20      mindx = min(abs(xc-xminima));
21
22      Py = squeeze(Pshift(:,xc,zc));
23      yminima = find(islocalmin(Py));
24      mindy = min(abs(yc-yminima));
25
26      Pz = squeeze(Pshift(yc,xc,:));
27      zminima = find(islocalmin(Pz));
28      mindz = min(abs(zc-zminima));
29      %if no minima are found, the search is ended and the while ...
            loop terminated
30      if isempty(mindx) || isempty(mindy) || isempty(mindz)
31          P = circshift(Pshift,-[yc-vid,xc-uid,zc-wid]);
32          break
33      end
34      %Ellipsoid approx. peaks is used to cut the peak out of the ...
            Patterson map
35      ellipse = ( (X-xc).^2/(mindx).^2 + (Y-yc).^2/(mindy).^2 + ...
            (Z-zc).^2/(mindz).^2) <= 1;
36      Pshift(ellipse) = 0;
37      %Additional criteria to terminate the while loop.
38      if size(maxima,1) > 4 && (Pmax/maxima(1,1) < 0.05) || ...
            size(maxima,1) > 500
39          P = circshift(Pshift,-[yc-vid,xc-uid,zc-wid]);
40          break
41      end
42
43      maxima(end+1,1) = Pmax; %Detected peak intensity
44      maxima(end,2) = uid; maxima(end,3) = vid; maxima(end,4) = ...
            wid; %Peak coordinates
45      maxima(end,5) = mindx;maxima(end,6) = mindy;maxima(end,7) = ...
            mindz; %Peak widths
46      P = circshift(Pshift,-[yc-vid,xc-uid,zc-wid]); %Translating ...
            P to its original state
47  end
48  %change coordinates at upper boundary (value 1) to 0
49  L = maxima(:,2) == length(u);
```

```matlab
50  maxima(end+1:end+numel(find(L)),:) = ...
        [maxima(L,1),ones(numel(find(L)),1),maxima(L,3:end)];
51  L = maxima(:,3) == length(v);
52  maxima(end+1:end+numel(find(L)),:) = ...
        [maxima(L,1:2),ones(numel(find(L)),1),maxima(L,4:end)];
53  L = maxima(:,4) == length(w);
54  maxima(end+1:end+numel(find(L)),:) = ...
        [maxima(L,1:3),ones(numel(find(L)),1),maxima(L,5:end)];
55  %Converting the coordinates to fractional coordinates
56  Patterson_Vectors(:,1) = maxima(:,1);
57  Patterson_Vectors(:,3) = round(u(maxima(:,2)),2); %coord. u
58  Patterson_Vectors(:,4) = round(v(maxima(:,3)),2); %coord. v
59  Patterson_Vectors(:,5) = round(w(maxima(:,4)),2); %coord. w
60  Patterson_Vectors(:,6) = frac2real(Patterson_Vectors(:,3:5),A); ...
        %real space length of <u,v,w> in Angstroem;
61  Patterson_Vectors(:,7:9) = ...
        (A*[maxima(:,5)'*du;maxima(:,6)'*dv;maxima(:,7)'*dw])';%somewhat ...
        like the Patterson peak width without physical meaning.
```

10.1.3 Converting fractional to real space vectors

```matlab
1  function [real_length,real_coord] = ...
        frac2real(frac_coord,lattice_vec_matrix)
2  %frac_coord needs to be n times 3 matrix
3  % (n,1) = x fractional coord. between 0 and 1
4  % (n,2) = y fractional coord. between 0 and 1
5  % (n,3) = z fractional coord. between 0 and 1
6  % lattice_vec_matrix should be array of a_vec, b_vec, c_vec so ...
        (3 x 3)
7  A = lattice_vec_matrix;
8  %Matrix multiplication to calculate real space vector ...
        compononts [in Angstroem]
9  real_coord = (A*frac_coord')';
10 % Real space Length of vector [in Angstroem]
11 real_length = sqrt((real_coord(:,1)).^2 + (real_coord(:,2)).^2 ...
        +(real_coord(:,3)).^2);
12 end % function
```

10.2 Input files for Heavy-Atom Routine

Table 10.1: Input entries for Patterson map of fINA04 in Fig. 8.5

h, k, l...Laue indices.

I...Intensity of diffraction peaks.

h	k	l	I [a.u.]
-1	-1	2	3139
1	1	2	3139
1	-1	2	2499
-1	1	2	2499
-1	-2	2	128
2	1	2	128
2	0	2	128
1	2	2	128
0	-2	2	128
0	2	2	128
-2	0	2	128
-2	-1	2	128
-1	0	3	79
1	0	3	79
0	-1	3	79
0	1	3	79
-1	-2	3	33
2	1	3	33
1	2	3	33
0	2	3	33
-2	0	3	33
2	0	3	33
-2	-1	3	33
0	-2	3	33
3	1	2	383
-3	-1	2	383
1	3	2	383
continued			Continued on next page

Table10.1 – continued from previous page

h	k	l	I [a.u.]
-1	-3	2	383
2	-2	2	78
3	2	2	78
2	3	2	78
-2	-3	2	78
-2	2	2	78
-3	-2	2	78
1	-3	2	466
3	-1	2	466
-1	3	2	466
-3	1	2	466
-3	-3	2	882
3	3	2	882
2	-2	3	45
3	2	3	45
2	3	3	45
-2	-3	3	45
-2	2	3	45
-3	-2	3	45
-1	-5	2	131
5	1	2	131
1	5	2	131
-5	-1	2	131
-4	-2	2	21
4	2	2	21
4	0	2	21
3	-2	2	21
2	-3	2	21
2	4	2	21
0	-4	2	21
0	4	2	21
			Continued on next page

95

Table10.1 – continued from previous page

h	k	l	I [a.u.]
-2	-4	2	21
-2	3	2	21
-3	2	2	21
-4	0	2	21
-5	-3	2	73
5	3	2	73
3	5	2	73
-3	-5	2	73
1	-4	1	60
4	-1	1	60
4	3	1	60
3	4	1	60
-1	4	1	60
-3	-4	1	60
-4	-3	1	60
-4	1	1	60
0	4	1	45
0	-4	1	45
4	0	1	45
4	2	1	45
3	-2	1	45
2	-3	1	45
2	4	1	45
-2	-4	1	45
-2	3	1	45
-3	2	1	45
-4	0	1	45
-4	-2	1	45
1	4	1	46
4	1	1	46
-4	-1	1	46
			Continued on next page

Table10.1 – continued from previous page

h	k	l	I [a.u.]
-1	-4	1	46
0	3	1	207
-3	0	1	207
0	-3	1	207
3	0	1	207
-2	-2	1	43
-2	1	1	43
-1	2	1	43
2	2	1	43
2	-1	1	43
1	-2	1	43
-1	-2	4	256
2	1	4	256
2	0	4	256
1	2	4	256
0	-2	4	256
0	2	4	256
-2	0	4	256
-2	-1	4	256
-2	-2	4	213
2	2	4	213
2	-1	4	213
1	-2	4	213
-1	2	4	213
-2	1	4	213
1	-1	4	189
-1	1	4	189
-1	-1	4	360
1	1	4	360
1	-3	4	423
3	-1	4	423
			Continued on next page

Table10.1 – continued from previous page

h	k	l	I [a.u.]
-1	3	4	423
-3	1	4	423
-4	0	4	68
4	2	4	68
4	0	4	68
3	-2	4	68
2	-3	4	68
2	4	4	68
0	-4	4	68
0	4	4	68
-2	-4	4	68
-2	3	4	68
-3	2	4	68
-4	-2	4	68
3	1	4	10
-3	-1	4	10
1	3	4	10
-1	-3	4	10
-1	0	5	157
1	0	5	157
0	-1	5	157
0	1	5	157
-1	-2	5	59
2	1	5	59
1	2	5	59
0	2	5	59
-2	0	5	59
2	0	5	59
-2	-1	5	59
0	-2	5	59
2	-2	5	16
			Continued on next page

Table10.1 – continued from previous page

h	k	l	I [a.u.]
3	2	5	16
2	3	5	16
-2	-3	5	16
-2	2	5	16
-3	-2	5	16
-1	-1	6	561
1	1	6	561
1	-1	6	42
-1	1	6	42
-1	-2	6	93
2	1	6	93
1	2	6	93
0	2	6	93
-2	0	6	93
2	0	6	93
-2	-1	6	93
0	-2	6	93
-4	0	6	3
4	2	6	3
4	0	6	3
3	-2	6	3
2	-3	6	3
2	4	6	3
0	-4	6	3
0	4	6	3
-2	-4	6	3
-2	3	6	3
-3	2	6	3
-4	-2	6	3
-1	-2	7	10
2	1	7	10
			Continued on next page

Table10.1 – continued from previous page

h	k	l	I [a.u.]
1	2	7	10
0	2	7	10
-2	0	7	10
2	0	7	10
-2	-1	7	10
0	-2	7	10
-2	-2	7	26
2	2	7	26
2	-1	7	26
1	-2	7	26
-1	2	7	26
-2	1	7	26
-1	-2	8	59
2	1	8	59
1	2	8	59
0	2	8	59
-2	0	8	59
2	0	8	59
-2	-1	8	59
0	-2	8	59
-2	-2	8	138
2	2	8	138
2	-1	8	138
1	-2	8	138
-1	2	8	138
-2	1	8	138
2	0	0	1099
2	1	0	1099
1	2	0	1099
0	2	0	1099
0	-2	0	1099
			Continued on next page

Table10.1 – continued from previous page

h	k	l	I [a.u.]
-2	0	0	1099
-2	-1	0	1099
-1	-2	0	1099
2	-1	0	3765
2	2	0	3765
-1	2	0	3765
1	-2	0	3765
-2	1	0	3765
-2	-2	0	3765
3	1	0	775
1	3	0	775
-1	-3	0	775
-3	-1	0	775
3	2	0	4160
2	-2	0	4160
2	3	0	4160
-2	-3	0	4160
-2	2	0	4160
-3	-2	0	4160
3	-1	0	676
1	-3	0	676
-1	3	0	676
-3	1	0	676
3	3	0	277
-3	-3	0	277
-4	0	0	876
-4	-2	0	876
-3	2	0	876
-2	3	0	876
-2	-4	0	876
0	4	0	876
			Continued on next page

Table10.1 – continued from previous page

h	k	l	I [a.u.]
0	-4	0	876
2	4	0	876
2	-3	0	876
3	-2	0	876
4	0	0	876
4	2	0	876
3	-3	0	450
4	-2	0	450
-3	3	0	450
-4	2	0	450
2	5	0	450
2	-4	0	450
-2	4	0	450
-2	-5	0	450
5	2	0	450
-5	-2	0	450

Table 10.2: Input file for Patterson map of fINA04 in Fig. 8.9. Chosen Laue indices are obeying the reflection conditions.

h, k, l...Laue indices.

I...Intensity of diffraction peaks.

h	k	l	I [a.u.]
-1	-1	2	3139
1	1	2	3139
1	-1	2	2499
-1	1	2	2499
2	0	2	128
0	-2	2	128
0	2	2	128
-2	0	2	128
			Continued on next page

Table 10.2 – continued from previous page

h	k	l	I [a.u.]
-1	0	3	79
1	0	3	79
0	-1	3	79
0	1	3	79
-1	-2	3	33
2	1	3	33
1	2	3	33
-2	-1	3	33
3	1	2	383
-3	-1	2	383
1	3	2	383
-1	-3	2	383
2	-2	2	78
-2	2	2	78
1	-3	2	466
3	-1	2	466
-1	3	2	466
-3	1	2	466
-3	-3	2	882
3	3	2	882
3	2	3	45
2	3	3	45
-2	-3	3	45
-3	-2	3	45
-1	-5	2	131
5	1	2	131
1	5	2	131
-5	-1	2	131
-4	-2	2	21
4	2	2	21
4	0	2	21
			Continued on next page

103

Table 10.2 – continued from previous page

h	k	l	I [a.u.]
2	4	2	21
0	-4	2	21
0	4	2	21
-2	-4	2	21
-4	0	2	21
-5	-3	2	73
5	3	2	73
3	5	2	73
-3	-5	2	73
1	-4	1	60
4	-1	1	60
4	3	1	60
3	4	1	60
-1	4	1	60
-3	-4	1	60
-4	-3	1	60
-4	1	1	60
3	-2	1	45
2	-3	1	45
-2	3	1	45
-3	2	1	45
1	4	1	46
4	1	1	46
-4	-1	1	46
-1	-4	1	46
0	3	1	207
-3	0	1	207
0	-3	1	207
3	0	1	207
-2	1	1	43
-1	2	1	43

Table 10.2 – continued from previous page

h	k	l	I [a.u.]
2	-1	1	43
1	-2	1	43
2	0	4	256
0	-2	4	256
0	2	4	256
-2	0	4	256
-2	-2	4	213
2	2	4	213
1	-1	4	189
-1	1	4	189
-1	-1	4	360
1	1	4	360
1	-3	4	423
3	-1	4	423
-1	3	4	423
-3	1	4	423
-4	0	4	68
4	2	4	68
4	0	4	68
2	4	4	68
0	-4	4	68
0	4	4	68
-2	-4	4	68
-4	-2	4	68
3	1	4	10
-3	-1	4	10
1	3	4	10
-1	-3	4	10
-1	0	5	157
1	0	5	157
0	-1	5	157
			Continued on next page

Table 10.2 – continued from previous page

h	k	l	I [a.u.]
0	1	5	157
-1	-2	5	59
2	1	5	59
1	2	5	59
-2	-1	5	59
3	2	5	16
2	3	5	16
-2	-3	5	16
-3	-2	5	16
-1	-1	6	561
1	1	6	561
1	-1	6	42
-1	1	6	42
0	2	6	93
-2	0	6	93
2	0	6	93
0	-2	6	93
-4	0	6	3
4	2	6	3
4	0	6	3
2	4	6	3
0	-4	6	3
0	4	6	3
-2	-4	6	3
-4	-2	6	3
-1	-2	7	10
2	1	7	10
1	2	7	10
-2	-1	7	10
2	-1	7	26
1	-2	7	26
			Continued on next page

Table 10.2 – continued from previous page

h	k	l	I [a.u.]
-1	2	7	26
-2	1	7	26
0	2	8	59
-2	0	8	59
2	0	8	59
0	-2	8	59
-2	-2	8	138
2	2	8	138
2	0	0	1099
0	2	0	1099
0	-2	0	1099
-2	0	0	1099
2	2	0	3765
-2	-2	0	3765
3	1	0	775
1	3	0	775
-1	-3	0	775
-3	-1	0	775
2	-2	0	4160
-2	2	0	4160
3	-1	0	676
1	-3	0	676
-1	3	0	676
-3	1	0	676
3	3	0	277
-3	-3	0	277
-4	0	0	876
-4	-2	0	876
-2	-4	0	876
0	4	0	876
0	-4	0	876
			Continued on next page

Table 10.2 – continued from previous page

h	k	l	I [a.u.]
2	4	0	876
4	0	0	876
4	2	0	876
3	-3	0	450
4	-2	0	450
-3	3	0	450
-4	2	0	450
2	-4	0	450
-2	4	0	450

10.3   Patterson Vectors of fINA04

Table 10.3: Patterson maxima from the map in Fig. 8.5 for 262 input peaks.

I_P...Intensity of Patterson maxima.

u, v, w...Patterson vector components.

L...Real space vector length in Å.

I_P	u	v	w	L [Å]
6774	0.00	0.00	0.50	8.83
4696	0.50	0.50	0.50	14.52
4297	0.00	0.50	0.75	15.15
4297	0.50	0.00	0.75	15.17
4297	0.00	0.50	0.25	8.48
4297	0.50	0.00	0.25	8.52
2907	0.50	0.50	0.00	11.51
1935	0.54	0.75	0.50	17.38
1934	0.25	0.46	0.50	12.21
1934	0.46	0.25	0.50	12.21
1934	0.75	0.54	0.50	17.43
1554	0.67	0.33	0.14	12.18
1553	0.33	0.67	0.14	12.10
1553	0.67	0.33	0.86	19.37
				Continued on next page

Table 10.3 – continued from previous page

I_{P}	u	v	w	L [Å]
1553	0.33	0.67	0.86	19.32
1406	0.32	0.68	0.35	13.45
1406	0.68	0.32	0.35	13.47
1406	0.32	0.68	0.65	16.58
1406	0.68	0.32	0.65	16.59
1293	0.59	0.59	0.88	20.65
1290	0.41	0.41	0.88	18.11
1290	0.59	0.59	0.13	13.83
1287	0.41	0.41	0.13	9.64
1217	0.24	0.47	0.00	8.43
1216	0.76	0.53	0.00	14.98
1216	0.53	0.76	0.00	15.01
1216	0.47	0.24	0.00	8.49
1168	0.87	0.13	0.36	14.77
1168	0.87	0.13	0.64	17.43
1168	0.13	0.87	0.36	14.68
1168	0.13	0.87	0.64	17.36
1134	0.71	0.83	0.89	23.71
1134	0.29	0.17	0.89	16.72
1134	0.71	0.83	0.11	17.82
1134	0.17	0.30	0.11	5.79
1115	0.87	0.71	0.10	18.27
1115	0.87	0.71	0.90	24.12
1114	0.29	0.13	0.10	5.45
1109	0.13	0.29	0.90	16.64
1092	0.90	0.41	0.62	19.16
1092	0.41	0.90	0.62	19.10
1092	0.90	0.41	0.38	17.09
1092	0.10	0.59	0.62	14.22
1092	0.60	0.10	0.62	14.29
1091	0.41	0.90	0.38	17.02
				Continued on next page

Table 10.3 – continued from previous page

I_P	u	v	w	L [Å]
1091	0.60	0.10	0.38	11.36
1091	0.10	0.59	0.38	11.30
1072	0.25	0.49	0.26	9.78
1072	0.52	0.76	0.26	15.46
1072	0.75	0.51	0.26	15.44
1072	0.52	0.76	0.75	19.82
1072	0.25	0.49	0.75	15.80
1072	0.49	0.25	0.26	9.80
1072	0.48	0.25	0.75	15.78
1072	0.75	0.51	0.75	19.81
1065	0.00	0.00	0.76	13.44
1064	0.00	0.00	0.24	4.26
1029	0.40	0.40	0.37	11.32
1029	0.60	0.60	0.37	15.21
1028	0.40	0.40	0.64	14.60
1028	0.60	0.60	0.63	17.75
1024	0.85	0.71	0.60	20.86
1023	0.71	0.85	0.60	20.85
1023	0.29	0.16	0.60	11.91
1023	0.15	0.29	0.60	11.89
1023	0.71	0.85	0.40	19.24
1023	0.85	0.71	0.40	19.27
1023	0.15	0.29	0.40	8.81
1023	0.29	0.16	0.40	8.84
946	0.88	0.42	0.12	15.67
946	0.88	0.42	0.88	21.93
946	0.42	0.88	0.12	15.61
946	0.42	0.88	0.88	21.89
946	0.12	0.58	0.12	9.33
946	0.12	0.58	0.88	17.96
946	0.59	0.12	0.88	18.00
				Continued on next page

Table 10.3 – continued from previous page

I_P	u	v	w	L [Å]
946	0.59	0.12	0.12	9.40
944	0.15	0.85	0.16	13.38
944	0.85	0.15	0.16	13.40
943	0.15	0.85	0.84	19.80
943	0.85	0.15	0.84	19.81

Table 10.4: Patterson maxima from the map in Fig. 8.9 for 172 input peaks.

I_P...Intensity of Patterson maxima.

u, v, w...Patterson vector components.

L...Real space vector length in Å.

I_P	u	v	w	L [Å]
9997	0.50	0.50	0.50	14.52
6787	0.50	0.50	0.00	11.51
6786	0.00	0.00	0.50	8.85
5830	0.00	0.50	0.75	15.10
5830	0.50	0.00	0.75	15.12
5829	0.00	0.50	0.25	8.48
5829	0.50	0.00	0.25	8.52
1604	0.16	0.85	0.37	14.53
1604	0.66	0.35	0.14	12.14
1603	0.85	0.16	0.37	14.60
1603	0.34	0.66	0.14	12.04
1603	0.66	0.35	0.87	19.38
1603	0.16	0.85	0.63	17.18
1602	0.34	0.66	0.87	19.32
1602	0.85	0.16	0.63	17.24
1432	0.89	0.40	0.12	15.71
1432	0.40	0.89	0.12	15.65
1432	0.90	0.39	0.62	19.09
1432	0.39	0.90	0.62	19.04
1432	0.60	0.11	0.12	9.56
				Continued on next page

Table 10.4 – continued from previous page

I_P	u	v	w	L $[\AA]$
1432	0.11	0.60	0.12	9.46
1432	0.89	0.40	0.88	21.96
1432	0.39	0.90	0.38	16.91
1432	0.90	0.39	0.38	16.98
1432	0.60	0.11	0.88	18.08
1432	0.40	0.89	0.88	21.91
1432	0.11	0.60	0.88	18.03
1432	0.10	0.61	0.62	14.41
1432	0.61	0.10	0.62	14.43
1431	0.61	0.10	0.38	11.48
1431	0.10	0.61	0.38	11.44
1399	0.33	0.68	0.65	16.57
1399	0.82	0.18	0.15	13.20
1399	0.82	0.18	0.85	19.80
1399	0.17	0.82	0.15	13.10
1399	0.17	0.82	0.85	19.74
1399	0.67	0.32	0.65	16.58
1399	0.33	0.68	0.35	13.44
1398	0.67	0.32	0.35	13.45
1385	0.72	0.77	0.11	17.25
1385	0.73	0.76	0.89	23.21
1385	0.26	0.22	0.61	12.22
1385	0.23	0.28	0.11	6.24
1385	0.24	0.28	0.89	16.73
1385	0.77	0.74	0.61	20.55
1384	0.27	0.22	0.39	8.88
1384	0.73	0.78	0.39	18.71
1278	0.00	0.50	0.00	7.25
1278	0.50	0.00	0.00	7.29
1277	0.00	0.50	0.50	11.44
1277	0.50	0.00	0.50	11.47
				Continued on next page

Table 10.4 – continued from previous page

I_{P}	u	v	w	L [Å]
1252	0.38	0.39	0.37	10.99
1251	0.62	0.61	0.37	15.65
1250	0.12	0.11	0.13	3.54
1245	0.89	0.88	0.13	20.50
1239	0.89	0.88	0.87	25.58
1238	0.38	0.39	0.63	14.25
1238	0.12	0.11	0.87	15.58
1236	0.61	0.61	0.63	17.96
1193	0.59	0.60	0.88	20.65
1190	0.91	0.91	0.38	21.93
1189	0.88	0.88	0.14	20.50
1185	0.91	0.91	0.63	23.64
1183	0.12	0.11	0.11	3.32
1183	0.41	0.41	0.13	9.64
1182	0.10	0.09	0.37	6.91
1181	0.62	0.62	0.64	18.18
1180	0.88	0.88	0.86	25.37
1180	0.41	0.41	0.88	18.08
1179	0.38	0.39	0.39	11.20
1175	0.09	0.09	0.63	11.25
1175	0.62	0.61	0.39	15.75
1174	0.89	0.88	0.86	25.39
1174	0.59	0.59	0.13	13.83
1172	0.89	0.89	0.86	25.46
1171	0.89	0.88	0.89	25.77
1170	0.88	0.89	0.86	25.34
1168	0.90	0.88	0.89	25.73
1167	0.38	0.39	0.61	14.06
1164	0.12	0.11	0.89	15.86
1161	0.89	0.88	0.86	25.40
1161	0.88	0.89	0.86	25.40
				Continued on next page

Table 10.4 – continued from previous page

I_{P}	u	v	w	L [Å]
1156	0.89	0.87	0.86	25.33
1156	0.89	0.89	0.89	25.78
1150	0.90	0.88	0.86	25.50
1146	0.90	0.87	0.89	25.70
1141	0.90	0.87	0.86	25.40
1141	0.38	0.39	0.35	10.85
1141	0.62	0.62	0.35	15.52
1141	0.89	0.88	0.89	25.78
1141	0.39	0.38	0.35	10.86
1137	0.89	0.87	0.86	25.34
1135	0.38	0.38	0.35	10.79
1135	0.38	0.39	0.35	10.85
1134	0.39	0.39	0.35	10.92
1134	0.89	0.89	0.86	25.56
1134	0.39	0.38	0.35	10.85
1134	0.39	0.39	0.35	10.91
1132	0.90	0.87	0.89	25.75
1131	0.89	0.89	0.89	25.81

Bibliography

[1] Hailian Li et al. "Design and synthesis of an exceptionally stable and highly porous metal-organic framework". In: *Nature* 402.6759 (1999), pp. 276–279. ISSN: 1476-4687. DOI: `10.1038/46248`. URL: `https://doi.org/10.1038/46248`.

[2] Susumu Kitagawa and Mitsuru Kondo. "Functional Micropore Chemistry of Crystalline Metal Complex-Assembled Compounds". In: *Bulletin of the Chemical Society of Japan* 71.8 (1998), pp. 1739–1753. eprint: `https://doi.org/10.1246/bcsj.71.1739`. URL: `https://doi.org/10.1246/bcsj.71.1739`.

[3] Ina Strauss et al. "Metal–Organic Framework Co-MOF-74-Based Host–Guest Composites for Resistive Gas Sensing". In: *ACS Applied Materials & Interfaces* 11.15 (2019), pp. 14175–14181. ISSN: 1944-8244. DOI: `10.1021/acsami.8b22002`. URL: `https://doi.org/10.1021/acsami.8b22002`.

[4] Marta Mon et al. "Efficient Gas Separation and Transport Mechanism in Rare Hemilabile Metal–Organic Framework". In: *Chemistry of Materials* 31.15 (2019), pp. 5856–5866. ISSN: 0897-4756. DOI: `10.1021/acs.chemmater.9b01995`. URL: `https://doi.org/10.1021/acs.chemmater.9b01995`.

[5] Sridhar Palla and Niket S. Kaisare. "Evaluating the impact of pellet densification and graphite addition for design of on-board hydrogen storage in a fixed bed of MOF-5 pellets". In: *International Journal of Hydrogen Energy* (2020). ISSN: 0360-3199. URL: `http://www.sciencedirect.com/science/article/pii/S0360319920311551`.

[6] Huacheng Zhang et al. "Ultrafast selective transport of alkali metal ions in metal organic frameworks with subnanometer pores". In: *Science Advances* 4.2 (2018). eprint: `https://advances.sciencemag.org/content/4/2/eaaq0066.full.pdf`. URL: `https://advances.sciencemag.org/content/4/2/eaaq0066`.

[7]   Yan Zheng et al. "Metal–organic frameworks for lithium–sulfur batteries". In: *J. Mater. Chem. A* 7 (8 2019), pp. 3469–3491. URL: `http://dx.doi.org/10.1039/C8TA11075A`.

[8]   Anastasiya Bavykina et al. "Metal–Organic Frameworks in Heterogeneous Catalysis: Recent Progress, New Trends, and Future Perspectives". In: *Chemical Reviews* (2020). ISSN: 0009-2665. DOI: `10.1021/acs.chemrev.9b00685`. URL: `https://doi.org/10.1021/acs.chemrev.9b00685`.

[9]   J. M. Yaghi M. O.and Kalmutzki and C. S. Diercks. *Introduction to Reticular Chemistry: Metal-Organic Frameworks and Covalent Organic Frameworks*. eng. Wiley-VCH, 2019, p. 19. ISBN: 9783527345021.

[10]   Mohamed Eddaoudi et al. "Systematic Design of Pore Size and Functionality in Isoreticular MOFs and Their Application in Methane Storage". In: *Science* 295.5554 (2002), pp. 469–472. ISSN: 0036-8075. eprint: `https://science.sciencemag.org/content/295/5554/469.full.pdf`. URL: `https://science.sciencemag.org/content/295/5554/469`.

[11]   F. Takusagawa and A. Shimada. "Isonicotinic acid". In: *Acta Crystallographica Section B* 32.6 (1976), pp. 1925–1927. URL: `https://doi.org/10.1107/S0567740876006754`.

[12]   Jack Y. Lu and Amy M. Babb. "An extremely stable open-framework metal–organic polymer with expandable structure and selective adsorption capability". In: *Chem. Commun.* (13 2002), pp. 1340–1341. URL: `http://dx.doi.org/10.1039/B200213B`.

[13]   B. J. Hathaway. "The evidence for "out-of-the-plane" bonding in axial complexes of the copper(II) ion". In: (1973), pp. 49–67.

[14]   Leonard J. Barbour. "Crystal porosity and the burden of proof". In: *Chem. Commun.* (11 2006), pp. 1163–1168. URL: `http://dx.doi.org/10.1039/B515612M`.

[15]   Bin Zhai et al. "Structures and magnetic properties of 3D manganese(II)- and 2D pillar-layered copper(II)-organic framework derived from mixed carboxylate ligands". In: *Journal of Solid State Chemistry* 264 (2018), pp. 29–34. ISSN: 0022-4596. URL: `http://www.sciencedirect.com/science/article/pii/S0022459618301749`.

[16] Feng Luo, Yun-xia Che, and Ji-min Zheng. "Highly Rare Ferromagnetic Interaction with the Cu(tetrahedron)-Cu(square)-Cu(tetrahedron) Mode Observed in A 2-Fold Interpenetrating Moganite Net". In: *Crystal Growth & Design* 9.5 (2009), pp. 2047–2049. ISSN: 1528-7483. DOI: 10.1021/cg801208z. URL: https://doi.org/10.1021/cg801208z.

[17] Leroy Alexander. *X-ray diffraction methods in polymer science: Preferred Orientations in Polymers.* Wiley-Interscience, 1969, pp. 210–211. URL: https://doi.org/10.1007/BF00550300.

[18] W. Bragg. "The Diffraction of Short Electromagnetic Waves by a Crystal". In: *Proceedings of the Cambridge Philosophical Society* 17 (1913), pp. 43–57.

[19] W. Friedrich, P. Knipping, and M. Laue. "Interferenzerscheinungen bei Röntgenstrahlen". In: *Annalen der Physik* 346.10 (1913), pp. 971–988. eprint: https://onlinelibrary.wiley.com/doi/pdf/10.1002/andp.19133461004. URL: https://onlinelibrary.wiley.com/doi/abs/10.1002/andp.19133461004.

[20] Benedikt Schrode et al. "*GIDVis*: a comprehensive software tool for geometry-independent grazing-incidence X-ray diffraction data analysis and pole-figure calculations". In: *Journal of Applied Crystallography* 52.3 (2019), pp. 683–689. URL: https://doi.org/10.1107/S1600576719004485.

[21] Roland Resel. "Lecture: X-Ray and Neutron Scattering". In: ().

[22] "Grazing Incidence Configurations". In: *Thin Film Analysis by X-Ray Scattering.* John Wiley and Sons, Ltd, 2006. Chap. 4, pp. 143–182. ISBN: 9783527607594. eprint: https://onlinelibrary.wiley.com/doi/pdf/10.1002/3527607595.ch4. URL: https://onlinelibrary.wiley.com/doi/abs/10.1002/3527607595.ch4.

[23] Soojin Park et al. "Macroscopic 10-Terabit–per–Square-Inch Arrays from Block Copolymers with Lateral Order". In: *Science* 323.5917 (2009), pp. 1030–1033. ISSN: 0036-8075. eprint: https://science.sciencemag.org/content/323/5917/1030.full.pdf. URL: https://science.sciencemag.org/content/323/5917/1030.

[24] A. L. Patterson. "A Fourier Series Method for the Determination of the Components of Interatomic Distances in Crystals". In: *Phys. Rev.* 46 (5 1934), pp. 372–376. URL: https://link.aps.org/doi/10.1103/PhysRev.46.372.

[25] D. W. Bennett. *Understanding single-crystal X-ray crystallography.* eng. Wiley-VCH, 2010, pp. 497–569. ISBN: 9783527326778.

[26]   Sulochanadevi Baskaran. "Structure and Regulation of Yeast Glycogen Synthase". In: (2010).

[27]   Dorothy Mary Crowfoot Hodgkin et al. "The structure of vitamin B12. 1. An outline of the crystallographic investigation of vitamin B12". In: *Proc. R. Soc. Lond. A* 242.15 (1957), pp. 228–263. ISSN: 0080-4630. DOI: 10.1098/rspa.1957.0174. URL: https://doi.org/10.1098/rspa.1957.0174.

[28]   Nam et al. "Polymorphs of Pentacene and 6,13-Pentacenequinone in Solution and Vapor Phase Growths." In: *Bulletin of the Korean Chemical Society* 31.8 (2010), pp. 2413–2415.

[29]   U. Shmueli. *International Table for Crystallography Volume B: Reciprocal Space.* eng. Kluwer Academic Publishers, 1996, p. 235.

[30]   Akitaka Hoshino, Yoshiko Takenaka, and Hideki Miyaji. "Redetermination of the crystal structure of α-copper phthalocyanine grown on KCl". In: *Acta Crystallographica Section B* 59.3 (2003), pp. 393–403.

[31]   Jack Y. Lu and Amy M. Babb. "An unprecedented interpenetrating structure with two covalently bonded open-frameworks of different dimensionality". In: *Chem. Commun.* (9 2001), pp. 821–822. URL: http://dx.doi.org/10.1039/B100634G.

[32]   Anne Pichon, Ana Lazuen-Garay, and Stuart L. James. "Solvent-free synthesis of a microporous metal–organic framework". In: *CrystEngComm* 8 (3 2006), pp. 211–214. URL: http://dx.doi.org/10.1039/B513750K.

[33]   Adedibu C. Tella et al. "Synthesis of copper–isonicotinate metal–organic frameworks simply by mixing solid reactants and investigation of their adsorptive properties for the removal of the fluorescein dye". In: *New J. Chem.* 38 (9 2014), pp. 4494–4500. URL: http://dx.doi.org/10.1039/C4NJ00411F.

[34]   Timothée Stassin et al. "Vapour-phase deposition of oriented copper dicarboxylate metal–organic framework thin films". In: *Chem. Commun.* 55 (68 2019), pp. 10056–10059. URL: http://dx.doi.org/10.1039/C9CC05161A.

[35]   Peter Zaumseil. "High-resolution characterization of the forbidden Si 200 and Si 222 reflections". In: *Journal of Applied Crystallography* 48.2 (Apr. 2015), pp. 528–532. URL: https://doi.org/10.1107/S1600576715004732.

[36] Haruhiko Tanaka and Tomoko Sadamoto. "The simultaneous determination of the kinetics and thermodynamics of Cu(OH)2 decomposition by means of TG and DSC". In: *Thermochimica Acta* 54.3 (1982), pp. 273–280. ISSN: 0040-6031. URL: `http://www.sciencedirect.com/science/article/pii/0040603182800178`.

[37] Josef Simbrunner et al. "Indexing of grazing-incidence X-ray diffraction patterns: the case of fibre-textured thin films". In: *Acta Crystallographica Section A* 74.4 (2018), pp. 373–387. URL: `https://doi.org/10.1107/S2053273318006629`.

[38] Benedikt Schrode. *GIDVis: Guide and Tutorials*. TU Graz, 2019. URL: `https://bitbucket.org/BenediktSchrode/gidvis/raw/master/Manual/Manual.pdf`.

[39] A. I. Kitaigorodskii. "The principle of close packing and the condition of thermodynamic stability of organic crystals". In: *Acta Crystallographica* 18.4 (1965), pp. 585–590. URL: `https://doi.org/10.1107/S0365110X65001391`.

[40] George M. Sheldrick. "A short history of *SHELX*". In: *Acta Crystallographica Section A* 64.1 (2008), pp. 112–122. URL: `https://doi.org/10.1107/S0108767307043930`.

[41] G. Calvarin and D. Weigel. "Structure cristalline et moléculaire de l'acétyl-I' benzoylferrocène". In: *Acta Crystallographica Section B* 27.6 (1971), pp. 1253–1263. URL: `https://doi.org/10.1107/S0567740871003820`.

[42] Theo Hahn. *International Table for Crystallography Volume A: Space-Group Symmetry*. eng. 1983, p. 910.

[43] University of London. Birkbeck College. *Space Group Diagrams and Tables*. 1997. URL: `http://img.chem.ucl.ac.uk/sgp/large/sgp.htm` (visited on 08/30/2020).

[44] E. L. Church and P. Z. Takacs. "The Interpretation Of Glancing Incidence Scattering Measurements". In: *Grazing Incidence Optics*. Ed. by John F. Osantowski and Leon P. Van Speybroeck. Vol. 0640. International Society for Optics and Photonics. SPIE, 1986, pp. 126–133. URL: `https://doi.org/10.1117/12.964364`.